HYPERSONIC MEASUREMENTS OF ROUGHNESS-INDUCED TRANSIENT GROWTH

A Dissertation

by

NICOLE SUSANNE SHARP

Submitted to the Office of Graduate and Professional Studies of
Texas A&M University
in partial fulfillment of the requirements for the degree of

DOCTOR OF PHILOSOPHY

Chair of Committee,	Edward B. White
Committee Members,	Rodney Bowersox
	Devesh Ranjan
	Helen Reed
	William Saric
Head of Department,	Rodney Bowersox

May 2014

Major Subject: Aerospace Engineering

ABSTRACT

The effects of surface roughness on boundary-layer disturbance growth and laminar-to-turbulent transition are not well understood, especially in hypersonic boundary layers. The transient growth mechanism that produces algebraic growth of streamwise streaks may play a key role in roughness-induced transition but has not previously been deliberately observed in hypersonic flow. To make such measurements, the present work studies the boundary layer of a 5° half-angle smooth cone paired with a slightly blunted nosetip and a ring of 18 periodically-spaced cube-like discrete roughness elements 1-mm tall by 1.78-mm wide by 1.78-mm long. The roughness element height is approximately equal to the boundary-layer thickness. Measurements are made in the low-disturbance Texas A&M Mach 6 Quiet Tunnel. No transition to turbulence is observed for freestream unit Reynolds numbers between 7.5×10^6 m^{-1} and 9.8×10^6 m^{-1}. Pitot measurements reveal azimuthally-alternating high- and low-speed streaks growing downstream of the roughness. Large unsteadiness is measured in the roughness wake but decays downstream. The streamwise evolution of the steady and unsteady disturbance energy is consistent with low-speed observations of transient growth in the mid-wake region behind periodically-spaced cylindrical roughness elements. This experiment contains the first quantitative measurements of roughness-induced transient growth in a high-speed boundary layer.

For Granddaddy, in loving memory.

ACKNOWLEDGEMENTS

I would like to begin by thanking my advisor, Dr. Edward White, for his support, not only during my Ph.D. but since my days as an undergraduate at Case Western Reserve University. I have known Ed for more than a decade now. He has guided my development as an engineer and a fluid dynamicist almost from the start, and I would not be who I am and where I am today without his influence.

Although I have been Dr. White's student, most of my time at Texas A&M has been spent in Dr. Rodney Bowersox's National Aerothermochemistry Laboratory (NAL). Dr. Bowersox has been like a second advisor, and I am grateful to him for his input and support, as well as his commitment to helping me feel a part of the NAL. I also thank the remainder of my committee—Dr. William Saric, Dr. Helen Reed, and Dr. Devesh Ranjan—for their support during my work and their dedication in challenging me to be my very best.

I would also like to thank my fellow students and researchers at the NAL, both past and present. First and foremost, I thank Dr. Jerrod Hofferth, who built the M6QT and its instrumentation. Jerrod's hard work produced a world-class facility equipped with instruments and capabilities that made it possible for me to focus my efforts on attempting measurements no one had ever done before. His guidance and insight were invaluable to me in designing and executing my experiments. I am also grateful to Dr. Michael Semper, in particular for his guidance when I was designing my Pitot probe, and Dr. Ray Humble, who first suggested the photocapture method for measuring distributed roughness. Additionally, I am enormously grateful to Alex Craig, Chi Mai,

and Ian Neel for repeatedly sacrificing their evenings and weekends to help me collect data.

I am also indebted to past and present members of Dr. White's research group. Dr. Nick Denissen taught me an enormous amount not only about transient growth but about boundary-layer stability in general. Dr. Rob Downs and Doug Kutz provided valuable assistance and code when I was designing my quasi-random periodic distributed roughness. Jason Monschke's help has been invaluable, not only for the self-similar solutions and optimal disturbance calculations he has performed to complement my experimental work, but for the many fruitful discussions we have had. Similarly, I am grateful to Matt Kuester for our enlightening and productive conversations about transient growth at both high- and low-speeds. I am thankful also for Bobby Ehrmann, who has helped me numerous times and who has also been a dear friend in the lab, on the bike, and in life.

For their assistance in test article fabrication, infrastructure maintenance, and safety oversight, I am grateful to the staff of the Oran W. Nicks Low Speed Wind Tunnel and machine shop. Cecil Rhodes has also been vital for his assistance with infrastructure upgrades and maintenance of the compressors. Thanks are due also to Will Seward of the chemistry department machine shop for silver-soldering my Pitot probe.

I am also forever thankful for the friendship and administrative brilliance of Rebecca Marianno, whose uncanny ability to make things happens has saved me on numerous occasions.

My work has been a part of the AFOSR/NASA-supported National Center for Hypersonic Laminar-Turbulent Transition Research, and their support through Grant #FA9550-09-1-0341 is gratefully acknowledged. Additionally, I was supported by Zonta International as one of their 2011 Amelia Earhart Fellows.

I am grateful also to those researchers who have and continue to conduct simulations related to my experimental work. At University of California, Los Angeles, fellow hypersonic center researchers Christopher Haley and Dr. Xiaolin Zhong are working on smooth-wall basic state and roughness-inclusive direct numerical simulations. With Dr. Bowersox's help, Dr. Ravi Srinivasan is also conducting direct numerical simulations using the periodically-spaced discrete roughness geometry. Jason Monschke has performed the optimal disturbance calculations described in the dissertation using code kindly shared by Dr. Simone Zuccher. Jason is also working on secondary instability calculations for my experiment.

No Ph.D. is without its struggles, and I owe my friends and family a great debt for their support during the good times and the not-so-good times. I'd especially like to thank the friends I've made through the Aggie Aerospace Women in Engineering, the Texas A&M Cycling Team, the Brazos Valley Cyclists, and two years of racing collegiate cycling. Thank you all for your friendship, your support, and for helping me maintain my sanity!

For the past three-and-a-half years, I have had the great pleasure of doing fluid dynamics outreach through my blogging with FYFD. Writing posts for FYFD five-times-a-week has been truly priceless for expanding my knowledge and familiarity with

the field, and I am extremely grateful for the enthusiasm and support of my readers, which has helped keep me motivated through the latter half of my Ph.D. work.

My parents and sister Kelley have been unfailingly supportive and understanding during these years apart. This degree is the culmination of an education exactly as old as my little sister, and I would never have made it so far without their love and encouragement. Thank you!

Finally, I owe special thanks to my fiancé Dr. Joseph Shoer for his sacrifices, his support, his understanding, his patience, and, above all, his love.

Nicole Sharp
College Station, TX
February 2014

NOMENCLATURE

Acronyms

AFOSR	Air Force Office of Scientific Research
BAM6QT	Boeing/AFOSR Mach 6 Quiet Tunnel (Purdue University)
BES	Biorthogonal eigenfunction system
CAD	Computer-aided design
CMM	Coordinate measuring machine
CTA	Constant-temperature anemometry
DAQ	Data acquisition
DNS	Direct numerical simulation
DRE	Discrete roughness element
EVA	Extra-vehicular activity (a.k.a. spacewalk)
HIFiRE	Hypersonic International Flight Research Experimentation
LHS	Left-hand side
M6QT	Mach 6 Quiet Tunnel (Texas A&M University)
MKS	MKS Instruments, Inc.
MTV	Molecular tagging velocimetry
NAL	National Aerothermochemistry Laboratory
NASA	National Air and Space Administration
NI	National Instruments Corporation
NO	Nitric oxide
PANT	Passive Nosetip Technology

PLIF	Planar laser-induced fluorescence
PSD	Power spectral density
RHS	Right-hand side
rms	Root mean square
SCFM	Standard cubic feet per minute
SLDT	Supersonic Low Disturbance Tunnel (NASA Langley)
TAMU	Texas A&M University
TG Cone	Transient Growth Cone
TSP	Temperature sensitive paint

Variables

a	Speed of sound $\equiv \sqrt{\gamma RT}$
e	Unsteady disturbance energy
E	Steady disturbance energy
G	Transient growth factor = E_{out}/E_{in}
k	Roughness height
L_{nozzle}	Nozzle length = 1.01 m
L_s	Sharp cone length = 0.4558 m
m	Wavenumber
M	Mach number
$\overline{M}$	Basic state Mach number
M'	Steady disturbance
M_e	Edge Mach number
M^{uns}	Unsteady disturbance
p	Static pressure
p_0	Total (stagnation) pressure, measured by Pitot tube
P_0	Stagnation pressure of tunnel
Pr	Prandtl number
r	(1) Recovery factor
	(2) Radial coordinate in nozzle, from centerline
R	Specific gas constant
R_{exit}	Nozzle radius at exit = 95.1 mm

Re	Freestream unit Reynolds number = $\rho_\infty U_\infty / \mu_\infty$
Re_e	Unit Reynolds number based on edge conditions
Re_{kk}	Reynolds number based on roughness height and smooth-wall conditions at the roughness height
Re_{L_s}	Reynolds number based on edge conditions and sharp cone length
T	Temperature
$\hat{T}$	Temperature disturbance
T_0	Tunnel stagnation temperature
T_{aw}	Adiabatic wall-temperature $\equiv T_e\left(1 + r\,\frac{\gamma - 1}{2} M_e^2\right)$
T_e	Temperature at boundary-layer edge
T_{hw}	Hot-wire operating temperature
T_r	Hot-wire recovery temperature = ηT_t
T_t	Total temperature
T_w	Wall-temperature
$\hat{u}$	Streamwise velocity disturbance
U	Streamwise velocity
U_∞	Freestream velocity
U_e	Velocity at boundary-layer edge
$\hat{v}$	Wall-normal velocity disturbance
V	Wall-normal velocity
$\hat{w}$	Spanwise velocity disturbance

W	Spanwise velocity
x	Streamwise coordinate
X	(1) Axial coordinate along cone, measured from sharp tip
	(2) Streamwise coordinate along nozzle, measured from throat
y	Wall-normal coordinate
Y	Wall-normal coordinate, measured from cone surface
η	(1) wall-normal disturbance vorticity
	(2) Hot-wire recovery factor $\equiv T_r / T_t$
δ	Boundary-layer thickness
δ^*	Displacement thickness
γ	Ratio of specific heats
γ_c	Cone half-angle
λ	Wavelength
λ_k	Roughness disturbance wavelength
μ_∞	Freestream absolute viscosity (via Sutherland's Law)
μ_e	Viscosity at boundary-layer edge
ν_e	Kinematic viscosity at the boundary-layer edge
ρ	Density
$\hat{\rho}$	Density disturbance
ρ_∞	Freestream density
ρ_e	Density at boundary-layer edge
θ	(1) Azimuthal angle around nosetip

	(2) Momentum thickness
ϕ	Azimuthal coordinate
τ	Hot-wire temperature loading factor = $(T_{hw} - T_r)/T_t$

TABLE OF CONTENTS

Page

Page

LIST OF FIGURES

FIGURE Page

FIGURE Page

LIST OF TABLES

1. INTRODUCTION

1.1 Background and motivation

The transition from laminar to turbulent flow in a boundary layer has been an open problem in physics for more than a century. In hypersonic flows, a turbulent boundary layer on a vehicle increases skin friction and rate of heat transfer. Despite fifty years of experience in the hypersonic regime, predictions for transition location on flight vehicles remain empirical in nature. The underlying physical mechanisms for transition continue as active topics for research, and, though much progress has been made on the transition question at low-speeds, work at hypersonic speeds proceeds at a slower pace.

Transition occurs when environmental disturbances—such as turbulent or acoustic freestream fluctuations, surface roughness, curvature discontinuities, or surface vibrations—enter the boundary layer, where the resulting perturbation may grow or decay. If the disturbance grows to sufficient amplitude, the laminar basic state is changed, and subsequent secondary instabilities of this altered basic state may lead to growth of other disturbances and an ultimate breakdown into turbulent flow. In two-dimensional, incompressible boundary layers, the linearized disturbance equations show that spanwise-invariant traveling waves, known as Tollmien-Schlichting waves, undergo exponential energy growth once a certain "critical" Reynolds number is reached. In compressible boundary layers, this same viscous mechanism exists but is known as the first mode, after Mack's (1984) terminology. The first mode dominates in two-dimensional, compressible boundary layers below a Mach number of 4 and can be stabilized by wall-cooling (Mack 1984).

Unlike their incompressible counterparts, two-dimensional, compressible boundary layers exhibit an additional exponentially growing instability, known as the second mode (Mack 1984), resulting from acoustic waves trapped inside the boundary layer. The second mode tends to dominate transition in two-dimensional boundary layers above Mach 4, and, unlike the first mode, the second mode is destabilized by wall-cooling (Mack 1984).

In three-dimensional boundary layers, still more exponentially growing instabilities are possible. For swept surfaces or at angle of attack, exponentially growing traveling or stationary crossflow waves can occur, leading to secondary instabilities (Saric *et al.* 2003). On surfaces with concave curvature, Görtler instabilities may form and grow, also leading to secondary mechanisms and breakdown (Saric 1994). All of the preceding disturbances are eigenmodes of the linearized Navier-Stokes equations, and both their mode shapes and growth rates may be described completely by solving the eigenvalue problem.

Some environmental disturbances—particularly the surface roughness of interest in this dissertation—introduce complex behavior that defies description by these traditional modal explanations. Instead, an algebraic-growth mechanism first described by Ellingsen and Palm (1975) and later refined by Landahl (1980) as the "lift-up" mechanism has been suggested. Landahl demonstrates that a finite perturbation aligned with the base flow's gradient and with a velocity component normal to the base flow will result in algebraic growth of a streamwise disturbance. Moreover, three-dimensional disturbances aligned in this fashion will produce a "streaky" flow with localized regions

of momentum excess and defect caused by the redistribution of streamwise momentum by the wall-normal velocity perturbations. Perhaps the most important characteristic of this mechanism is its capability to produce disturbance growth in boundary layers where no traditional instabilities exist. That is, even if in the limit of extended time or streamwise distance all perturbations in a flow are decaying, an initial period of disturbance growth remains possible. This *transient growth* may be a factor in the transition of many flows not well described by traditional linear stability theory, from simple pipe flow to the atmospheric re-entry of blunt-bodied capsules (Reshotko 2001). In boundary layers, transient growth results in the creation of low- and high-speed streamwise streaks. These streaks manifest as adjacent regions of accelerated and decelerated flow relative to the boundary layer basic state, and have been observed at low-speeds as the result of surface roughness (White 2002, Fransson *et al.* 2004, White *et al.* 2005). It is the aim of the present work to measure this same behavior in a hypersonic boundary layer.

The current framework used to categorize boundary layer transition behavior is credited to Morkovin *et al.* (1994). Figure 1-1 shows this transition roadmap and the role played by transient growth as the initial environmental disturbance amplitude increases. In this framework, Path A represents the scenarios of modal growth described previously, and represents much of the existing and emerging work in hypersonic boundary layer transition. This includes work on first and second mode growth, crossflow waves, Görtler instabilities, and so on.

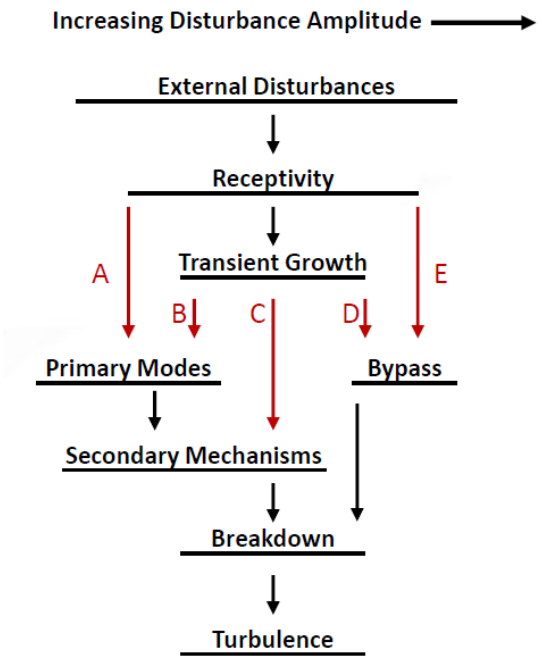

Figure 1-1. Roadmap for transition to turbulence in boundary layers. Adapted from Morkovin *et al.* (1994).

Path B represents a scenario in which nonmodal transient growth increases a disturbance's amplitude prior to modal growth, which takes over once a neutral stability point is crossed and a region of exponential instability begins. This scenario requires transient growth, which is strongest for stationary streamwise disturbances, to couple into modal growth, which may be largest at supersonic speeds for non-streamwise disturbances. Tempelmann *et al.* (2012) have completed calculations demonstrating this path to transition for a compressible boundary layer on a swept flat plate. In their work, optimal transient growth disturbances provide initial growth for what becomes stationary crossflow waves past the first neutral point.

Across low- and high-speed flows, most research on transient growth falls into Path C, in which transiently growing disturbances result in sufficient alteration of the basic state flow that secondary effects occur and lead to breakdown. This path includes some cases of transition which were previously classified as "by-pass transition" because they did not conform to modal growth explanations. Analysis of Path C transition in the wake of surface roughness involves several stages. The first, as shown in the roadmap, is receptivity, in which roughness is converted to a flow perturbation inside the boundary layer. Much effort has been dedicated to understanding receptivity in recent years, but the problem remains complex and difficult to characterize. Unlike the subsequent disturbance growth, which Denissen (2011) shows linearized equations capture, the initial input forcing is not easily quantified. Experimental work indicates receptivity is non-linear, even when the subsequent disturbance evolution is linear (White *et al.* 2005). For transient growth, the situation is further complicated by a lack of fixed mode shapes to search for in either experiments or direct numerical simulation (DNS) (White 2002). Both the mode shape and growth rate for transient growth are fixed by receptivity, *not* the eigenvalue problem. Several mathematical tools have been suggested for analyzing the receptivity of transient growth, some of which will be discussed in the following section.

The receptivity phase is followed by a period of transient growth, in which the perturbation grows larger in amplitude and distorts the mean flow. This growth is described by a linear process (Denissen 2011). Every eigenmode contained within the perturbation ultimately decays; however, the perturbation, as the sum of these decaying

modes, can still experience net energy growth. This occurs due to the non-orthogonality of the Orr-Sommerfeld and Squire equations (and their compressible counterparts). Because these equations are not self-adjoint, their eigenmodes are non-orthogonal. As a result, they may interfere both constructively and destructively with one another. The growth and decay of a perturbation is computed by tracking every mode in the boundary layer, unlike in modal growth where only unstable modes and their harmonics are computed.

Physically, roughness-induced transient growth occurs on streamwise disturbances generated in the wake of surface roughness, such as the counter-rotating, stationary, streamwise vortices wrapped around a roughness element (Whitehead 1969, Danehy *et al.* 2010, Iyer and Mahesh 2013). Viscosity decays these vortices, and their behavior is described by the Orr-Sommerfeld disturbance equation. As the vortex pair spins, it redistributes momentum in the boundary layer, pulling high-momentum fluid lower and pushing low-momentum fluid higher, as described by Landahl's lift-up mechanism (Landahl 1980). This action distorts the mean-flow field around the decaying vortex, resulting in the creation of high- and low-speed streaks. The coupling between the Orr-Sommerfeld and Squire equations is such that this decaying disturbance caused by the streamwise vortices generates vorticity in the wall-normal plane—the transiently-growing streaks. Reshotko (2001) demonstrates this behavior with a two-equation model problem, in which the Orr-Sommerfeld and Squire operators are replaced with their eigenvalues. The system of disturbance equations is:

$$\frac{\partial}{\partial t}\begin{pmatrix}\xi\\ \eta\end{pmatrix}=\begin{pmatrix}L_{os} & 0\\ \gamma & L_s\end{pmatrix}\begin{pmatrix}\xi\\ \eta\end{pmatrix} \tag{1.1}$$

where ξ is the disturbance vorticity in the x-z plane; η is the disturbance vorticity normal to the wall; L_{OS} and L_S are, respectively, the homogenous Orr-Sommerfeld and Squire operators, without their time-varying terms; and γ is a coupling coefficient. Replacing the operators with their eigenvalues allows a simple model "solution" indicative of transient growth behavior. Let $L_{os}\xi = -\lambda\xi$, $L_s\eta = -\mu\eta$ with initial conditions $\xi(0)=\xi_0, \eta(0)=\eta_0$, representing decaying disturbances. Thus, the "solution" to Equation 1.1 becomes:

$$\xi = \xi_0 e^{-\lambda t}, \eta = -\gamma\xi_0\left(\frac{e^{-\lambda t}-e^{-\mu t}}{\lambda-\mu}\right)+\eta_0 e^{-\mu t} \tag{1.2}$$

For the special case in which $\lambda=\mu$, this result simplifies to:

$$\xi = \xi_0 e^{-\lambda t}, \eta = -\gamma\xi_0 t e^{-\lambda t}+\eta_0 e^{-\lambda t} \tag{1.3}$$

in which the Orr-Sommerfeld result is purely decaying but its uni-directional coupling to the Squire result causes algebraic growth of the wall-normal disturbance vorticity for small *t,* followed by exponential decay as *t* continues to grow. Physically, the Orr-Sommerfeld "solution" corresponds to the decaying streamwise vortex, whereas the Squire "solution" represents the transiently-growing streak.

Eventually, the perturbation distorts the mean-flow in the form of stationary streamwise streaks. As these streaks grow in amplitude, they can be destabilized by secondary, inflectional instabilities. The combined flow—a Blasius-type basic state plus transient growth—may then transition. Measuring these streaks and the streamwise

evolution of their disturbance energy in a boundary layer constitutes evidence of transient growth. Prior to this dissertation, no deliberate measurements confirming the existence of transient growth in a hypersonic boundary layer have occurred.

1.2 Roughness-induced transition

All realistic hypersonic vehicles feature rough surfaces. This roughness may be isolated, in the form of a fastener, a joint, or protuberance; or it may be distributed in nature. Distributed roughness includes marks left by machining, ablating surfaces, and the background surface roughness of a vehicle's thermal protection system. Distributed roughness may also describe arrays of individual roughness elements, also known as discrete roughness elements (DREs). Roughness is also categorized as two-dimensional—e.g. steps or gaps—or three-dimensional, according to its geometry.

Historically, many studies of roughness-induced hypersonic transition have been experimental, due to the computational difficulty of calculating flow over distributed rough surfaces. Reda (2002) and Schneider (2008) review much of the experimental work, which focuses on transition location prediction, not on the receptivity process and subsequent disturbance growth. The importance of surface roughness amplitude and its effect on transition location has been of historic interest, due to its usefulness in design. Surface roughness is deemed "critical" in height when the transition front moves forward from its smooth wall location. Continuing to increase the roughness height moves the transition location further forward. When the transition front has advanced to its closest location to the roughness, the trip height is deemed "effective". Such studies of roughness-induced transition find that three-dimensional, distributed surface

roughness results in earlier transition than isolated, three-dimensional roughness elements of equivalent height and shape (Reda 2002). Thus distributed surface roughness is "more critical" than isolated, three-dimensional surface roughness.

One of the most enduring studies of hypersonic roughness-induced transition, the Passive Nosetip Technology (PANT) program, was carried out by Acurex Corporation during the 1970s (Wool 1975a, 1975b). The experimental portion of the PANT program included arcjet and wind tunnel tests of hemispherically blunted nosetips using a variety of geometries, materials, and surface roughness configurations. Nosetip transition for the PANT data set is confined to edge Mach numbers less than 1. Although the transition location correlation suggested by the PANT program is no longer in wide use, the program's data set remains a foundation stone upon which many such correlations are built (Batt and Legner 1983, Reda 2002, Reshotko 2008).

Most hypersonic surface roughness studies to date, including PANT, were conducted in conventional hypersonic wind tunnels, in which turbulent boundary layers on the nozzle walls radiate acoustic disturbances into the freestream along Mach lines (Morkovin 1969). This freestream contamination alters the receptivity relative to the low-disturbance free-flight environment, and can result in transition due to different physical mechanisms than in flight. Casper *et al.* (2011) studied the effects of freestream noise on transition location for an isolated diamond roughness element on a scale model of the HIFiRE cone (Kimmel *et al.* 2007) using temperature sensitive paint (TSP). The work was conducted in Purdue University's Boeing/AFOSR Mach-6 Quiet Tunnel (BAM6QT), which utilizes bleed slots at the nozzle throat to initiate a new

laminar boundary layer on the nozzle wall. Casper *et al.* (2011) found that effective roughness heights under noisy flow are not always as effective under quiet flow. Moreover, roughness heights that were effective under both noisy and quiet flow still saw later transition under quiet flow. While this study did not pinpoint the physical mechanism by which freestream disturbances affected transition, it clearly demonstrated that these fluctuations can affect the transition process. Borg and Schneider (2008) observed similar effects of freestream noise on roughness-induced transition using periodic roughness arrays on a 20%-scale model of the X-51A forebody.

Ballistic range experiments offer an alternative to conventional wind tunnel studies. Recently, Reda and coworkers have conducted ballistic-range experiments using blunt bodies with isolated (Reda *et al.* 2010) and distributed surface roughness (Reda *et al.* 2008) as well as large half-angle cones with small (Reda *et al.* 2012a) and large nose bluntness (Reda *et al.* 2012b) and distributed roughness. The blunt bodies, both hemispherical and conic, had roughness elements or distributed roughness placed on the nose (Reda *et al.* 2008, 2010), whereas the more recent conic experiments had smooth nosetips and roughened frusta (Reda *et al.* 2012a,b). Models were fired at Mach 10 through quiescent air, and infrared thermography was used to track the transition location on the models in flight. Reda *et al.* (2010) found that isolated roughness was less effective at tripping the boundary layer than distributed surface roughness, and that tripping was more difficult to achieve for elements placed near the stagnation point. For distributed roughness, Reda advocates a critical roughness Reynolds number parameter at transition:

$$\mathrm{Re}_{ke,tr} = \frac{U_e k}{\nu_e} \tag{1.4}$$

where k represents roughness height and the subscript e indicates flow parameters evaluated at the boundary layer edge, as a method of predicting transition location. The value of the critical roughness Reynolds number at transition varies by geometry and is not consistent across all tested geometries (Reda *et al.* 2013).

Recent work in super- and hypersonic roughness-induced transition has focused on the effects of isolated roughness elements. This interest is motivated largely by the STS-114 Space Shuttle mission, in which astronaut Stephen Robinson conducted an extravehicular activity (EVA) on the underside of the shuttle *Discovery* to remove two pieces of protruding gap filler from between the thermal protection system tiles. At the time, NASA had too little data to predict the effects this isolated roughness would have on the shuttle's boundary layer transition during re-entry, and the risks of a never-before-attempted EVA were deemed less than those of de-orbiting with the gap fillers protruding. Subsequently, NASA initiated several studies on the effects of isolated roughness elements of various shapes relevant to the Space Shuttle as well as the Orion Crew Exploration Vehicle.

Danehy and coworkers have utilized NASA Langley Research Center's 31-inch Mach 10 Wind Tunnel facility for nitric oxide (NO) planar laser-induced fluorescence (PLIF) studies with isolated roughness elements of various shapes and heights on a flat-plate model. Isolated roughness elements are placed on the upper surface of a sharp, smooth, 10-degree half-angle wedge. Edge Mach numbers are varied by changing the

model's angle of attack. Boundary layer thickness is controlled with both angle of attack and stagnation pressure. Danehy *et al.* (2007) studies flow past rectangular and triangular roughness elements oriented at a 45° angle to the streamwise flow direction. The results showed laminar, transitional, and turbulent flow patterns along the centerline in the wake of the roughness element, depending on the relative height of the roughness to the boundary layer. Danehy *et al.* (2009) examines the effects of isolated hemispherical roughness elements, with NO PLIF plan view images showing the formation of streaks and what appear to be "counter-rotating, streamwise, corkscrew-shaped structures emanating from the sides of the trip" (Danehy *et al.* 2009). These structures appear consistent with vortices originating upstream of the roughness element wrapping around to form streamwise vortices in the element's wake—an ideal situation for transient disturbance growth.

Iyer and Mahesh (2013) perform a DNS study matching Danehy *et al.* (2009)'s experimental conditions. Qualitatively, the structures seen in the DNS match those in the experiment. Using their computational results, Iyer and Mahesh (2013) are able to explore the structure of flow upstream and downstream of the hemispherical roughness element, finding that systems of unsteady spanwise vortices form upstream of the roughness, wrap around, and become systems of streamwise vortices in the symmetry and off-symmetry planes downstream of the roughness. Iyer and Mahesh (2013) report significant increases in skin friction downstream of the roughness element even in the high Mach number flows that remain laminar, suggesting that flow distortion effects may be significant even when insufficient to cause transition.

Danehy *et al.* (2010) focuses on isolated cylindrical roughness elements in hypersonic flow. Like the hemispherical elements in prior work, NO PLIF visualizations of the flow downstream of the cylindrical elements show streaky structures. Oil-flow visualizations show formations similar to Whitehead's (1969) results, with alternating bands of parallel lines indicative of multiple counter-rotating vortices downstream of the roughness element. Bathel *et al.* (2010) and (2013) study isolated cylindrical roughness elements using the same tunnel and flat-plate model. NO molecular tagging velocimetry (MTV) is used to quantitatively measure boundary layer profiles fore and aft of the roughness element. Bathel *et al.* (2010) found spanwise mean-flow distortion consistent with high- and low-speed streaks; in combination with temperature sensitive paint, they saw regions of increased heat transfer corresponding to regions of increased velocity downstream of the trip. In roughness element wake profiles, Bathel *et al.* (2013) saw increased velocity relative to a smooth-wall laminar profile deep in the boundary layer and a velocity defect higher from the surface. They concluded that the differences in velocity profile relative to a laminar profile are indicative of transition to turbulence.

Computational and experimental studies of isolated roughness elements in a supersonic flat-plate boundary layer are also on-going. Choudhari *et al.* (2010) study a diamond-shaped isolated roughness element in a Mach 3.5 flat-plate boundary layer. The mean-flow field shows the formation of streamwise streaks in the wake of the roughness, as well as a mushroom-like shape to the boundary layer thickness downstream of the trip. Increasing roughness height increases streak amplitude, and the stability characteristics of the resulting mean-flow indicate both even (symmetric or varicose) and

odd (antisymmetric or sinuous) modes are present in the wake. Complementary experimental work in the NASA Langley Research Center's Mach 3.5 Supersonic Low-Disturbance Tunnel (SLDT), a supersonic quiet wind tunnel, is being carried out by Kegerise and co-workers. Kegerise *et al.* (2010) report results of a study utilizing a diamond-shaped roughness element on a straight, 7-degree half-angle cone; baseline measurements on the cone without roughness agree well with computations by Choudhari *et al.* (2010) and hot-wire measurements of mean and fluctuating mass-flux profiles downstream of the roughness element are reported. Spectra show instability growth for frequencies in the 150-250 kHz range and show qualitative agreement with the results of Choudhari *et al.* (2010). Experiments for a diamond-shaped roughness element on a flat plate in quiet Mach 3.5 flow are on-going (Kegerise, private communication).

The only known experiments directly measuring growth of a roughness-induced instability in a hypersonic boundary layer under low-disturbance ("quiet") freestream conditions were conducted by Wheaton and Schneider (2012, 2013) at Purdue. The experiment utilized the thick laminar boundary layer along the nozzle wall of the Boeing/AFOSR Mach-6 Quiet Tunnel. Wheaton and Schneider (2012) measured a 21-kHz instability in the wake of an isolated cylindrical roughness element with height approximately equal to the boundary layer thickness ($k/\delta \sim 1$) at Mach 5.95. They confirmed the existence of the instability using Pitot probes and hot-wire anemometry; calculations by Bartkowicz *et al.* (2010) also identified the instability and isolated its origin in a system of unsteady spanwise vortices occurring upstream of the roughness

element, consistent with Iyer and Mahesh's (2013) findings for a hemispherical element. Wheaton and Schneider (2012) confirmed that the instability formed upstream of the roughness element, decayed in the freestream, grew in the wake of the element, and was not present in the case of a smooth wall. They do not attribute the instability to any specific transition mechanism, identifying it only as a laminar wake instability.

Wheaton and Schneider (2013) conducted additional experiments using cylindrical roughness with heights between $k/\delta \sim 0.33$-0.66, also under quiet-flow conditions at Mach 5.95. Using pressure sensors mounted in an array along the centerline of the roughness, Wheaton and Schneider (2013) measured transition onset and wake development downstream of the near-critical roughness element. In their experiment, transition was first observed at $Re_{kk} = 355$, based on computed smooth-wall conditions at the roughness height. Wheaton and Schneider observed significant variations in transition location between runs at nominally-identical experimental conditions, possibly due to differences in wall-temperature differences between runs. In general, their spectral measurements showed initial disturbance growth in the 10-40 kHz range that did not shift in frequency with downstream distance. This was followed downstream by a higher-frequency peak between 40-70 kHz, which did shift to lower frequencies with increasing streamwise distance, suggesting a boundary layer thickness effect. As flow transitioned, the peaks broadened and merged, eventually settling toward smooth-wall turbulent values.

Although these studies of isolated roughness elements in super- and hypersonic flow do not focus on transient growth, the authors' descriptions of streamwise vortex

structures downstream of the roughness element and Bathel *et al.* (2010)'s identification of low-speed streaks in the flow indicate that transient growth may play a role in these wakes. The existence of streamwise vortices in the wake of roughness elements is key to the transient growth of low- and high-speed velocity streaks, as discussed previously. These studies also provide a glimpse of the role of roughness height relative to boundary layer thickness. In particular, the studies by Danehy and coworkers (2007, 2009, 2010), along with the computations of Iyer and Mahesh (2013), indicate that height of the roughness element relative to the boundary layer affects the wake structure and subsequent transition or lack thereof, with larger values of k/δ tending toward turbulence.

Studies specifically targeting hypersonic transient growth have been computational up to this point, in part because the theory is recent and in part due to a lack of low-disturbance hypersonic facilities in which experimental studies are possible. Because transiently growing perturbations are made up of many decaying eigenmodes, the "most unstable" transient perturbation cannot be defined in the sense of modal growth. Instead, optimal disturbance theory suggests calculating the set of initial disturbances for which the maximum net energy growth is achieved at a set downstream distance (Butler and Farrell 1992). Schmid and Henningson (2001) review the theoretical and mathematical basis of optimal disturbances as well as early progress in temporal optimal disturbances, as does Reshotko (2001). A framework for the spatial theory of optimal disturbances in compressible boundary layers is given by Tumin and Reshotko (2001). These early studies found that the most significant transient growth—

in both incompressible and compressible boundary layers—was associated with stationary streamwise vortices (Tumin and Reshotko 2001), similar to those observed downstream of surface roughness (Whitehead 1969, Danehy *et al.* 2010).

Optimal disturbances in hypersonic flow have been computed for a number of geometries including those on a flat plate and sphere (Reshotko and Tumin 2004, Zuccher *et al.* 2006) and a sharp cone (Zuccher *et al.* 2007). Reshotko and Tumin (2004) initially calculate optimal disturbances for a parallel boundary layer on a flat plate and sphere; Zuccher *et al.* (2006) extend the analysis to a non-parallel boundary layer but find the same trends. At low Mach numbers, all geometries saw increased transient growth amplitudes when the wall was cooled relative to an adiabatic wall condition. At higher Mach numbers, wall-cooling's effects were lessened, with even extreme wall-cooling resulting in lower transient growth amplitudes than in the adiabatic case. For zero-pressure-gradient boundary layers, Zuccher *et al.* (2007) found that geometrical divergence created a stabilizing effect on transient growth. In other words, for the same conditions, a boundary layer on a sharp cone had smaller transient growth amplitudes than the equivalent boundary layer on a flat plate. On spheres, an increasing radius led to increased energy growth, particularly in the vicinity of the stagnation point, but because an increasing radius also increases Reynolds number, discerning individual effects is difficult. Tempelmann *et al.* (2012) found similar results for optimal disturbances on flat and curved swept plates for compressible boundary layers up to a Mach number of 1.5. Tempelmann *et al.* (2012) also found that concave curvature

increased transient growth amplitudes, though not to the same extent as the crossflow modes destabilized by that curvature.

Although optimal disturbance calculations are valuable tools in guiding exploration of transient growth, studies of surface roughness at low-speeds have indicated that observed transient growth is suboptimal. In a series of experiments by White and coworkers (White 2002, White *et al.* 2005, Ergin and White 2006), an array of discrete cylindrical roughness elements were placed in an incompressible flat-plate boundary layer. Hot-wire anemometry measured the steady and unsteady spanwise distortions in the velocity field due to transient growth of streamwise streaks. The transient growth observed in these boundary layers was qualitatively similar to that seen in optimal disturbance calculations. However, the experimentally realized disturbances reached their maximum energy growth upstream of the calculated optimal disturbances, and the maximum amplitude reached was lower than that of the optimal disturbance.

Multimode decomposition, a method of extracting the continuous modal amplitudes that describe receptivity for a transiently growing perturbation, was introduced by Tumin (2003) for use in analyzing direct numerical simulations and was extended by Denissen and White (2009) for use in experimental studies, in which only the streamwise velocity perturbations and their streamwise evolution are known. Multimode decomposition uses a biorthogonal eigenfunction system (BES) approach to solve the linearized Navier-Stokes equations in terms of modes of a discrete and continuous spectra. Tumin (2011) reviews the BES methodology and many of its applications to receptivity problems, including roughness effects.

Denissen and White (2009) use multimode decomposition to show conclusively that roughness-induced perturbations cannot be described by optimal disturbance calculations. They showed that suboptimal disturbances exist lower in the boundary layer and decay further upstream than optimal disturbances. Despite their lower maximum amplitudes, however, suboptimal disturbances are more unstable than optimal disturbances, breaking down at lower amplitudes.

Currently, work is underway to extend the use of multimode decomposition to compressible flows for the analysis of both DNS and experiments. However, for the present work, it is necessary to proceed using existing compressible optimal disturbance calculations for guidance as to the qualitative behaviors of hypersonic transient growth with the understanding that, quantitatively, these calculations are not indicative of experimentally-realized transient growth. It is hoped that measurements from the current work will be used in future multimode decomposition studies of hypersonic roughness-induced transient growth.

1.3 Objectives

As described earlier in the background and literature review, at the onset of this work, no experiment had ever deliberately measured roughness-induced transient growth in a hypersonic flow. Given the differences observed between experimentally-realized transient growth and optimal disturbance calculations at low-speeds, elucidating roughness effects at hypersonic speeds requires experimental measurement as well. The primary objective of the present work is to make the first quantitative measurements of roughness-induced transient growth behavior in a hypersonic boundary layer. These

measurements take place on a slightly blunted cone under quiet flow conditions at Mach 5.9.

To achieve this goal requires completion of several smaller objectives. Firstly, an appropriate experimental model for hypersonic roughness-induced transient growth must be designed. Section 2 describes the design and manufacture of this experimental model, as well as describing companion simulations that complement the experimental work.

Secondly, it is necessary to develop and execute a method for measuring and identifying transient growth in a hypersonic flow. The short run-times of hypersonic facilities and the added complexity of compressible flow necessitate departures from the methodology utilized in low-speed transient growth experiments. Section 3 describes the Texas A&M Mach 6 Quiet Tunnel (M6QT) facility, the instrumentation, and the methodology used to measure hypersonic transient growth. Section 4 details the analysis and results that identify roughness-induced transient growth in a hypersonic boundary layer for the first time.

Finally, it is important to place the present work into the context of the existing theoretical, experimental, and numerical understanding of roughness-induced transition and transient growth. To this end, §4 relates the present analysis to the theoretical framework for evaluating disturbance energy and draws numerous parallels to existing work at both high- and low-speed. It also presents an overview of recent high-speed roughness results, including the present work. Lastly, §5 summarizes the conclusions of the current work, and §6 suggests directions and recommendations for future work.

2. TEST DESIGN*

To date, there has been no known effort to deliberately measure roughness-induced transient growth in a hypersonic boundary layer. Such an effort requires a low-disturbance test environment to isolate the effects of surface roughness from those of freestream fluctuations and to permit comparison to existing transient growth theory and optimal disturbance calculations. It is also a necessary step in moving from wholly empirical transition correlations towards physics-based ones informed by an understanding of the underlying transition mechanisms. For such fundamental studies, it is natural to investigate a zero-pressure-gradient boundary layer; at hypersonic velocities, this can be achieved in an axisymmetric nozzle using a cone-geometry at zero angle of attack. The current research utilizes such a cone-geometry in anticipation of the model's use in the TAMU M6QT low-disturbance wind tunnel facility.

This section focuses on the test design of the present research with emphasis on two primary subjects: the wind tunnel model and its companion simulations. The physical details of the Transient Growth Cone (TG Cone) model are discussed, as well as the philosophy of its design and an evaluation of its manufactured quality. Descriptions are also given of test articles that were manufactured for the model but unused in the experiments. They are included here for reference and in the hope that future experiments will utilize these additional configurations. Companion simulations of the model and its test environment are also discussed.

* Portions of this section are reprinted with permission from "Roughness-Induced Transient Growth on a Hypersonic Blunt Cone," by Sharp, N. S., and White, E. B., 2014. *AIAA Paper 2014-0432*, Copyright 2014 by the American Institute of Aeronautics and Astronautics, Inc.

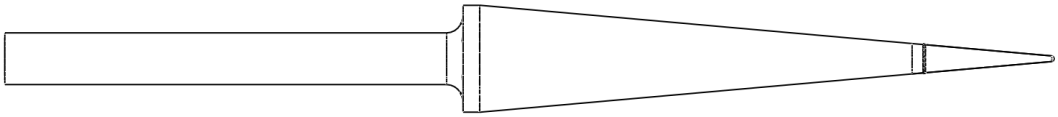

Figure 2-1. Schematic of the TG Cone experimental model with 1.59-mm radius DRE nosetip.

2.1 Transient Growth Cone model

Any wind tunnel model for use in transient growth experiments should be designed to eliminate or avoid the effects of other instabilities and transition mechanisms. To that end, a straight 5° half-angle cone serves as the base for the current Transient Growth Cone (TG Cone). Operating at its nominal freestream conditions, the Mach number in the M6QT test facility remains high enough that the first Mack mode avoided. By operating at a nominal zero-degree angle of attack with a straight cone, both the crossflow and Görtler instabilities are eliminated. Without a flare or adverse pressure gradient to enhance second-mode growth, the model is sub-critical to the second mode. Moreover, the bluntness of the TG Cone's nosetips helps to stabilize the second mode.

The TG Cone, shown in Figure 2-1, consists of a smooth 5° half-angle conic frustum with a base diameter of 79.9 mm and a length of 331.3 mm built to accommodate interchangeable nosetips of varying nose bluntness and surface roughness. The sharp length of a full cone would be 455.8 mm. The frustum and all of its nosetips are constructed from 17-4 PH stainless steel. Relevant measurements of the frustum and nosetips are summarized in Table 2-1.

Cone Model	
Sharp length	455.8 mm
Base diameter	79.88 mm
Frustum	
Length	331.3 mm
Base diameter	79.88 mm
Joint diameter	21.8 mm
Joint location	125.5 mm ($0.27L_s$)
1.59-mm Smooth Nosetip	
Length	107.9 mm
Joint diameter	21.8 mm
6.59-mm Smooth Nosetip	
Length	58.1 mm
Joint diameter	21.8 mm
1.59-mm DRE Nosetip	
Length	107.9 mm
Joint diameter	21.8 mm
Number of roughness elements	18
Roughness axial location	114.5 mm ($0.25L_s$)
Roughness wavelength	3.56 mm (20°)
Roughness height	1.0 mm
Roughness length	1.78 mm
Roughness width	1.78 mm
Roughness spacing	1.78 mm (10°)
6.35-mm DRE Nosetip	
Length	58.1 mm
Joint diameter	21.8 mm
Roughness characteristics	Identical to 1.59-mm DRE nosetip
6.35-mm periodic distributed roughness nosetip	
Length	58.1 mm
Joint diameter	21.9 mm
Roughness axial location	$0.15\text{-}0.27L_s$
Average roughness height	0.11 mm
Roughness periodicity	30°

Table 2-1. Measurements of the experimental model and nosetips. Nosetip lengths refer only to the external geometry, excluding the stem and threading. All axial locations are referenced relative to a sharp tip.

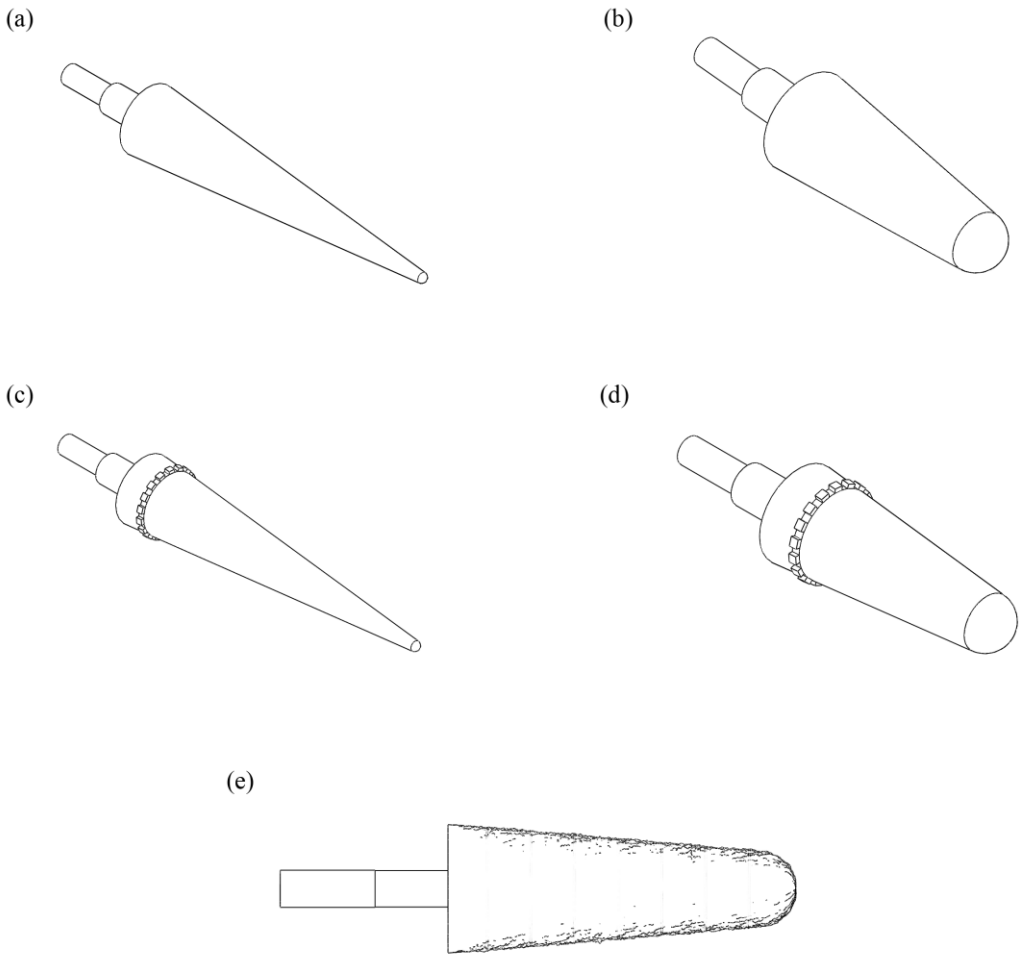

Figure 2-2. Schematic of the TG Cone nosetips. The manufactured nosetips include (a) the 1.59-mm radius smooth nosetip, (b) the 6.25-mm radius smooth nosetip, (c) the 1.59-mm radius DRE nosetip, (d) the 6.35-mm radius DRE nosetip, and (e) the 6.35-mm radius quasi-random periodic distributed roughness nosetip.

Isolating the roughness to the nosetips serves several purposes. The first of these is to allow for testing of a variety of surface roughness configurations (as well as nosetip geometries) without the need to manufacture a full-length model for each. Secondly, the boundary layer is most receptive to disturbances near the leading edge; studying surface

roughness on the nosetip places those disturbances where they are most likely to affect the flow. Finally, confining the surface roughness to an upstream location allows roughness-induced disturbances to grow over a clearly defined downstream extent without interference from continuing surface roughness.

The experiments described in this document utilize only one nosetip: a 1.59-mm radius, spherically blunted nosetip with a ring of periodically-spaced discrete roughness elements (DREs). However, five total nosetips were manufactured alongside the TG Cone's frustum. The design and manufacture of all five nosetips is described in this section. The nosetips, shown in Figure 2-2, consist of the following: two smooth (1.59-mm and 6.35-mm nose radii) nosetips, one distributed rough (6.35-mm nose radius) nosetip, and two nosetips with discrete roughness elements (DREs; 1.59-mm and 6.35-mm nose radii). The nosetips' bluntness was chosen based on the geometry of the M6QT's nozzle, which has an exit diameter of 191 mm. The bow shock off the TG Cone was modeled for different nose bluntnesses and cone insertion lengths. The maximum nose bluntness was chosen because it provided adequate insertion into the nozzle's quiet test core without allowing the bow shock to reflect off the nozzle wall. After machining, the 6.35-mm smooth nosetip and the frustum were ground and polished as one unit, resulting in a nearly invisible joint (< 1 μm). The 1.59-mm smooth nosetip was manufactured to match the frustum as closely as possible without further modifying the frustum. The smooth nosetips provide a potential baseline for comparison with the rough cases.

Surface roughness on hypersonic vehicles comes in many varieties, from isolated roughness to arrays of roughness elements to fully three-dimensional distributed roughness. The TG Cone nosetips utilize two forms of roughness: a ring array of three-dimensional discrete roughness elements (DREs) and periodic quasi-random distributed roughness. Both can be considered representative test cases for real vehicle roughness, with the array of DREs similar to a tripping array or a series of fasteners along a surface and the quasi-random distributed roughness akin to background or ablated surface roughness on a flight vehicle. Unlike a real vehicle, however, both roughness configurations (in their ideal form, at least) consist of clearly defined disturbance wavelengths, which allow for easier analysis of their effects on the boundary layer. Similarly, quantifying the roughness rather than utilizing random or sandpaper-type roughness makes the current work easier for other researchers to replicate in future simulations and experiments. To that end, both the nominal roughness and measures of final model relative to its intended design are discussed.

2.1.1 Discrete roughness element nosetips

The two nosetips with discrete roughness elements (DREs) feature a ring of 18 raised cube-like 1.78-mm long by 1.78-mm wide by 1-mm tall roughness elements located about 10 mm upstream of the frustum joint, corresponding to a $X/L_s = 0.25$. The height k of the DREs is of the order of the local boundary layer thickness. These nosetips allow evaluation of the boundary layer's response to a particular disturbance wavelength, λ_k, based on the spacing of the DREs. The selected disturbance wavelength of 3.56 mm is 3-3.5 times the thickness of the boundary layer at the roughness location, in keeping

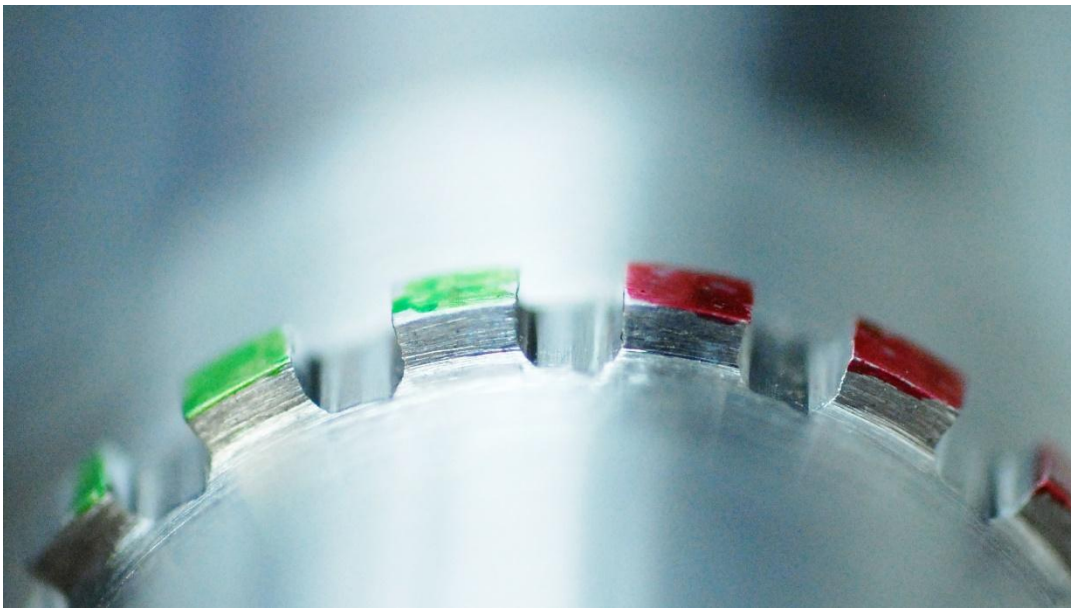

Figure 2-3. Macro photograph of the discrete roughness elements on the 1.59-mm DRE nosetip. The elements are viewed from upstream, with red indicating the port side of the model and green indicating the starboard side.

with the spanwise wavelength for optimal disturbance growth found in the calculations of Reshotko and Tumin (2004). Azimuthally, the disturbance wavelength is 20°, and each roughness element is spaced $\lambda_k/2$, or 10°, from its neighbors. This azimuthal periodicity allows for spatial phase-locked averaging of the experimental measurements, which significantly improves the signal-to-noise characteristics of the data. For the reported experiments, the nosetip radius is 1.59 mm, and the roughness elements are centered at an axial location 97 mm downstream of the nosetip, 114 mm from the apex of an equivalent sharp cone. Figure 2-3 shows a macro image of the roughness elements behind which measurements occurred. After manufacturing, both the 1.59-mm and 6.35-

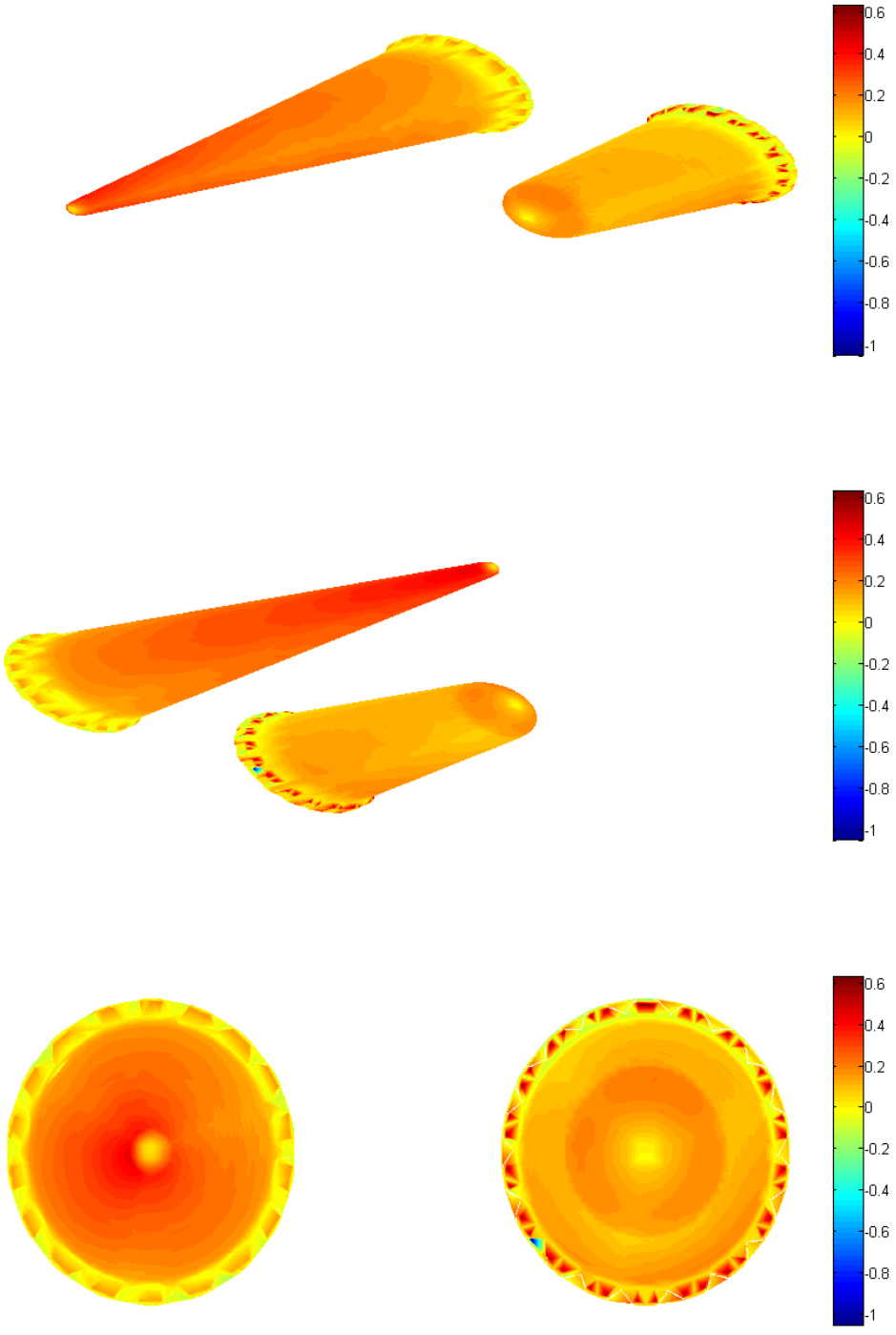

Figure 2-4. Results of coordinate measuring machine analysis on the DRE nosetips. The color scale indicates deviation, in millimeters, of the manufactured part from the original design.

mm DRE nosetip were measured in a Mitutoyo Crysta-Apex C-7106 coordinate measuring maching (CMM) for deviation from their nominal measurements. Figure 2-4 shows the results of this analysis with the total deviation of each point's measured value relative to the nominal CAD model displayed in terms of an interpolated color-map projected onto the CAD nosetip surface. Both nosetips are displayed with the same color scale to give a sense of the relative amount of deviation between each part. The scale ranges from a positive deviation of 0.62 mm (higher than the CAD surface) to a negative deviation of -1.08 mm (lower than the CAD surface).

The shorter 6.35-mm nosetip primarily deviates around the discrete roughness elements, whereas the longer 1.59-mm nosetip meets tolerances around the roughness elements but deviates on the conical section near the blunted tip. The largest deviation, an indentation of nearly 1 mm due to a tool mark, is on the blunter nosetip and is visible in Figure 2-4. The largest deviations from the nominal surface all occur around the discrete roughness elements of the blunter nosetip, and, with the exception of the aforementioned tool mark, skew toward positive deviations of about 0.5 mm. The mean absolute deviation of the blunter nosetip is 0.17 ± 0.11 mm. A modified approach was used when cutting the discrete roughness elements for the longer, less blunt nosetip, which resulted in much better adherence to the nominal design, as demonstrated by the very low deviation values in Figure 2-4. The primary source of deviation for the longer nosetip is a positive deviation along the conical surface past the spherical nose. This deviation is widespread and slightly asymmetric. However, the 1.59-mm radius DRE nosetip's maximum positive deviation is 0.43 mm, and the maximum negative deviation

is -0.16 mm, neither of which is as extreme as the blunter nosetip. The longer nosetip's mean absolute deviation is 0.13 ± 0.08 mm.

2.1.2 Quasi-random periodically distributed roughness nosetip

The final 6.35-mm nosetip features quasi-random periodic distributed roughness generated in a fashion similar to that of Downs *et al.* (2008). The advantage of quasi-random periodic distributed roughness is that it simulates a naturally-occurring distributed rough surface but does so in a mathematically definable fashion that features a particular disturbance wavelength and its harmonics. Quasi-random roughness is generated for a 30° arc in Fourier space by randomly selecting amplitude and phase coefficients for the series:

$$k(x,\theta) = \sum_{n=1}^{N}\sum_{m=1}^{M} A_{n,m} \cos\left[\left(\frac{2\pi n x}{\lambda_k \cos\gamma_c}\right) + mK\theta + \Phi_{n,m}\right] \tag{2.1}$$

where x is the axial coordinate measured from the tip of the blunt cone; θ is the azimuthal angle around the sphere-cone nosetip; γ_c is the half-angle of the cone; and k projects in the direction normal to the nominal smooth nosetip surface. The longest wavelength of the roughness is λ_k = 10.16 mm and the quasi-random roughness pattern repeats over two 150° arcs, which are separated by two 30° nominally smooth arcs. K = 12 to ensure 30° periodicity and $N = M = 5$ to limit the roughness near the stagnation point to manufactuable values. The $A_{n,m}$ coefficients are selected from a half-normal distribution and scaled such that the maximum amplitude is 0.635 mm. $A_{n,m}$ coefficients for which $n^2 + m^2 > 5^2$ are set to zero to maintain isotropy. Phases are randomly selected from a uniform distribution between 0 and 2π.

After generation, the roughness is numerically applied to the nominally smooth nosetip surface and three windowing procedures are applied. The first brings *k* smoothly to zero over the 15° arcs on the outside of each 150° rough arc, and the second smoothes *k* to zero over the final 10.5% of the nosetip's length. The purpose of these sections is to smoothly ramp into and out of the rough sections. The third windowing procedure is applied only to the spherical portion of the nosetip, and, while it does not smooth *k* to zero, it modulates the size of the roughness based on its proximity to the stagnation point. This was found to be necessary for the creation of manufacturable surfaces. The

Figure 2-5. The 6.35-mm quasi-random periodic distributed roughness nosetip.

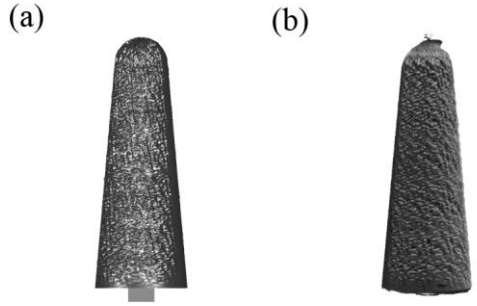

Figure 2-6. Comparison of designed and manufactured quasi-random periodic distributed roughness. The snapshots are intended for qualitative comparison of the (a) designed and (b) photocaptured roughness fields.

final roughened nosetip was generated in stainless steel (17-4 PH) via direct metal laser sintering by Forecast 3D and is visible in Figure 2-5.

After manufacture, the distributed roughness nosetip was studied to ensure that the desired wavelengths and roughness amplitudes were present in the final product. The manufactured nosetip was quantified using a photocapture technique that constructed a three-dimensional digital model of the nosetip from a series of photographs. The freely available Autodesk 123D Catch software was used for the digital reconstruction. The manufactured roughness was extracted from the digital model by performing a best fit to the nominal smooth nosetip surface. The extracted photocaptured roughness was then compared with the as-designed roughness extracted from the digital model given to the manufacturer. Images of the photocaptured roughness and as-designed roughness are shown in Figure 2-6 for comparison. Qualitatively, they appear quite similar. The spectra of the photocaptured roughness,

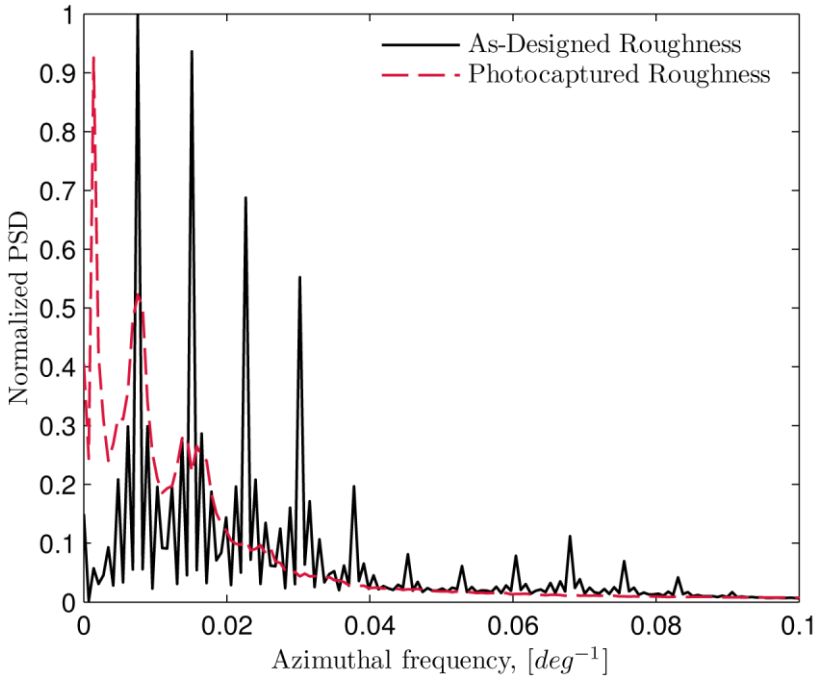

Figure 2-7. Spectra of the designed and manufactured quasi-random distributed roughness.

seen in Figure 2-7, showed the same harmonic behavior as that of the as-designed roughness for the first several harmonics. Measures of the average roughness amplitude also showed good agreement, with both models having a k_{rms} = 0.11 mm:

$$k_{rms} = \sqrt{\frac{1}{N}\sum_{i=1}^{N} y_i^2} \tag{2.2}$$

where y_i is the vertical deviation of the roughness from the nominal surface and N is the total number of measurements. Thus, the manufactured nosetip's distributed roughness shows acceptable agreement with the as-designed roughness.

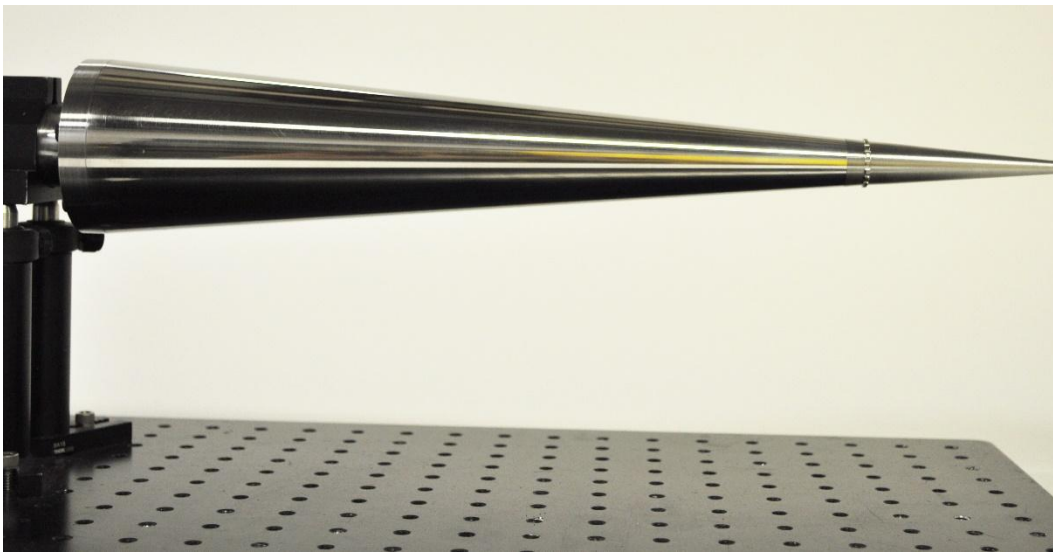

Figure 2-8. TG Cone model in its experimental configuration.

2.1.3 Experimental configuration

As noted earlier, although all five nosetips were designed and manufactured with transient growth experiments in mind, only the 1.59-mm DRE nosetip was utilized in the final experiments. In the interest of thoroughly documenting the experiment, the following is a description of the TG Cone model as it was used in the experiments. The 1.59-mm DRE nosetip was screwed into the frustum using Loctite Threadlocker Blue 242 on the threads for added security. The cone was mounted to a sting used to project the model forward into the nozzle. The sting's circular collar abuts the base of the frustum and matches its diameter (as they were machined together). It does not extend the cone's 5° half-angle; its side face is parallel to the cone axis, as seen in Figure 2-1. The sting collar is 12.7 mm thick. An image of TG Cone configuration used in the experiments is shown in Figure 2-8. Additionally, Figure 2-9 shows macro images of the

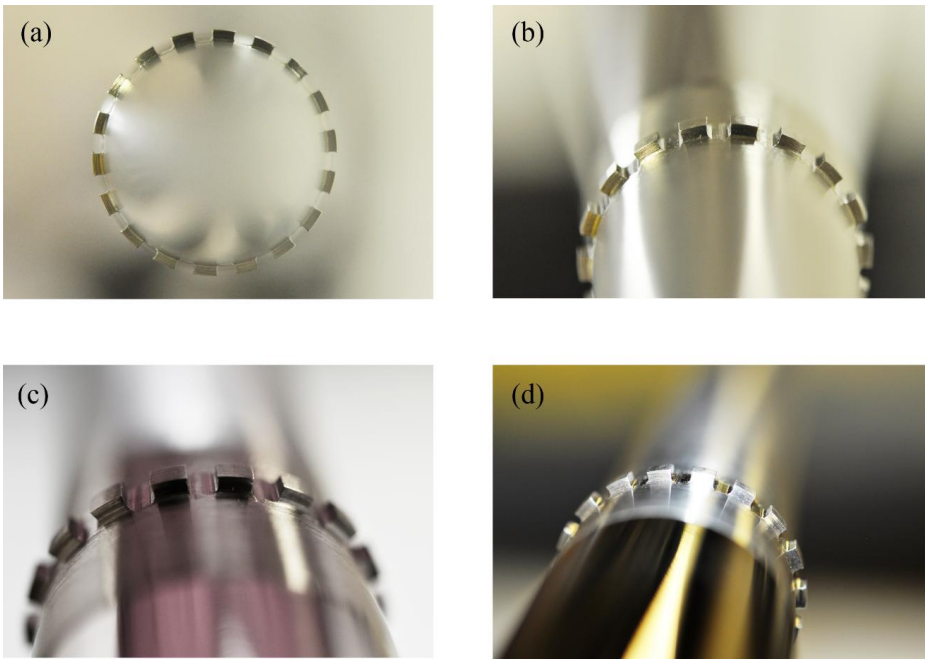

Figure 2-9. Additional views of the discrete roughness elements. Images show the 1.59-mm radius DRE nosetip from (a) forward, (b) forward and above, (c) behind and above, and (d) behind and skewed starboard.

discrete roughness elements on the 1.59-mm nosetip from various angles, with particular focus on the regions behind which measurements occurred.

2.2 Companion simulations

Many of the advances made in understanding transient growth at low-speeds—and, indeed, in understanding stability and transition in general—have come about through careful collaboration between experimentalists, computationalists, and theorists. To this end, direct numerical simulations complementing the present experiment are underway in collaboration with researchers at the University of California, Los Angeles and Texas A&M University. Soon, DNS data for the geometry will be available and will enable comparisons to more sophisticated data, as discussed later in §6.3.

In planning the experiment, a self-similar compressible boundary layer equivalent to that of a sharp, 5° half-angle cone (at zero angle of attack) was used. The basic state was generated for a grid 800 points tall at 200 streamwise stations located between the roughness array and the end of the cone. Three cases, matching the nominal Mach number, stagnation temperature, adiabatic wall temperature ratio, and Reynolds numbers of the experiment, were considered. (Details of the experimental conditions are given in §4.1.) Optimal disturbance calculations were performed with the code described in Zuccher *et al.* (2006) and Zuccher *et al.* (2007) using a full energy norm definition at the outlet. Figure 2-10 shows the calculated transient growth factors as a function of wavenumber. For all Reynolds numbers, the optimal disturbance growth factors peak for a wavelength between λ_k and $\lambda_k/3$, indicating that the roughness array's spacing is near the optimal azimuthal wavelength, as desired. These self-similar basic state and optimal disturbance calculations are referred to later when describing the experimental basic state (§4.2), analyzing the disturbance energy norm (§4.5), and evaluating a transient-growth based transition location correlation with respect to the experiment (§4.6).

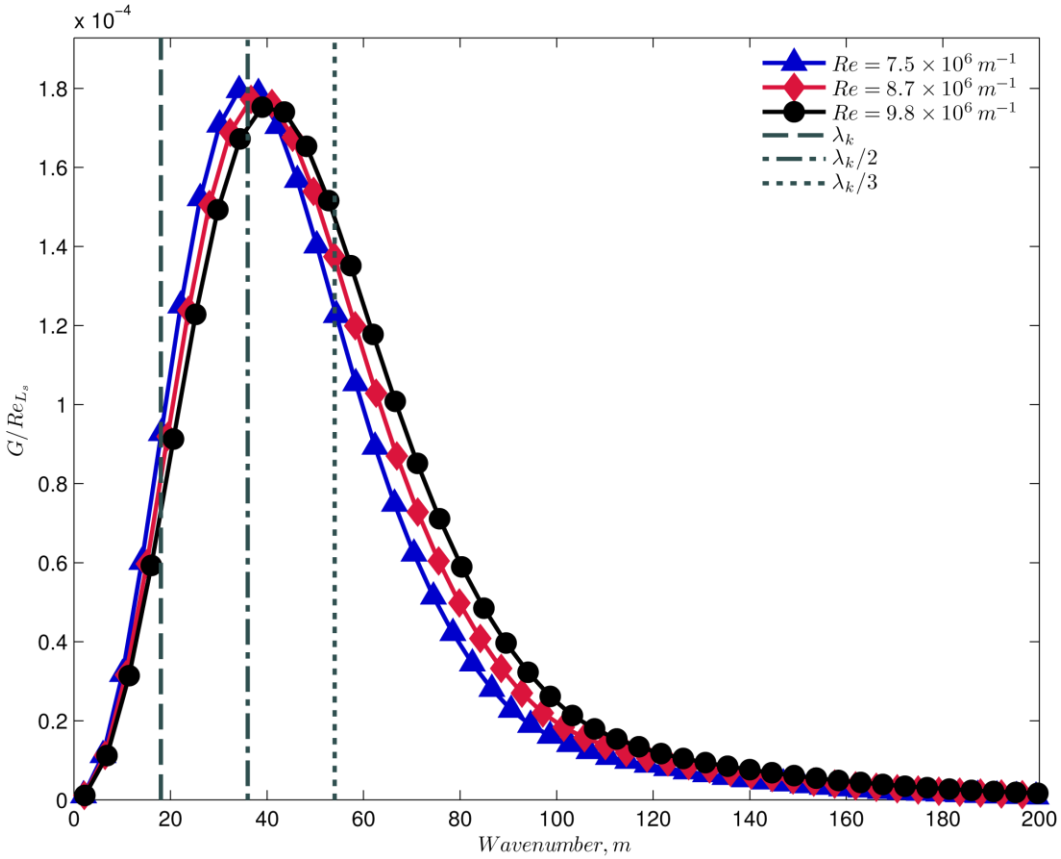

Figure 2-10. Optimal disturbance growth factors for a sharp, 5° half-angle cone at the experimental conditions. The growth factors are scaled using Re_{L_s}, the Reynolds number based on edge conditions and the sharp length of the cone.

3. FACILITY AND METHODS[*]

Previous subsonic experiments on transient growth measured the evolution of disturbances in the wake of periodically-spaced cylindrical roughness on a flat plate using dense hot-wire-anemometry scans in spanwise planes at multiple streamwise positions (White 2002, White *et al.* 2005, Ergin and White 2006). In many respects, the current work is guided by the methods of those earlier experiments. Adapting low-speed techniques and analysis to high-speed experiments is not straightforward, and several challenges were addressed in doing so. This chapter discusses some of those challenges through description of the experimental facility, the instrumentation, and the methodology used in the current work.

3.1 Mach 6 Quiet Tunnel

No single ground facility can emulate all aspects of hypersonic flight (Schneider 2008). The chief concern in a stability experiment is whether the freestream disturbance environment of the wind tunnel is comparable to that of flight. In conventional noisy wind tunnels, the turbulent boundary layer on the nozzle wall radiates disturbances along Mach lines onto the model, thereby contaminating the incoming flow field. Quiet hypersonic wind tunnels are defined by an absence of measurable turbulent intermittancy in the region of uniform freestream flow (Wilkinson 1997).

The experiments described here were conducted in the Mach 6 Quiet Tunnel (M6QT) at Texas A&M University. The M6QT facility is housed in the TAMU National

[*] Portions of this section are reprinted with permission from "Roughness-Induced Transient Growth on a Hypersonic Blunt Cone," by Sharp, N. S., and White, E. B., 2014. *AIAA Paper 2014-0432*, Copyright 2014 by the American Institute of Aeronautics and Astronautics, Inc.

Aerothermochemistry Laboratory (TAMU-NAL) and shares much of its infrastructure and instrumentation with other facilities within the laboratory. As such, much of the work done in establishing the wind tunnel, its infrastructure, instrumentation, and procedures is described elsewhere by the researchers responsible for their development. The present chapter is intended to include only the information most relevant to the current work and frequent references are made to sources where more detailed and thorough descriptions of specific topics are available.

3.1.1 Construction and infrastructure of the Mach 6 Quiet Tunnel

The Texas A&M Mach 6 Quiet Tunnel is the present incarnation of a facility originally designed and built at NASA Langley Research Center, where it was known as the Mach 6 Pilot Quiet Nozzle in the Nozzle Test Chamber. It was developed in the late 1980s and early 1990s as a low-disturbance hypersonic wind tunnel suitable for use in boundary-layer stability experiments as part of the National Aerospace Plane venture. Wilkinson (1997) discusses some of the historical context around the facility's development as well as the early studies in second-mode instability conducted in the tunnel while at NASA. After these studies, the facility was disassembled and stored until 2005, when it was moved to Texas A&M. Hofferth *et al.* (2010) and Hofferth (2013) describe the facility's reestablishment and infrastructure in detail.

The low-disturbance freestream environment of the M6QT results from several factors in the nozzle's design that help maintain laminar flow on the nozzle wall. An annular bleed slot upstream of the throat is connected through four valves to the diffuser. When these valves are opened during a run, the low pressure of the diffuser provides

suction that removes the contraction-wall boundary layer. This establishes a fresh, laminar boundary layer on the nozzle wall. The nozzle has a throat 25.4 mm in diameter and is 1.01 m long. Its exit diameter is 190.3 mm. The expansion contour of the nozzle is gradual, using a straight-wall region downstream of the throat to delay the onset and growth of Görtler vortices. The interior of the nozzle is electroplated with an alloy of nickel and 10% phosphorus for hardness and has been polished, most recently in Fall 2010-Spring 2011, to reduce the likelihood of premature nozzle wall transition due to roughness. Description and details of the polishing and its effect on M6QT performance are given in Hofferth and Saric (2012) and Hofferth (2013). Together the bleed-slot boundary-layer suction, gradual expansion, and polished finish of the M6QT nozzle enable the facility's low-disturbance test environment. Flow quality details are presented later in §3.1.4.

Aside from the nozzle, the other major components of the M6QT facility are its settling chamber, contraction, test section, and diffuser. Detailed descriptions of each component as well as the tunnel's instrumentation are found in Hofferth (2013) and only an overview is given here. The settling chamber consists of two major segments, the first of which contains a series of mesh screens to condition incoming flow. The second section of the settling chamber is empty. The settling chamber is equipped with an Omega K-type thermocouple and an MKS Baratron 615A High-Accuracy Capacitance Manometer to measure stagnation temperatures and pressures, respectively.

Downstream of the settling chamber, the 305-mm long contraction region accelerates flow with a contraction ratio of 132.25. As described in Hofferth (2013), the

contraction mates with the nozzle to create the toroidal region in which suction removes the incoming boundary layer prior to the nozzle.

Following the nozzle is the stainless-steel test section chamber which houses the nozzle, test jet, and diffuser in an enclosed free-jet configuration. The test section is 0.81 m in height and width, excluding corner relief, and is equipped with access doors on the floor, ceiling, and both sides. Each door is equipped with a 200-mm window for optical access. Additional access ports allow instrument cable penetration through Conax fittings that prevent vacuum leakage.

Finally, the diffuser consists of an aluminum bell mouth with a 348 mm maximum diameter and 25º entrance angle located 1.8 nozzle exit diameters downstream of the exit plane. The bell mouth connects to a 203-mm diameter, 1.8 m long pipe that exhausts into a 609-mm diameter pipe connected directly to the vacuum source. Both the test section and diffuser are equipped with MKS 902 Piezo Vacuum Transducers to monitor their pressure.

As mentioned previously, the M6QT is integrated into shared infrastructure at the TAMU National Aerothermochemistry Laboratory (TAMU-NAL), where it operates in a pressure-vacuum blow-down configuration. The vacuum is supplied by a two-stage Fox-brand Venturi air-ejector system, which uses approximately 20 kg/sec of compressed air (10.2 atm) to generate a minimum starting back-pressure of 4 Torr. The run-time of the M6QT is largely determined by the ejector's high mass-flow requirements.

The notable difference from the infrastructure described in Hofferth (2013) is the compressors which supply air to the TAMU-NAL facilities. As of June 2013, air is

supplied by two Compair Reavell H5442 air compressors (130 SCFM each). This high-pressure air is filtered (99% efficient sub-micron), dried to -40°C in a twin-tower desiccant drier, and stored at 170 atm in a 23.2 m^3 tank. The ejector is supplied with air through a series of 4-inch carbon-steel pipe, whereas the tunnel air is supplied through a stainless-steel 2-inch line. The tunnel air supply is heated with a 500 kW Chromalox electric-resistance heater and filtered again to remove 99.9% of particles larger than 1 μm before entering the tunnel. Each supply pipeline is controlled with a Bray pneumatic actuator that starts and stops flow. A series of Stra-Val regulators provides the necessary control pressures to the ejector, and a separate series of Stra-Val regulators ensures delivery of the desired stagnation pressure to the wind tunnel. Temperature and pressure are monitored throughout the infrastructure using Omega-brand pressure transducers and K-type thermocouples.

Data acquisition for the M6QT is provided by two desktop computers, each equipped with National Instruments (NI) data acquisition hardware and controlled through custom LabVIEW software. During a run, the first system, "NAL-DAQ", monitors and records pressures and temperatures throughout the shared infrastructure and the M6QT. The system uses a NI USB-6255 M Series 16-bit multiplexing data acquisition board with 40 differential input channels to sample data at 1 kHz per channel, average to 10 Hz, and save all data to a spreadsheet for each run. The second system, "M6QT-DAQ", is adaptable to the specific needs of a given experimental campaign. For example, in the work described here, the M6QT-DAQ controlled and monitored motion control by the probe traversing mechanism (§3.1.3), executed and

recorded high-bandwidth Pitot (§3.2.1) or hot-wire-anemometry (§3.2.2) measurements, and tracked temperatures and pressures within the M6QT during runs. High-bandwidth acquisition uses an NI USB-6366 X-Series Data Acquisition board, which offers up to 2-MHz sampling across 8 differential channels with simultaneous sampling. Further detail on both data acquisition systems and their capabilities is given in Hofferth (2013).

3.1.2 Mach 6 Quiet Tunnel operation

One of the major challenges of conducting transient growth experiments at hypersonic speeds is the limited run-time of the facility relative to low-speed wind tunnels. To that end, it is useful to describe a generic run of the M6QT. Several modifications to this general procedure were made for much of the experimental campaign described in this work. These changes and the reasoning behind them are discussed later in §3.4.1.

To reach the nominal stagnation temperature of 430 K (required to avoid liquefaction of oxygen once hypersonic flow is initiated), the tunnel must be heated at subsonic speeds prior to initiating a run. The Chromalox heater supplying the incoming air was supplemented with Ogden Mighty-Tuff electric-resistance band heaters located in the fiberglass-blanket-insulated settling chamber. For the initial run of a day, this convective pre-heating typically requires 10-15 minutes of subsonic airflow through the wind tunnel. Pre-heating for subsequent runs typically lasts less than 5 minutes.

Once the settling chamber reaches the appropriate temperature and the tunnel's pressure regulators have been set to the desired stagnation pressure, the tunnel air supply valve is closed and the Chromalox heater is shut off. Final safety and data acquisition checks are made. A run is initiated by activating both stages of the ejector system. After

several seconds, the tunnel will be evacuated to approximately 10 Torr as far upstream as the settling chamber pressure regulator. At this point, the tunnel supply ball-valve just upstream of the heater is actuated, filling the tunnel with the nominal stagnation pressure and starting hypersonic flow.

The tunnel is started with the bleed valves closed. Very quickly after flow is established in the tunnel, the bleed valves are opened, initiating suction upstream of the throat and generating a low-disturbance, "quiet" flow environment for freestream unit Reynolds numbers up to 11×10^6 m^{-1}. This begins the on-condition portion of the run during which experiments are conducted. The tunnel remains on-condition up to roughly 40 seconds while the tank discharges from 170 atm to 92 atm. When data collection is complete or the air supply reaches approximately 92 atm (whichever comes first), the run is ended by closing the bleed valves and shutting off the air supply to the ejectors, causing a loss of vacuum that unstarts flow in the tunnel. The main air supply valve to the tunnel is also closed, allowing the remaining air in the line to exhaust subsonically through the tunnel.

3.1.3 Probe traversing mechanism

A linear two-axis probe traversing mechanism with a 400 mm by 200 mm range of motion is mounted to the ceiling of the M6QT test section. The components of this system were supplied by Aerotech, Inc. and are described in detail in Hofferth (2013). The system is capable of motion accurate to $O(5\ \mu m)$ and is controlled through a custom software interface in M6QT-DAQ's LabVIEW program (§3.1.1). The traverse

mechanism can be adapted to several configurations, as described by Hofferth (2013), but was primarily used for this work in an azimuthal configuration.

In this configuration, a rotating platform on two bronze sleeve bearings attaches to the model's sting mount. The bearings are located on either side of the clamping sleeve that fastens the model to the tunnel. Because the sting mount and cone were machined together, the platform rotates concentrically about the cone. Atop the platform is a wedge-shaped, fixed-angle (10°) probe holder which affixes a probe in a single axial and wall-normal position. The probe's height is controlled manually with custom shims (in 0.5 mm, 0.76 mm, and 4.76 mm thicknesses).

Also attached to the platform is a wedge-shaped riser and clevis pin that connect to a bar linking the platform to the linear traverse. The linkage joints are tightly toleranced to minimize slop in mapping the linear motion into azimuthal motion. Depending on one's choice of anchor point on the linear traverse and the length and angle of the linkages, the 200 mm of linear travel can be transformed into approximately 55° degrees of azimuthal motion with a stepping resolution of ~0.01°. The azimuthal motion's center relative to the cone varies with anchor point and linkage angle, making it possible to measure azimuthal regions larger than 55° by using multiple linkage configurations over the course of an experimental campaign.

Each time the linkage was adjusted, the azimuthal motion of the platform was measured relative to the traverse's linear motion using a digital inclinometer and was calibrated to a quadratic fit. Each calibration contained more than 40 points, representing both directions of motion, and the quadratic fits had R^2 values greater than 0.999. An

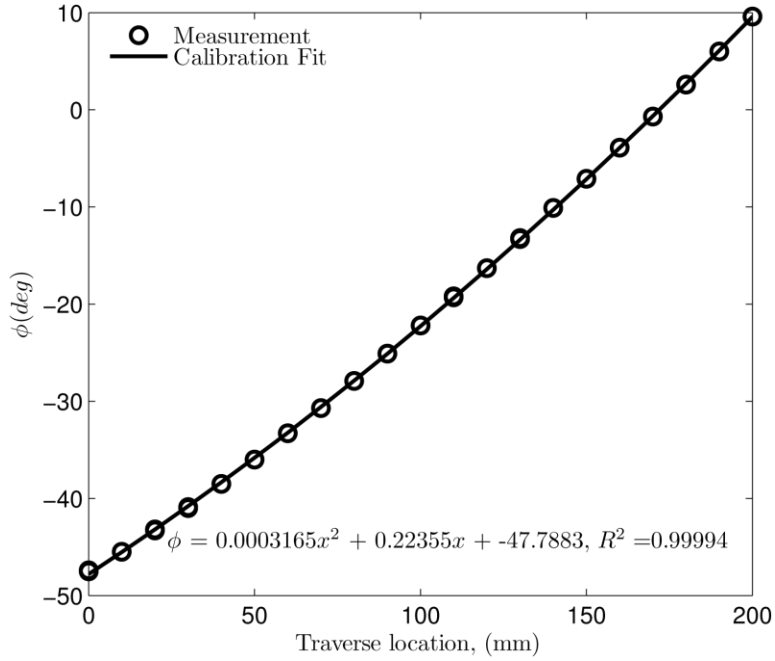

Figure 3-1. Example calibration fit of azimuthal rotation to the linear traverse's motion.

example calibration fit is shown in Figure 3-1. The calibration was then used to generate linear motion profiles corresponding to the desired azimuthal motion for a specific run.

Probe height was measured optically using a Keyence LS-7030R optical micrometer with an accuracy of ±2 μm and a minimum detectable gap of 0.15 mm. The device attaches to a precision, two-axis translation stage mounted to a sleeve that clamps around the outer sheath of the M6QT nozzle. Hofferth (2013) gives a detailed description of the procedure for optical height measurement. In the present work, probe heights were measured at several azimuthal positions; typical variation in the measured probe height was less than 15 μm over a 50° azimuthal range. The recorded probe height corresponds to the physical center of the probe's forward-most cross-section. Although

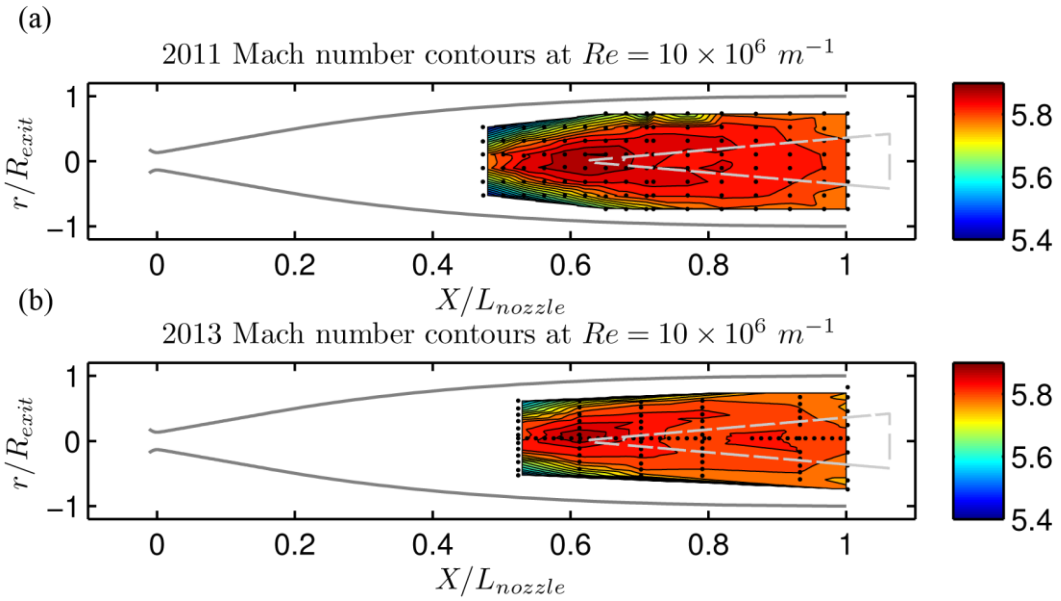

Figure 3-2. Mach number contours inside the M6QT nozzle. Data shown are results from a) the 2011 survey by Hofferth (2013), and b) the present 2013 survey. Dots indicate Pitot measurement locations. Color scales and contour levels are identical in both plots. Outlines of the M6QT nozzle contour and the experimental model are included for visual reference.

probe heights were measured with the flow off, magnified schlieren video of the probes before, during, and after a run showed no measurable movement.

3.1.4 Mach 6 Quiet Tunnel flow quality assessment

Standard operating procedure of the M6QT includes occasional evaluation of flow quality inside the nozzle. In particular, more extensive flow quality evaluation is warranted after any substantial modifications to the tunnel and/or its infrastructure. In the six months prior to the experimental work described in this document, a pair of Chicago Pneumatic air compressors were removed and replaced with Compair Reavell air compressors and significant alterations and improvements were made to the

surrounding infrastructure. This left the M6QT out of commission from January 2013 through June 2013. In bringing the tunnel back online, a spatial survey of freestream mean and fluctuating pressures was carried out using a Kulite XCEL-152-10A in a Pitot configuration. The experimental configuration and procedure matched that in the survey reported by Hofferth and Saric (2012) and Hofferth (2013).

The 2013 flow evaluation survey was less extensive than the 2011 survey by Hofferth (2013). A pressure sweep at the centerline of the nozzle exit plane confirmed quiet flow up to a freestream unit Reynolds number of $Re = 11 \times 10^6$ m^{-1}, which is consistent with past performance. A spatial survey of the centerline plane inside the nozzle was conducted at $Re = 10 \times 10^6$ m^{-1}, the highest Reynolds number used in the current experimental work. A comparison of the Mach number contours from the present survey and the previous survey by Hofferth (2013) is shown in Figure 3-2. The M6QT nozzle contours and an outline of the TG Cone model are included for reference. Black dots indicate the probe measurement locations used to interpolate the displayed contours. Identical color scales and contour levels are shown for both surveys. The data show good agreement to within the limitations of interpolation.

Normalized Pitot pressure fluctuations are the major indicator of flow quality for a quiet tunnel (Wilkinson 1997, Hofferth 2013). These normalized fluctuations are defined as a percentage ratio of the temporal root-mean-square (rms) of the Pitot pressure fluctuations to the mean freestream Pitot pressure. Contours of normalized Pitot pressure fluctuations for both freestream surveys are shown in Figure 3-3. Once again, agreement is good between the current and previous survey. In Figure 3-3 the color scale

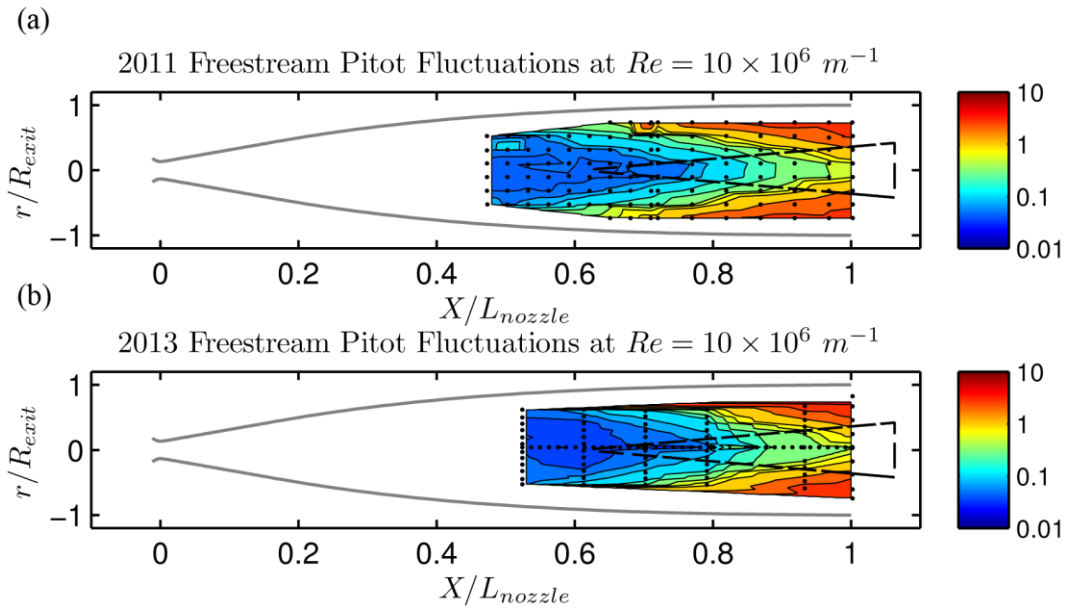

Figure 3-3. Normalized freestream Pitot fluctuations inside the M6QT nozzle. Data shown are results from a) the 2011 survey by Hoffeth (2013), and b) the present 2013 survey. Dots indicate Pitot measurement locations. The logarithmic color scale and contour levels are identical in both plots. Outlines of the M6QT nozzle contour and the experimental model are included for visual reference.

is logarithmic to highlight the variations in freestream fluctuations with axial position. Pressure fluctuations of 0.1% impinge on the cone model roughly 80% of the way down the nozzle at $X/L_s = 0.45$. Pressure fluctuations reach 1% at approximately $X/L_s = 0.71$. By comparison, the roughness array (§2.1.1) is located at $X/L_s = 0.25$, well upstream of any substantial freestream pressure fluctuations.

Typical freestream fluctuation levels in a conventional hypersonic wind tunnel range from 1-3%.

Figures 3-2 and 3-3 indicate that facility's performance post-TAMU-NAL expansion is consistent with past M6QT performance. They also demonstrate that the

roughness array is located inside the quiet flow region and that the roughness-perturbed boundary layer experiences a substantial region of quiet flow before any significant freestream pressure fluctuations can be expected to impinge on the cone.

3.2 Experimental diagnostics and instrumentation

The M6QT tunnel and its data acquisition infrastructure include provisions for many diagnostics such as hot-wire anemometry, Kulite pressure transducers, schlieren photography, and more. Many of these systems and capabilities are described in detail in Hofferth (2013). The present experimental study (excluding the freestream survey of flow quality discussed in §3.1.4) utilized a Kulite pressure transducer in a Pitot tube configuration as the primary diagnostic with only preliminary measurements conducted using hot-wire anemometry. Both diagnostics are discussed in the following sections, along with description of the thermocouple used to monitor the model's wall temperature. A comparison of hot-wire and Pitot measurements in the experiment is given later in §3.5.

3.2.1 Pitot tube measurements

The main diagnostic for the current work is a Pitot probe containing a Kulite XTE-190 pressure sensor. These instruments are miniature strain-gage sensors mounted on a thin silicon diaphragm. The sensor element is located inside a cylinder 3.8 mm in diameter that widens aft of the element into a miniature threaded housing that can be easily installed into a probe body. The small size and mass of the sensor element allows the pressure transducer to respond quickly, with a nominal resonant frequency of 240 kHz.

The XTE-190 has a full-scale pressure range of 1.7 bar absolute (25 psia) and is temperature-compensated for a range including operating temperatures in the M6QT.

The probe body was designed and fabricated in-house. The exterior contour's taper is formed by telescoping several diameters of stainless-steel tubing and silver-soldering them together. A machined stainless-steel adapter is silver-soldered into the downstream end so that the threaded XTE-190 fits into the body. The internal volume of the probe body is minimal in order to maximize frequency response. After an initial transient during tunnel start-up, the Pitot probe responded to variations in pressure between azimuthal measurement positions on a time-scale smaller than the time required for the traverse to move between positions. The mouth of the Pitot tube is approximately elliptical in shape, with the major axis aligned in the azimuthal direction and the minor axis in the vertical direction. The outer diameter is 3.6 mm horizontally and 2.0 mm vertically. The inner diameters are 3.0 mm and 1.4 mm, respectively.

An Endevco Model 136 signal conditioner supplied the transducer with 10V DC power and amplified its full-scale output signal of 100 mV. The full-scale output signal was sampled at 500 kHz and acquired using a National Instruments 16-bit data acquisition system. It was discovered mid-campaign that the Endevco Model 136 adds broad band electronic noise in the 20-50 kHz range. Hofferth (2013) traced this to the switching-type DC power supply used by the device. Because transient growth is a steady phenomenon the additional noise was deemed a tolerable limitation. Later in §3.5 a comparison is made between Endevco-powered measurements of pressure fluctuations and the fluctuations measured by hot-wire anemometry.

The Kulite XTE-190 pressure transducer's response is linear throughout its compensated temperature range, including the operating temperature of the M6QT. However, the devices are known to have a slight variation in the zero-offset value of their calibration with sensor temperature. When a static calibration was performed at room-temperature, the device's sensitivity differed by only 1% from the manufacturer-reported value. The difference between the calibrated room-temperature zero-offset value and the high-temperature zero-offset value set in the tunnel was less than 0.15 psi. Effectively, the zero-offset value's temperature dependence may be treated as a systematic bias error and is accounted for through uncertainty propagation.

3.2.2 Hot-wire anemometry measurements

As noted previously, preliminary measurements were conducted using uncalibrated hot-wire anemometry. The principle behind hot-wire anemometry is the convective cooling of a heated, active wire only a few microns in diameter. The technique has excellent spatial resolution and frequency response, but the sensors themselves are very delicate. Unlike the second-mode or crossflow instabilities, measuring transient growth does not require a high-frequency response, and this, combined with the robustness of the Kulite pressure transducer, motivated the selection of Pitot measurements as the primary diagnostic in the present work. Nevertheless, a brief overview of the hot-wire anemometry system and sensors used is given here. Greater attention to the construction, fabrication, and operation of the sensors is given in Hofferth (2013) and readers are referred there for those details. Hofferth (2013) also discusses a method for calibration

of multiple hot-wire sensors at a time in the M6QT. This capability is under development but was not yet available at the time of the experiment.

The preliminary measurements utilize hot-wire anemometry using an A.A. Lab Systems AN-1003 constant temperature anemometer (CTA) system. Hot-wires are operated at a single, constant overheat ratio ($\tau \sim 1$), resulting in sensitivity primarily to mass flux (Smits *et al.* 1983). Hot-wire probe bodies and sensors are fabricated and repaired in-house. The sensor used in this work was fabricated by the author using one of the straight probe bodies built and described by Hofferth (2013). The active wire element consisted of a Wollaston wire with a platinum-10% rhodium core of 5-μm diameter encased in silver approximately 50 μm in diameter. The Wollaston wire was soldered to stainless-steel insect pins, the tips of which were nominally separated by 1.2 mm. The center portion of the wire core was exposed by etching with a drop of dilute nitric acid. The active length of the wire was 0.6 mm, giving a length-to-diameter ratio of 120. Ideally, the length-to-diameter ratio of a sensor should be approximately 150 to avoid end conduction effects and provide adequate sensitivity (Smits *et al.* 1983).

After construction, the hot-wire sensor and anemometer bridge were tuned at test conditions using a square-wave injection, according to the procedure given in Hofferth (2013). A PC-based oscilloscope measured impulse input and wire response. Analysis showed the frequency-amplitude transfer function had a -3dB roll-off at approximately 100 kHz for the sensor used in the preliminary measurements shown in §3.5.

Hot-wire data were sampled at 500 kHz with 200 ms of residence time at each point in the boundary layer.

3.2.3 Thermocouple measurements

The TG Cone model as described in §2.1 and used in the experiments was not built with any embedded instrumentation, although it was designed to enable retro-fitting with sensors in the future. The cone is thick-walled but hollow. In the current work, the wall-temperature was monitored by means of an Omega SA1-K fine-wire K-type thermocouple, which was mounted to the surface of the model at $X/L_s = 0.94$ using high-temperature aluminum tape. Azimuthally, the thermocouple was attached 180° opposite of the measurement region. Data from the thermocouple were acquired using the NAL-DAQ acquisition computer described in §3.1.1. The M6QT facility's 40-second run-time is insufficient for the cone to equilibrate to adiabatic conditions, and the thermal inertia of the thick-walled model is sufficiently high that the cone's wall temperature remains essentially constant (variation of ~0.1%) throughout a run. Although wall-temperature did not change significantly during a run, it was important to monitor the adiabatic wall-temperature ratio between runs, as will be discussed in §3.4.1.

3.3 Model alignment

Since the M6QT's low-disturbance freestream environment exists inside the nozzle, the cone model is installed with all but the aftmost 51 mm of the model within the nozzle. This places the model's nosetip, roughness array, and frustum joint inside the region of quiet-flow, as shown in Figure 3-3.

The cone model was installed nominally at zero angle of attack in the present study. The model's misalignment relative to the test section was quantified using a Keyence LT-8120 Confocal Laser Displacement Sensor system attached to the test

chamber's two-axis traversing mechanism, according to the procedure described by Hofferth (2013). The Keyence device measures height differences with maximum range of 2 mm and a 0.2 μm resolution. By scanning the upper surface of the nozzle's outer sheath and the cone's support shaft with the LT-8120, a three-dimensional point cloud of each surface was produced in the reference frame of the traverse's axes. Axial slices of the point cloud were then best fit to circles of known diameter (38.1 mm for the cone shaft and 235 mm for the nozzle sheath) to determine the position of the circle centers at each axial location. Pitch and yaw angles of the nozzle and cone relative to the traverse axes were determined from these center locations, and, by comparing the traverse-relative alignments of the cone and nozzle, the alignment of the cone relative to the nozzle flow was determined.

This method assumes the flow is concentric with respect to the nozzle sheath and that the cone model is concentric with respect to its support shaft. The latter assumption is known to be correct because the cone model was machined and ground using the same support shaft used in the experiments. The former is reasonable, given the tolerances to which the nozzle was produced.

The cone model was installed in the test section twice during the experimental campaign. In the first installation, the model misalignment was measured as 0.20° in pitch (nose up, bottom side windward) and 0.28° in yaw (nose left, viewed looking upstream). In the second installation, the model misalignment was 0.28° in pitch (nose up, bottom side windward) and 0.55° in yaw (nose left, viewed looking upstream). In both installations, measurements occurred along the upper half of the cone, meaning

these rays were in a slightly leeward, three-dimensional condition. Comparisons of data at the same conditions between the installations showed no differences due to model alignment relative to the nozzle.

3.4 Boundary layer scans

3.4.1 Condition matching between runs

In previous low-speed experiments, transiently growing streaks were identified using finely-spaced hot-wire measurements in spanwise planes through a boundary layer taken at multiple streamwise positions (White 2002, White *et al.* 2005, Ergin and White 2006). The measurement planes were wide enough to capture as many as eight roughness elements from the periodic array, and the effectively unlimited run-time of subsonic wind tunnels enabled experimenters to capture data in dense grids at many streamwise positions during the same run and, thus, at the same conditions.

The M6QT's capability of a 40-second run-time at constant conditions is unique among the hypersonic quiet facilities in operation at this time. It enables detailed boundary layer profiles that are not possible in other facilities; however, the run-time is not sufficiently long to emulate the dense measurement grids of subsonic transient growth experiments. Moreover, the current compressor capacity is limited to refilling the air storage tank at a maximum rate of approximately 20 atm/hr, meaning that several hours of refilling are necessary between runs. The total number of potential runs between facilities using the shared TAMU-NAL infrastructure is roughly 5-7 runs per day in its current configuration.

Given these limitations, matching conditions between individual runs of the M6QT was vital to constructing useable data sets for measuring transient growth. Settling chamber pressure and temperature were monitored during each run and controlled to within 2-3% of their nominal value. This resulted in freestream unit Reynolds numbers that varied by less than ±1.5% between all runs across a given condition.

The largest challenge in condition matching between runs, however, was maintaining a constant ratio of model wall temperature to adiabatic wall temperature. In preliminary azimuthal measurements, significant variations in both hot-wire and Pitot measurements were seen between runs that varied from $T_w/T_{aw} = 0.92$ to $T_w/T_{aw} = 1.03$. This 11% difference in adiabatic wall temperature ratio resulted in boundary layer thicknesses doubling at a given azimuthal location. For comparison, Blanchard and Selby (1996) measured wall-cooling effects on a flared cone in the M6QT during its time at NASA Langley Research Center. In their experiments, they saw a 25.5% decrease in boundary layer thickness relative to an adiabatic-wall boundary layer at $T_w/T_{aw} = 0.67$. The large variations seen in the present work, therefore, were inconsistent with boundary-layer growth due to an 11% change in adiabatic wall temperature ratio. Instead, these variations are likely caused by the structures downstream of the roughness elements shifting as the cone wall temperature varies. Wheaton and Schneider (2013) also observed significant run-to-run variations in behavior for a near-critical roughness element that were traced to wall temperature differences between runs.

To avoid these temperature effects, a nominal adiabatic wall temperature ratio of $T_w/T_{aw} = 0.95$ was selected and runs were controlled to within ±1.5% of this value. Within this range, no azimuthal shifting of structures between runs was observed. The nominal value of $T_w/T_{aw} = 0.95$ was chosen for its convenience; it was the mode of the adiabatic wall temperature ratios observed in preliminary measurements. It corresponds to the typical cone temperature observed in back-to-back experiments conducted after the initial run of the day warms the M6QT settling chamber.

Because the cone model is not equipped with heating elements or a cooling system, its temperature could not be controlled independently of the M6QT stagnation temperature. Instead, the adiabatic wall temperature ratio was controlled through the timing of runs. This involved modification of the M6QT general operating procedure, as described in §3.1.2. In standard M6QT operation, the first run of a day is immediately preceded by a 10-15 minute subsonic pre-heating of the tunnel to bring the settling chamber from room temperature to its nominal stagnation temperature of 430 K. During this pre-heat, the cone model would also be heated from a room temperature value to a temperature exceeding the adiabatic wall temperature. To avoid this excessive heating of the cone model, the current work utilized a separate initial subsonic pre-heat prior to the first run of the day. During this pre-heat, the cone reached approximately 95% of its nominal run temperature and the M6QT settling chamber reached 85% of its nominal stagnation temperature. This was followed by a 20-35 minute pause, during which the cone temperature would relax to 91% of its nominal run-time value. Once the cone temperature reached this value, the normal M6QT operating procedure resumed with a

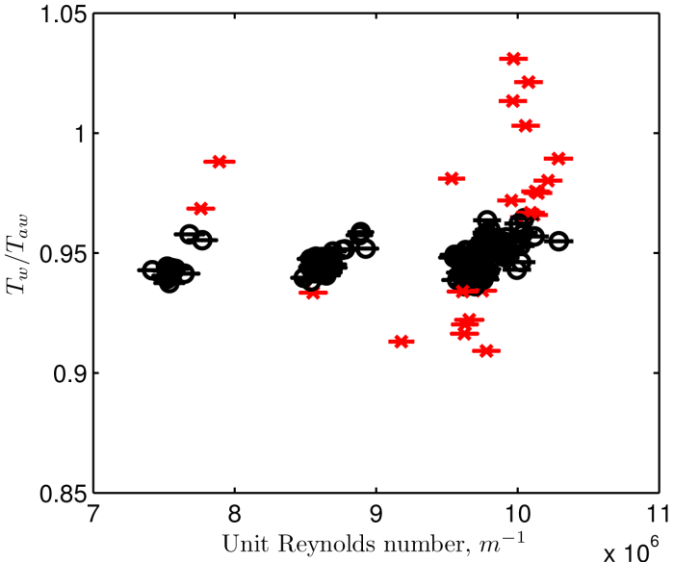

Figure 3-4. Run conditions for azimuthal Pitot tube measurements. Each datum represents a single run, with error bars indicating condition variation within the run. Black data points indicate on-condition runs, whereas red data points mark runs outside the acceptable range of freestream unit Reynolds number and adiabatic wall temperature ratio.

brief (< 5 minute) subsonic pre-heat to bring the settling chamber stagnation temperature to 430 K, followed immediately by a hypersonic run. Subsequent runs during the day were again initiated when the cone temperature reached 91% of its nominal run-time value and the air storage tank was sufficiently full to complete a run (>160 atm). If the cone temperature dropped below 91% of its run-time value before the air supply was refilled, an abbreviated separate subsonic pre-heat and pause were used to bring the cone back to temperature before initiating a new run. Using this procedure, the adiabatic wall temperature ratio of most runs was kept to $T_w/T_{aw} = 0.95 \pm 0.15$.

Figure 3-4 illustrates the Reynolds number and temperature conditions of every azimuthal Pitot measurement in the experimental campaign. Each point represents a single run; the error bars represent variation of conditions during that specific run. Data points in black are runs which matching the nominal adiabatic wall temperature ratio and freestream unit Reynolds number to within ±1.5%; data points in red fell outside the acceptable range. The Pitot measurement data reported in §4 represent 111 on-condition runs with a total estimated run-time of 46 minutes of hypersonic flow enabled by more than 550 compressor hours.

3.4.2 Scanning procedure

During a single run, data were collected along an approximately 55° azimuthal arc at a fixed height above the model, using the azimuthal traverse configuration described in §3.1.3. A typical run contained 27-34 measurements. The first several measurements occurred at the same azimuthal location and allowed the Pitot tube the necessary time for its initial start-up transient. As described in §3.2.1, after this initial transient, the Pitot tube's response was quicker than the time needed for the traverse to reach its next position. Data were then collected in 2° increments along the arc. When the traverse reached the end of the measurement region, it reversed direction and returned to the initial position, obtaining a handful of sparse measurements along the way. These data points were inspected after each run to ensure that no significant differences were observed between data taken at the beginning and end of a run, but the return-arc points were not included in subsequent analysis. Runs during which variations were observed were excluded from analysis and repeated.

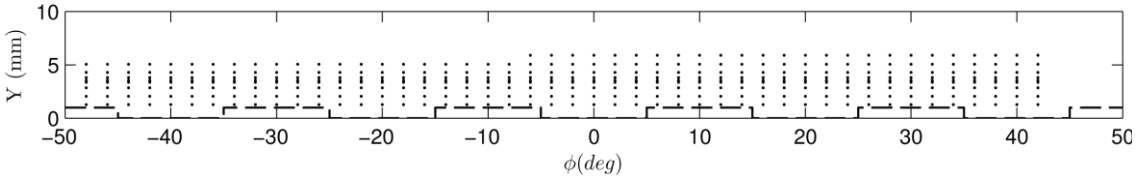

Figure 3-5. Example measurement grid for a combined data set. Black dots mark raw measurement locations, and dashed lines indicate projection of discrete roughness elements into the plane of measurement. The aspect ratio of the image is approximately the same as the aspect ratio of the measured region.

The usual direction of travel for the traverse was from starboard to port with respect to the model. In some runs the primary direction of motion was reversed, but no effect was observed on the results.

Between runs, the probe height was varied manually using shims capable of vertical increments as small as 0.5 mm. The probe's height was measured using the optical micrometer described in §3.1.3 and varied by less than 15 μm over the full azimuthal range.

The azimuthal extent of the measurements at a given streamwise location was increased by using two or more traverse configurations. As described in §3.1.3, moving the anchor point of the linkage between the linear traverse and the rotating platform shifted the 55° measurement arc relative to the cone. Measurements taken with these separate configurations included 6-10° worth of overlapping points, which were compared on a run-to-run basis to ensure adequate agreement.

In this way, data from 14-25 individual runs were combined to create a data set spanning an azimuthal plane extending approximately ±50° from vertical and spanning four full disturbance wavelengths. Figure 3-5 shows a scaled example of a typical

measurement grid after all runs for a given condition are combined. In subsequent analyses, the measured data were interpolated onto a standard grid with 1° azimuthal spacing and 0.25 mm vertical spacing using Matlab's TriScatteredInterp function.

3.5 Comparison of hot-wire and Pitot tube measurements

Two diagnostic techniques, the Pitot tube (§3.2.1) and the hot-wire sensor (§3.2.2) were considered for the present work. Each technique has its advantages and limitations. The Pitot tube is robust, which is ideal given the many runs necessary to construct a dataset (§3.4); however, its physical size (OD 3.6 mm wide and 2 mm tall) limits its spatial resolution. In contrast, the hot-wire sensor has excellent spatial resolution, but its durability is lacking. A comparison of both diagnostics is illustrative.

The methodology described in §3.4.2 was used to make measurements with both a Pitot tube and an uncalibrated hot-wire sensor for an azimuthal segment at $X/L_s = 0.94$ at $Re = 9.8 \times 10^6\ \mathrm{m}^{-1}$. These measurements are shown in Figure 3-6. Black dots indicate raw measurement locations, relative to each probe's center. Black lines are contours of mean measurement quantity (voltage for the uncalibrated hot-wire and total pressure for the Pitot) whereas the colored contours indicate the temporal root-mean-square (rms) variation of the measurement quantity. The size of each probe is shown to scale in the lower right corner of each contour plot. Note that the probes are scaled correctly relative to the data in the plot, but the plots themselves are not elongated to match the aspect ratio of the physical measurements.

Although the measurements are oversampled relative to the Pitot's size, the Pitot is still much smaller than the disturbance wavelength (between 0.27 and $0.3\lambda_k$ depending

on axial location) and captures the structure well azimuthally. Its temporal response also compares reasonably with the hot-wire: regions of high temporal rms correlate between the two probes. The Pitot does show vertical attenuation of the signal relative to the hot-wire, but its overall performance is adequate and its robustness is ideal, given the large number of runs necessary to acquire a complete dataset.

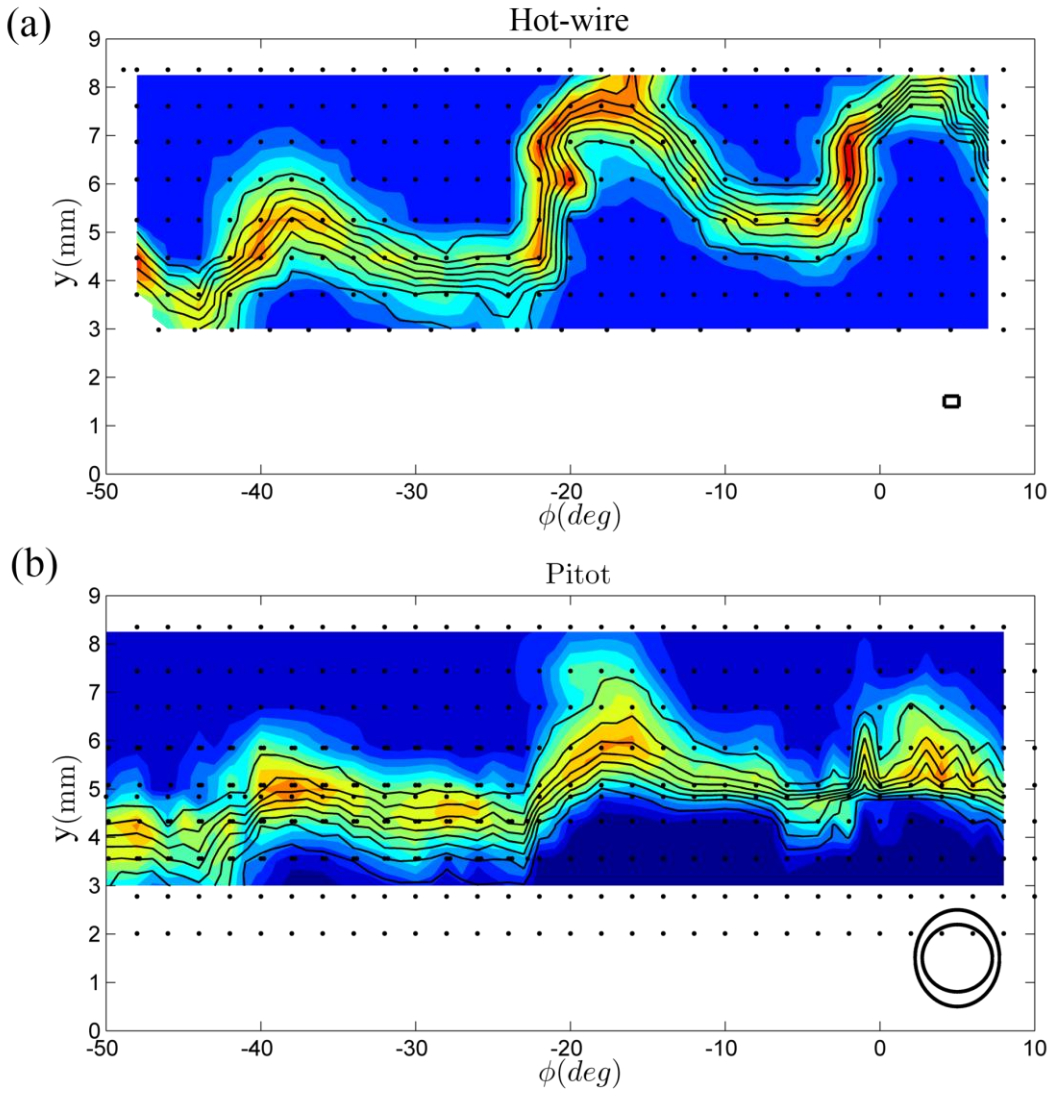

Figure 3-6. Comparison of hot-wire and Pitot measurements. Data show a) uncalibrated hot-wire and b) Pitot tube measurements at $X/L_s = 0.94$ for $Re = 9.8 \times 10^6$ m^{-1}. Dots indicate measurement location relative to probe center. Black lines are contours of measurement quantity (voltage for hot-wire; total pressure for Pitot). Colors indicate temporal root-mean-square fluctuations of measurement quantity. Probe sizes are included at the lower right to the scale of the image.

4. RESULTS AND DISCUSSION[*]

As the first experimental study of hypersonic roughness-induced transient growth, the current work occupies an interesting position. It owes much of its design, methodology, and goals to previous subsonic transient growth experiments, but, at the same time, is closely related to other recent and on-going efforts to measure roughness-induced transition at high-speed. In this section, the analysis and results are framed with respect to both low- and high-speed results. The section begins with a description of the experimental conditions and data processing, then presents the results of the current experiment in detail, with frequent reference to similarities to other low- and high-speed roughness studies. A framework for analyzing the disturbance energy evolution in high-speed experiments is included, adapting techniques used in low-speed transient growth experiments. The present work is then compared to a transient-growth-inspired roughness transition correlation, and, finally, the section ends with a survey of recent high-speed roughness-induced transition results to place the present work in their context.

4.1 Experimental conditions and data analysis

Steady and unsteady measurements were made for six conditions, representing a combination of three streamwise positions and three Reynolds number conditions, which are summarized in Table 4-1. The streamwise positions are X/L_s = 0.86, 0.90, and 0.94. These positions are, respectively, 278 mm, 295 mm, and 316 mm downstream of the

[*] Portions of this section are reprinted with permission from "Roughness-Induced Transient Growth on a Hypersonic Blunt Cone," by Sharp, N. S., and White, E. B., 2014. *AIAA Paper 2014-0432*, Copyright 2014 by the American Institute of Aeronautics and Astronautics, Inc.

	$X/L_s = 0.86$	$X/L_s = 0.90$	$X/L_s = 0.94$
$Re = 7.5 \times 10^6$ m^{-1}	X		
$Re = 8.7 \times 10^6$ m^{-1}	X	X	
$Re = 9.8 \times 10^6$ m^{-1}	X	X	X

Table 4-1. Experimental measurement stations by streamwise position and freestream unit Reynolds number. The X symbol marks measured conditions.

roughness array, as measured along a straight ray of the cone. All three measured Reynolds number conditions are well-inside the quiet flow regime of the M6QT (Hofferth 2013), and increased levels of freestream noise do not impinge onto the cone until $X/L_s = 0.71$ or later (see discussion in §3.1.4). Further details of each Reynolds number condition are given in Table 4-2.

Variation of the Reynolds number alters the boundary layer thickness at the roughness location, effectively changing the roughness height relative to the boundary layer. The lower Reynolds number cases correspond to smaller roughness heights relative to the boundary layer thickness. However, changing the Reynolds number also shifts the effective streamwise position of the measurements in terms of the number of boundary layer thicknesses over which they have developed. This complicates direct comparisons of different Reynolds numbers at the same axial streamwise location.

Parameter	Condition 1	Condition 2	Condition 3
Nominal M	5.9	5.9	5.9
Nominal P_0	689 kPa	793 kPa	896 kPa
Nominal T_0	430 K	430 K	430 K
Re	7.5×10^6 m^{-1}	8.7×10^6 m^{-1}	9.8×10^6 m^{-1}
Re_{edge}	8.8×10^6 m^{-1}	1.01×10^7 m^{-1}	1.14×10^7 m^{-1}
T_w/T_{aw}	0.95	0.95	0.95

Table 4-2. Details of the experimental conditions.

Using the scanning techniques and interpolation discussed in §3.4.2 produced total pressure results for fields approximately 100° in azimuthal span. These total pressure measurements were converted to Mach number using the Rayleigh-Pitot relations:

$$M^2 = \frac{2}{\gamma - 1}\left[\left(\frac{p_0}{p}\right)^{\frac{\gamma-1}{\gamma}} - 1\right], \quad for \quad M < 1 \tag{4.1}$$

$$\frac{p_0}{p} = \left[\frac{(\gamma+1)^2 M^2}{4\gamma M^2 - 2(\gamma+1)}\right]^{\frac{\gamma}{\gamma-1}}\left(\frac{1-\gamma+2\gamma M^2}{\gamma+1}\right), \quad for \quad M > 1 \tag{4.2}$$

where p_0 is the total pressure measured by the Pitot tube, p is the static pressure, and M is the local Mach number prior to the Pitot probe's interference. For supersonic Mach numbers, Equation 4.2 was solved numerically with a root-finding algorithm. The static pressure was assumed constant across the boundary layer and estimated using the measured average total pressure at the edge and the analytically-estimated edge Mach

number of 5.499. The static pressure's uncertainty was estimated using a ±0.5° misalignment of the cone, resulting in less than 2% uncertainty across all Reynolds numbers. The uncertainty in the total pressure measurement was based on the temperature-driven shift in the zero-offset value of the Kulite sensor's calibration (§3.2.1). These uncertainties in the pressures were carried through to the Mach number through the Rayleigh-Pitot relations. The uncertainty in the Mach number was approximately 3% or less for most regions of the flow. For clarity, the uncertainties are not displayed in the figures in §4.2-4.4, but they are given in the final disturbance energy estimates of §4.5.

In the present work, both the steady disturbances associated with transiently growing streaks and the unsteady disturbances caused by the roughness wake are of interest. Quantitative measures of the steady disturbance are obtained by decomposing the measured steady Mach number fields into two components: the azimuthally-invariant basic state $\overline{M}(x, y)$ and the azimuthally-varying steady disturbance. The azimuthally-invariant basic state is calculated as an azimuthal average of the measured steady flow and thus is not equivalent to a smooth-wall ideal basic state.

Although the M' disturbances are presented in terms of Mach numbers, it is important to note that these quantities are not, in themselves, Mach numbers but rather a measure of the relative effect of the steady disturbances on the Mach number. For example, an $M'(x, y, \phi) = -0.5$ represents a steady disturbance whose effect decreases the local Mach number by -0.5 relative to the basic state Mach number $\overline{M}$.

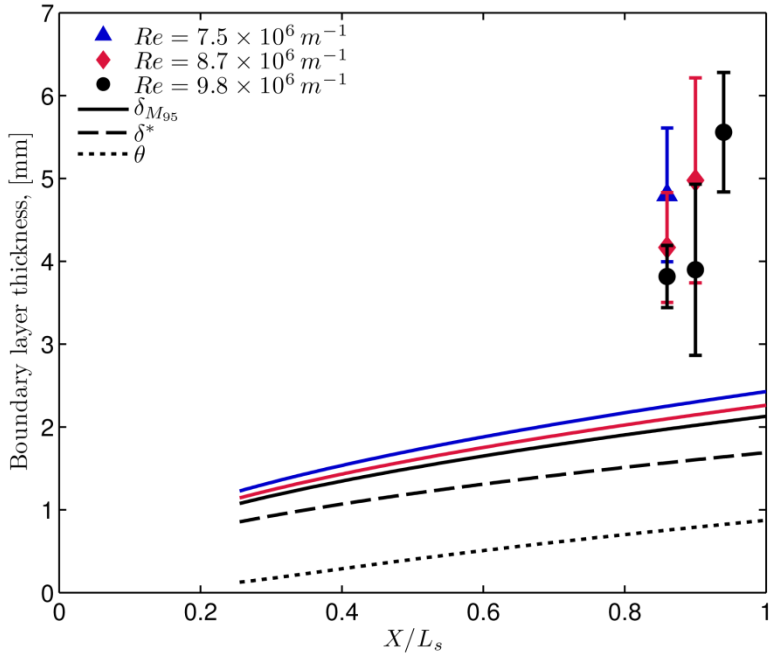

Figure 4-1. Streamwise evolution of boundary layer thickness. Experimental data points indicate average azimuthal boundary layer thickness based on 95% of edge Mach number with error bars indicating the root-mean-square of the azimuthal variation. Lines show predicted boundary layer thickness based on a self-similar compressible boundary layer on a sharp, 5° half-angle cone.

Because the unsteadiness in the total pressure measurements is large and it is unclear whether large unsteady variations in the static pressure may exist due to shock unsteadiness, the unsteady disturbances are presented in terms of the temporal root-mean-square of the total pressure measured by the Pitot probe, $p_{0,rms}$, normalized by the measured total pressure at the edge, $p_{0,edge}$.

The streamwise coordinate x is non-dimensionalized by the sharp cone length, L_s; the azimuthal coordinate ϕ by the roughness disturbance wavelength, λ_k; and the wall-normal coordinate y by the roughness element height, k.

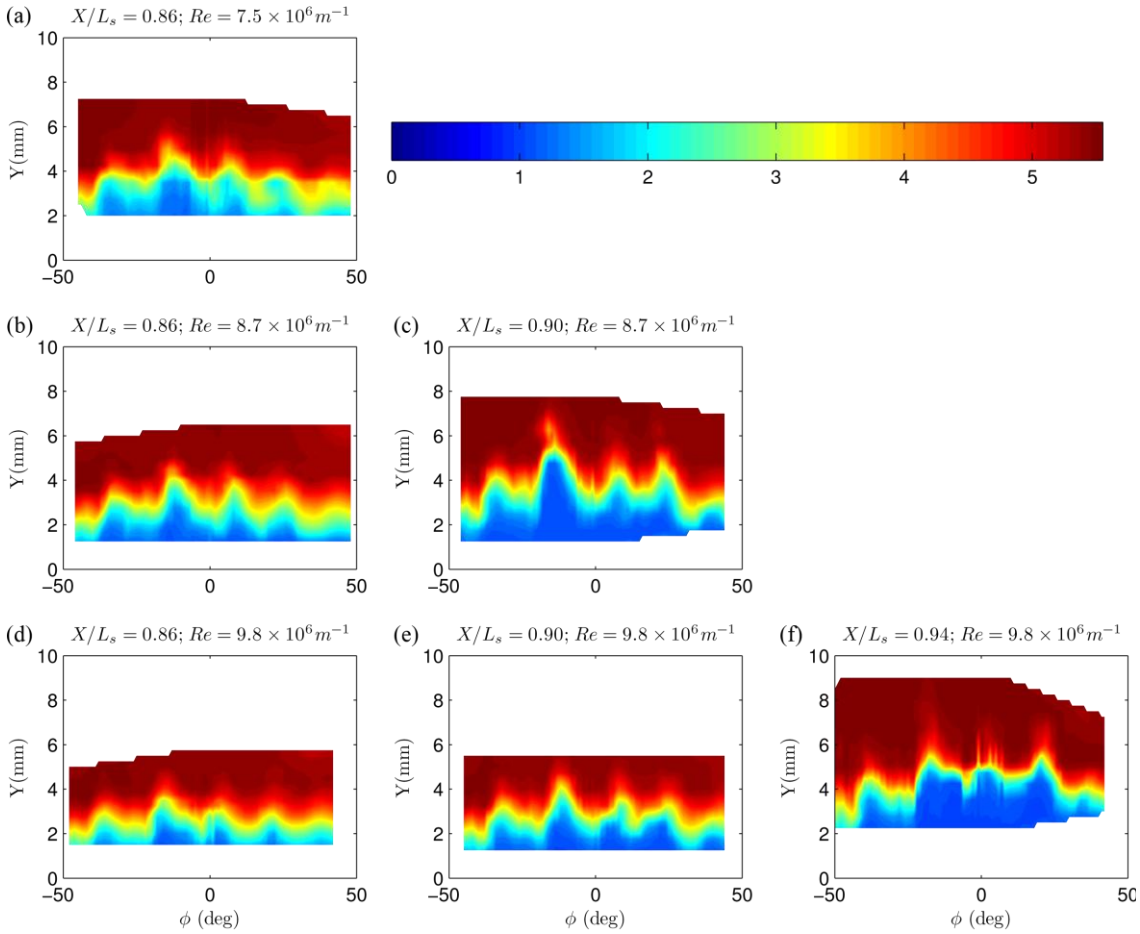

Figure 4-2. Contours of Mach number by streamwise location and Reynolds number.

4.2 Basic state measurements

The experimental basic state, $\overline{M}(x, y)$, is an azimuthal average of the experimental measurements taken at a specific height and streamwise position. Although data were taken over a larger azimuthal span, analysis was limited to four full disturbance wavelengths. Since the basic state is an average over an area including the roughness wakes, it cannot be considered equivalent to a smooth-wall ideal basic state.

The boundary layer thickness was estimated based on 95% of the edge Mach number. Figure 4-1 shows the streamwise evolution of the boundary layer thickness, with error bars indicating the root-mean-square variation in boundary layer thickness over the azimuthal span. Estimates of several boundary layer thickness measures for a self-similar compressible boundary layer on a 5° half-angle cone are also included for comparison. The solid line indicates an analytical boundary layer thickness based on 95% of the edge Mach number, whereas the dashed and dotted lines represent the displacement and momentum thicknesses, respectively, based on mass-flux. Both the boundary layer thickness and its growth rate are larger in the experiment than would be expected for a laminar boundary layer. The aftmost streamwise position of the high Reynolds number case shows particularly strong growth that could be a precursor to transition.

The raw Mach number contours for the full azimuthal span are shown in Figure 4-2. The contours consist of azimuthally-alternating high- and low-speed streaks, as expected for roughness-induced transient growth. There is significant element-to-element variation in the streak heights, as reflected in the error bars in Figure 4-1; however, each condition is consistent in the pattern of variation between streaks, indicating that these variations may be the result of imperfections and inconsistencies between individual roughness elements. As the streaks develop in the streamwise direction, the boundary layer's distortion increases and individual streaks begin to warp, as in Figure 4-2(f).

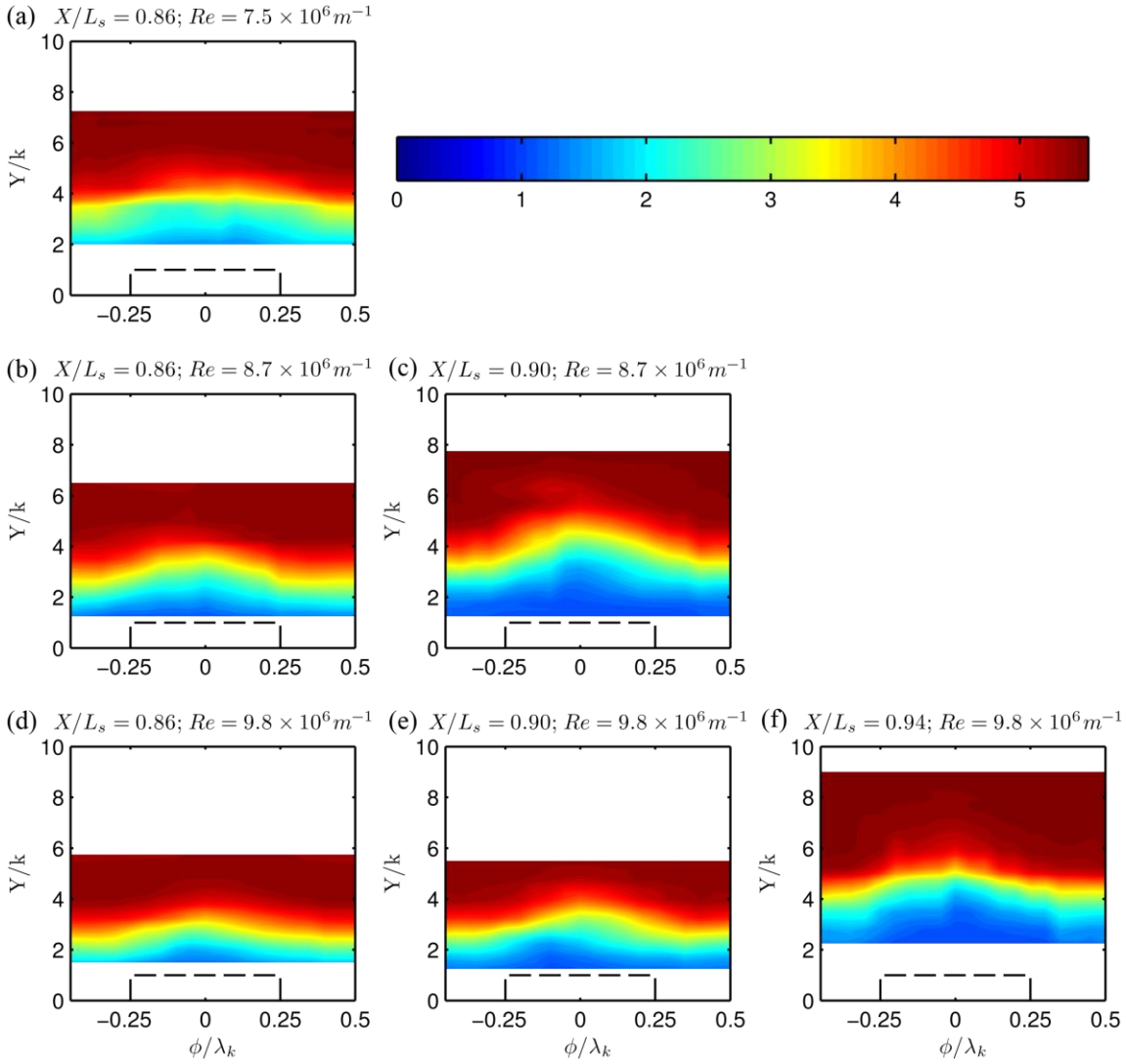

Figure 4-3. Phase-locked averaged contours of Mach number by streamwise location and Reynolds number. Dashed lines indicate the projection of a roughness element into the measurement plane.

To decrease the effects of element-to-element variation, the data were phase-locked averaged over four disturbance wavelengths, λ_k. Phase-locked averaged Mach number contours are shown in Figure 4-3. Dashed lines mark the projection of a roughness element into the plane of measurement. The low-speed streak is centered behind the roughness, as observed in prior work at both subsonic (White *et al.* 2005,

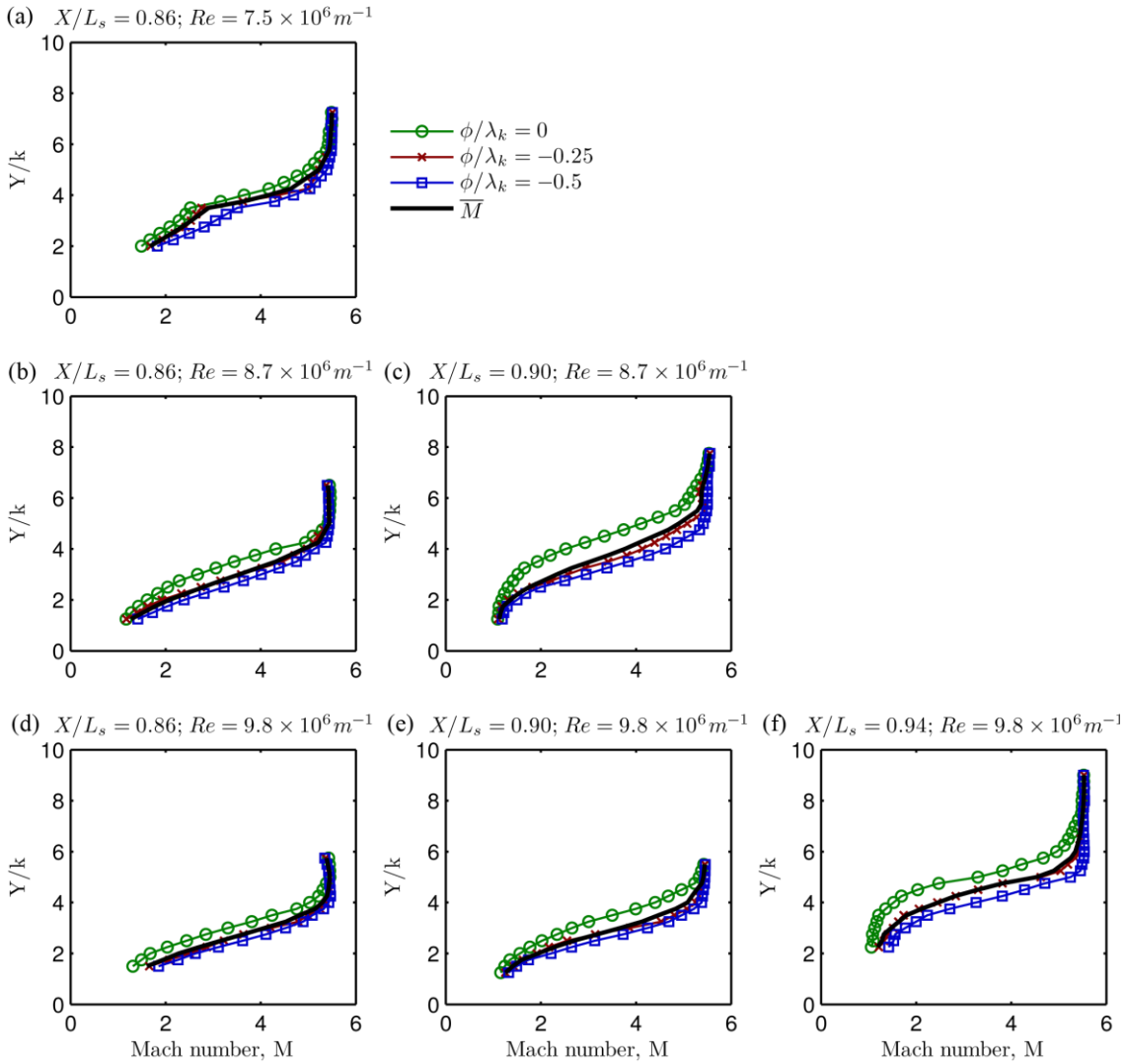

Figure 4-4. Wall-normal Mach number profiles by streamwise location and Reynolds number. Phase-locked averaged profiles are shown along the roughness element centerline $(\phi / \lambda_k = 0)$, at the roughness element edge $(\phi / \lambda_k = -0.25)$, and between the roughness elements $(\phi / \lambda_k = -0.5)$. The solid black line indicates the azimuthal average Mach number profile.

Ergin and White 2006) and supersonic speeds (Bathel *et al.* 2010, Choudhari *et al.* 2010, Kegerise *et al.* 2010, Iyer and Mahesh 2013). A high-speed streak sits between roughness elements. As the streaks grow, the boundary layer is increasingly distorted,

with the contours beginning to show possible signs of breakdown, especially near the top of the low-speed streak in Figure 4-3(c) and (f).

Figure 4-4 shows Mach number profiles in azimuthal slices at the roughness centerline, the roughness element edge, and between roughness elements. The solid black line indicates the azimuthally-invariant basic state. Along the centerline, the Mach number remains low in a region extending several roughness heights from the wall, followed by a region of high-shear stretching to the boundary layer edge. The profiles strongly resemble those seen by Kegerise *et al.* (2010) in the mid-wake region behind a diamond-shaped roughness element at Mach 3.5, including the kink near $Y/k = 3.5$ in Figure 4-4(a). At the edge of the roughness element, the profiles nearly match those of the azimuthal basic state. Between the roughness elements, the edge Mach number extends to lower heights, consistent with a high-speed streak, but the profiles show stronger resemblance to the basic state profile than the centerline profiles do. This suggests that the high-speed streaks do not cause as much distortion in the boundary layer as the low-speed streaks. Overall, none of the Mach number profiles demonstrate the fullness expected from transition into a turbulent boundary layer. There are signs of inflection in the basic state profiles in Figure 4-4(c), (e), and (f), but these occur near the sonic line below $Y/k = 2$ and are suspected remnants of the spatial averaging caused by the size of the Pitot probe.

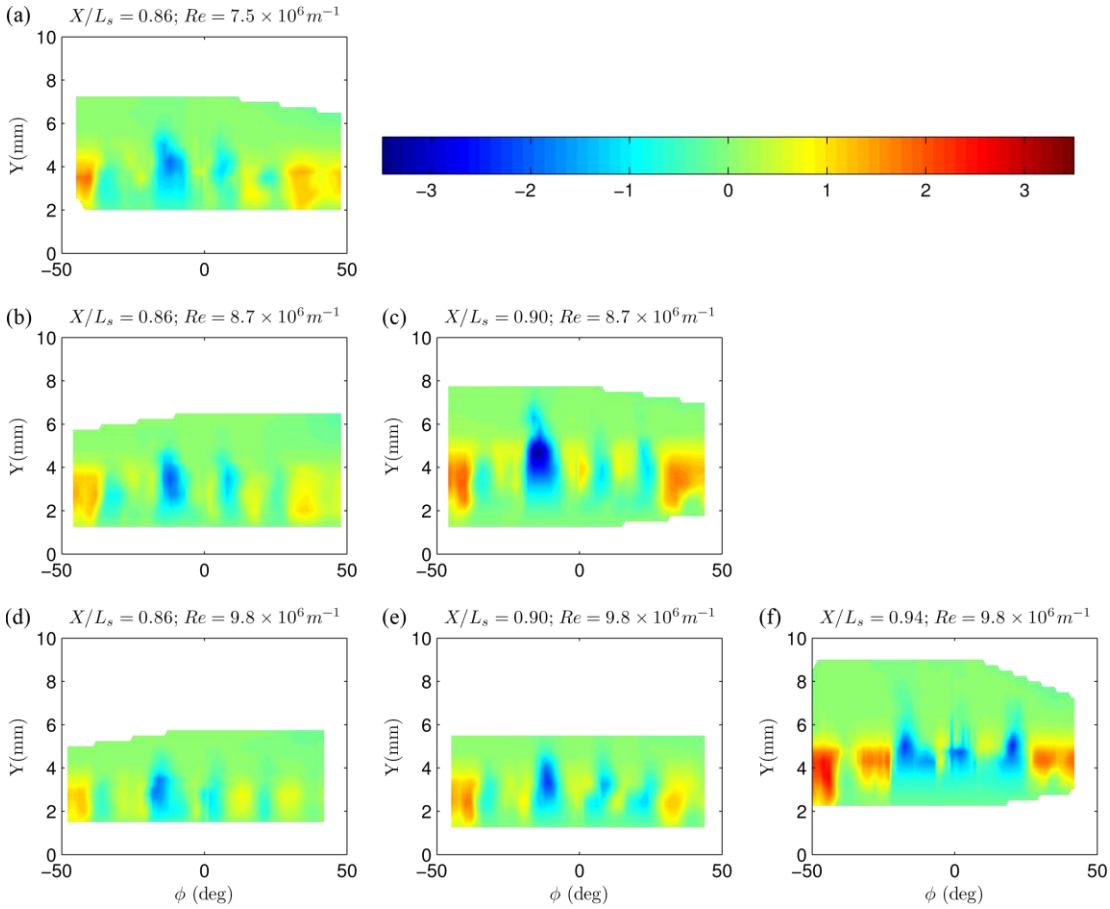

Figure 4-5. Contours of steady disturbance M' by streamwise location and Reynolds number.

4.3 Steady disturbance measurements

The azimuthally-varying steady disturbance $M'(x, y, \phi)$ is obtained by subtracting the basic state $\overline{M}$ from every azimuthal position. The raw steady disturbance contours are shown in Figure 4-5. Like the Mach number contours (Figure 4-2), the raw steady disturbances show alternating high- and low-momentum streaks that vary significantly from element to element.

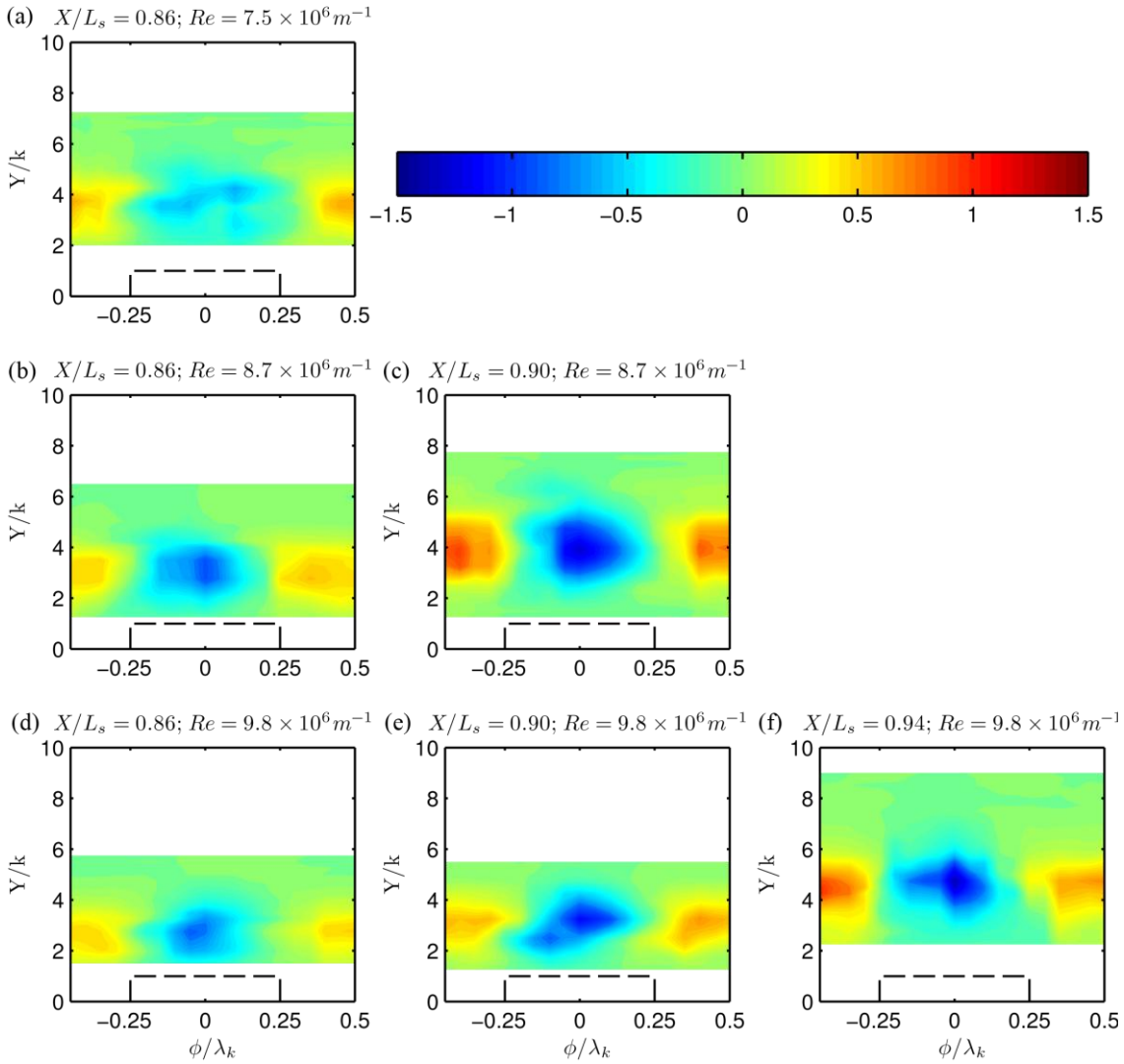

Figure 4-6. Phase-locked averaged contours of steady disturbance M' by streamwise location and Reynolds number. Dashed lines indicate the projection of a roughness element into the measurement plane.

The phase-locked averaged steady disturbance contours are given in Figure 4-6. The low-speed streaks appear generally stronger than their high-speed counterparts, but both disturbances intensify with increasing streamwise distance for the Reynolds numbers observed. Figure 4-7 shows profiles of the steady disturbance along the

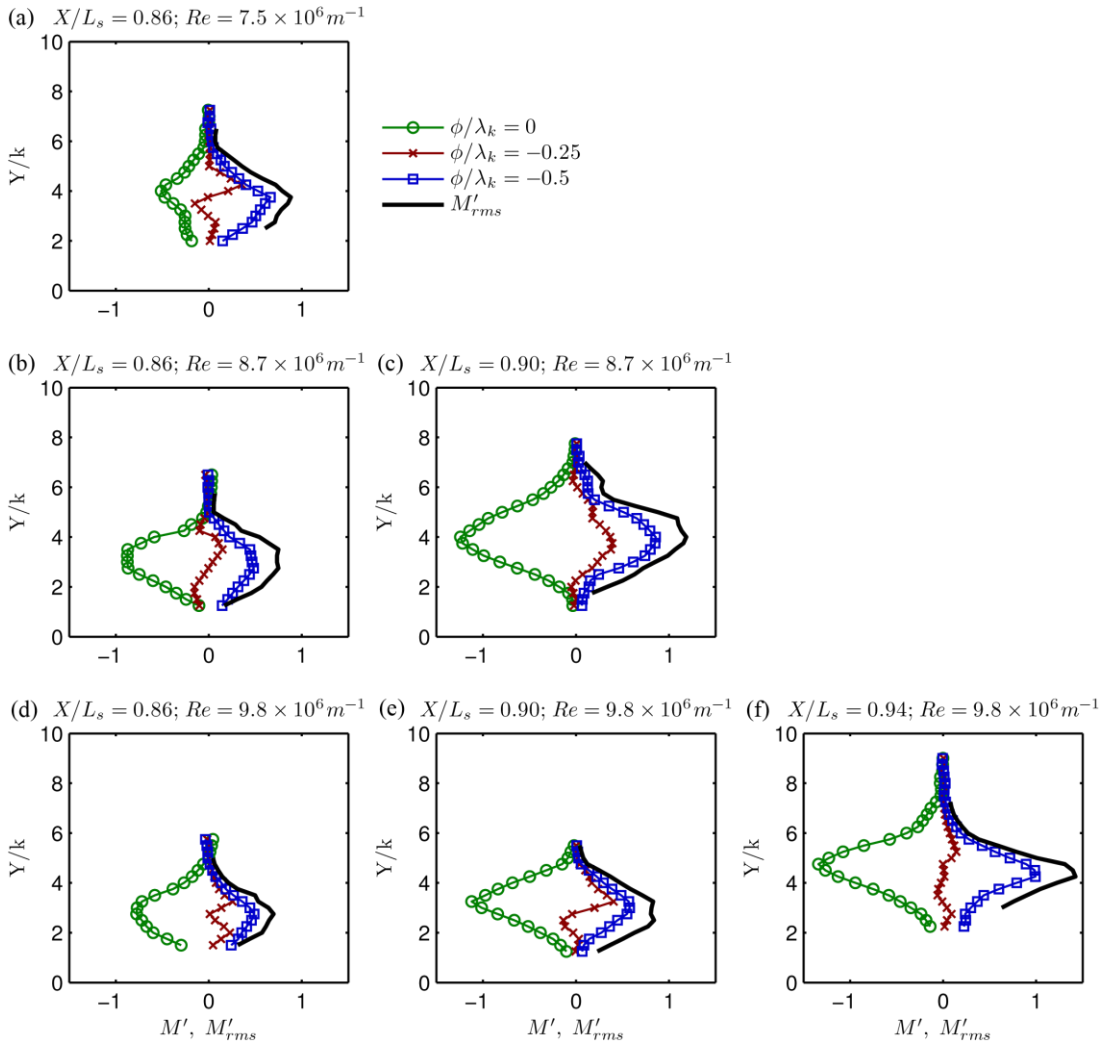

Figure 4-7. Wall-normal steady disturbance M' profiles by streamwise location and Reynolds number. Phase-locked averaged profiles are shown along the roughness element centerline $(\phi / \lambda_k = 0)$, at the roughness element edge $(\phi / \lambda_k = -0.25)$, and between the roughness elements $(\phi / \lambda_k = -0.5)$. The solid black line indicates the full-span azimuthal root-mean-square steady disturbance profile.

roughness element centerline, the roughness edge, and between roughness elements. The solid black line represents the azimuthal root-mean-square variation, M'_{rms}, measured across four disturbances wavelengths. In all but Figure 4-7(a), the low-speed streak on

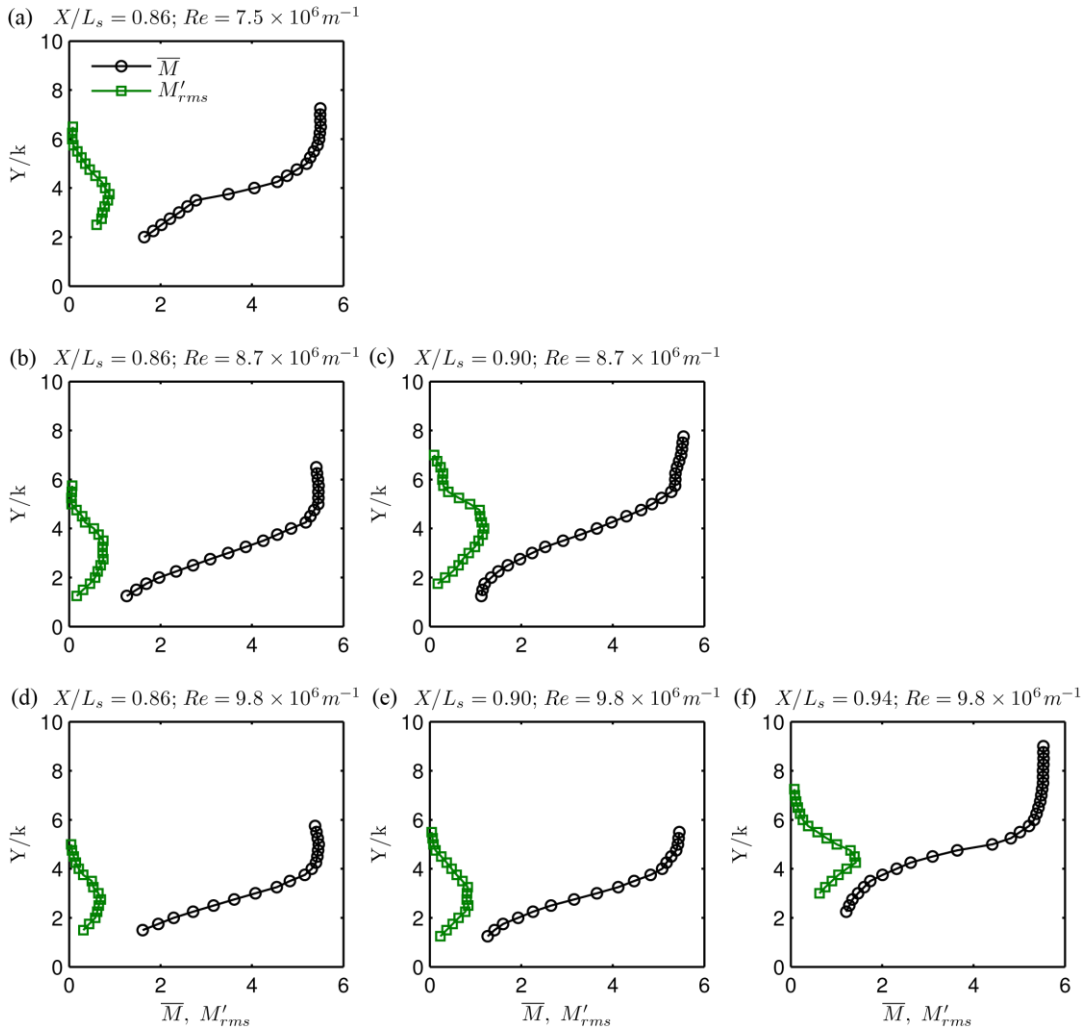

Figure 4-8. Wall-normal profiles of $\overline{M}$ and M'_{rms} by streamwise location and Reynolds number.

the roughness centerline has a larger peak magnitude than the high-speed streak between roughness elements. Both the low- and high-speed streaks show consistent streamwise growth. Along the roughness edge, the steady disturbance is at its weakest, and these profiles show effects of both the low- and high-speed streaks.

Figure 4-8 compares the basic state $\overline{M}$ with the full-span azimuthal rms steady disturbance M'_{rms}. The steady disturbance reaches its peak magnitude toward the lower end of the boundary layer's high-shear region, and there are no clear signs of the disturbance's peak magnitude shifting relative to the boundary layer's growth. The magnitude of the steady disturbance is very large relative to the basic state, and peaks at between 12-26% of the edge Mach number or 15-30% of the total Pitot pressure at the edge.

4.4 Unsteady disturbance measurements

The unsteady disturbance has been characterized using the temporal root-mean-square of the total Pitot pressure at each spatial location. An azimuthal average of these values over four disturbance wavelengths gives a measure of the total unsteadiness.

Raw contours of the unsteady total Pitot pressure are given in Figure 4-9. The regions of unsteadiness closely follow the boundary layer seen in Figure 4-2 and show much of the same element-to-element variation. Phase-locked averaged contours are visible in Figure 4-10. The region of strongest unsteadiness is located near the low-speed streak in the shear-layer generated above the roughness element, consistent with the strong shear-layer unsteadiness observed by Iyer and Mahesh (2013) behind hemispherical roughness. The unsteadiness is strongest and most widespread at the forwardmost station and highest Reynolds number case in Figure 4-10(d), which corresponds to the largest effective k/δ. For all Reynolds number cases, the unsteadiness decays with increasing streamwise distance.

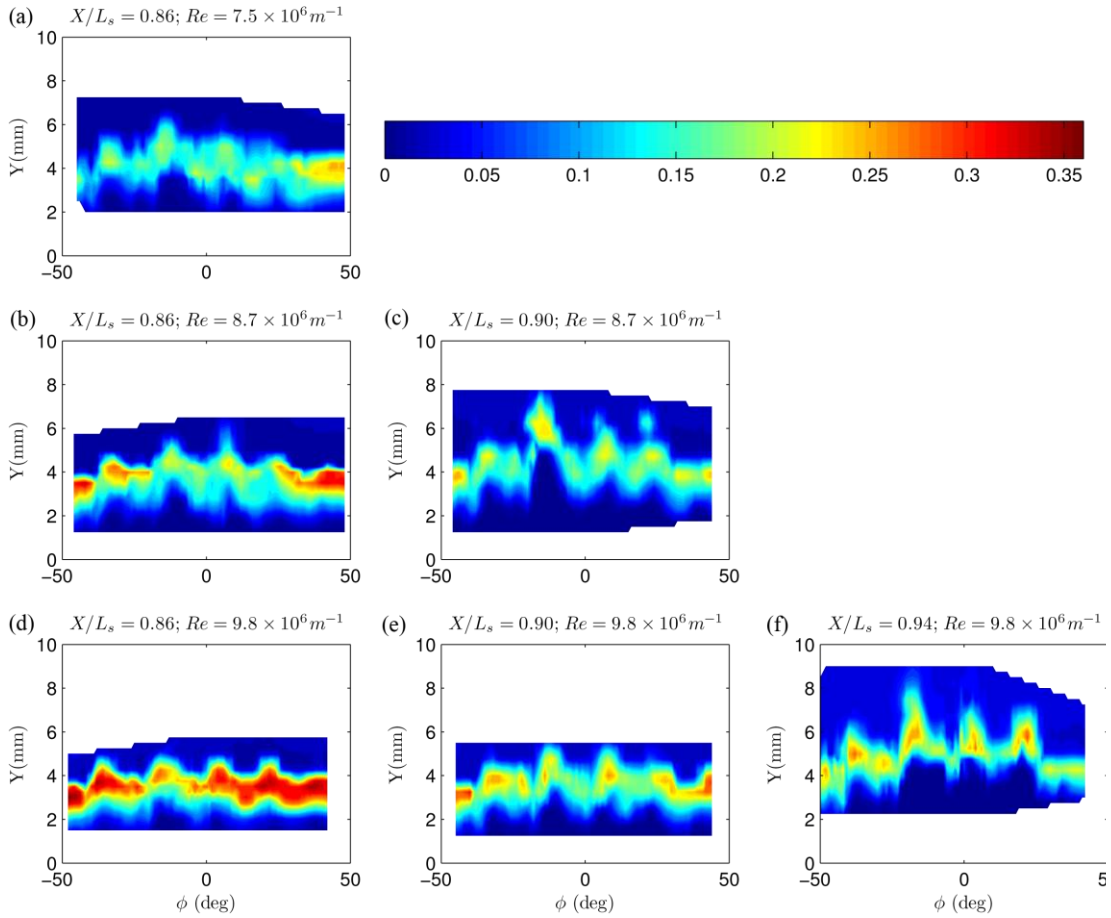

Figure 4-9. Contours of unsteady total pressure $p_{0,rms} / p_{0,edge}$ by streamwise location and Reynolds number.

Figure 4-11 shows profiles of the unsteady total Pitot pressure along the roughness centerline, roughness edge, and between roughness elements. The unsteady disturbance profiles are very similar at all azimuthal positions, with a general trend of decaying peak magnitude with downstream distance. However, the downstream positions at higher Reynolds numbers show signs of the centerline unsteadiness profile lifting and broadening compared to the other azimuthal positions. Kegerise *et al.* (2010) observed a similar broadening of the fluctuating mass-flux profiles on the centerline of a

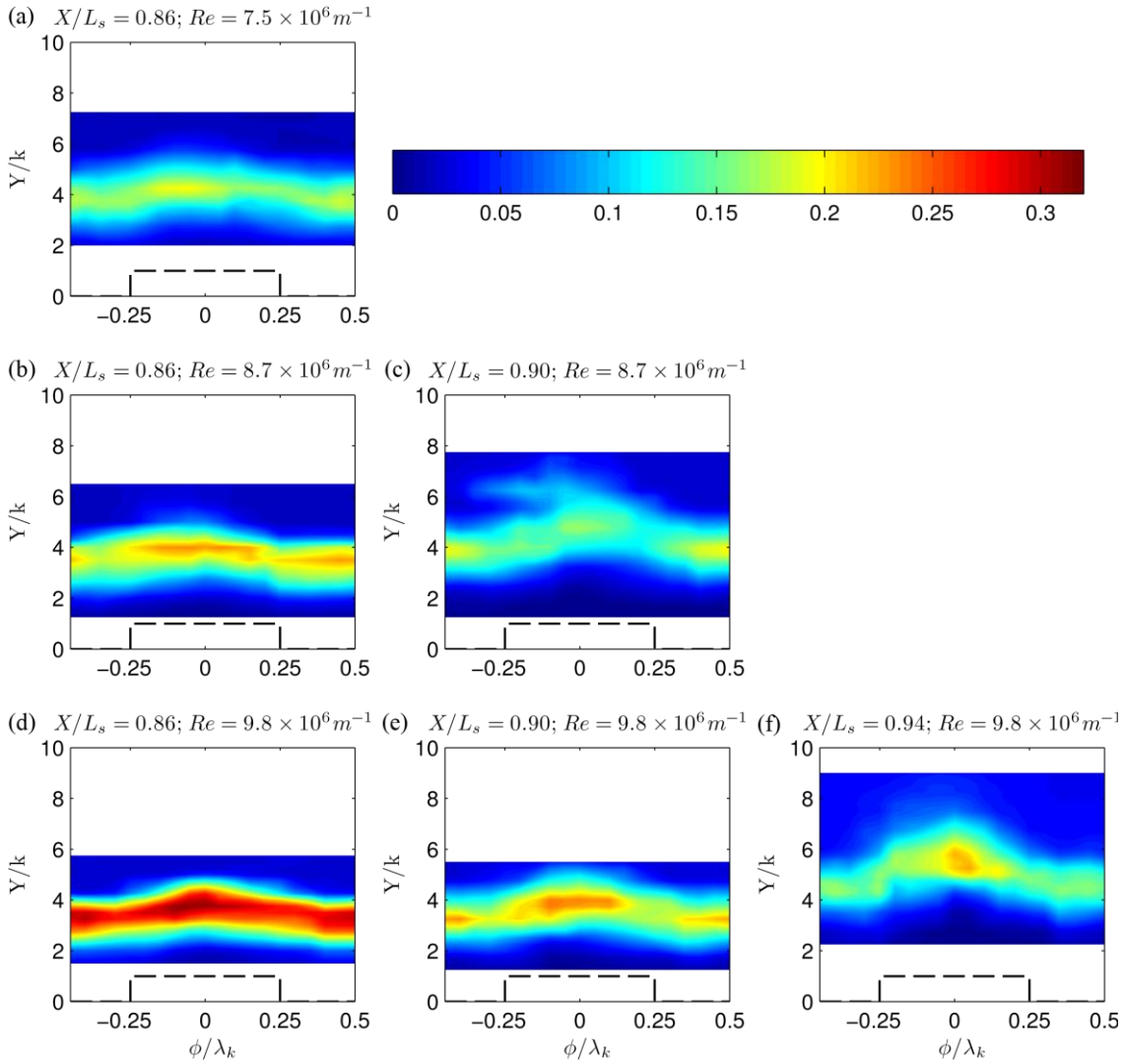

Figure 4-10. Phase-locked averaged contours of unsteady total pressure $p_{0,rms} / p_{0,edge}$ by streamwise location and Reynolds number. Dashed lines indicate the projection of a roughness element into the measurement plane.

diamond roughness element in the mid-wake region prior to transition. The present cone model is too short to observe transition at these conditions.

Figure 4-12 shows the azimuthal average unsteady total Pitot pressure profiles compared to the basic state $\overline{M}$. The unsteadiness peaks in the high-shear region of the

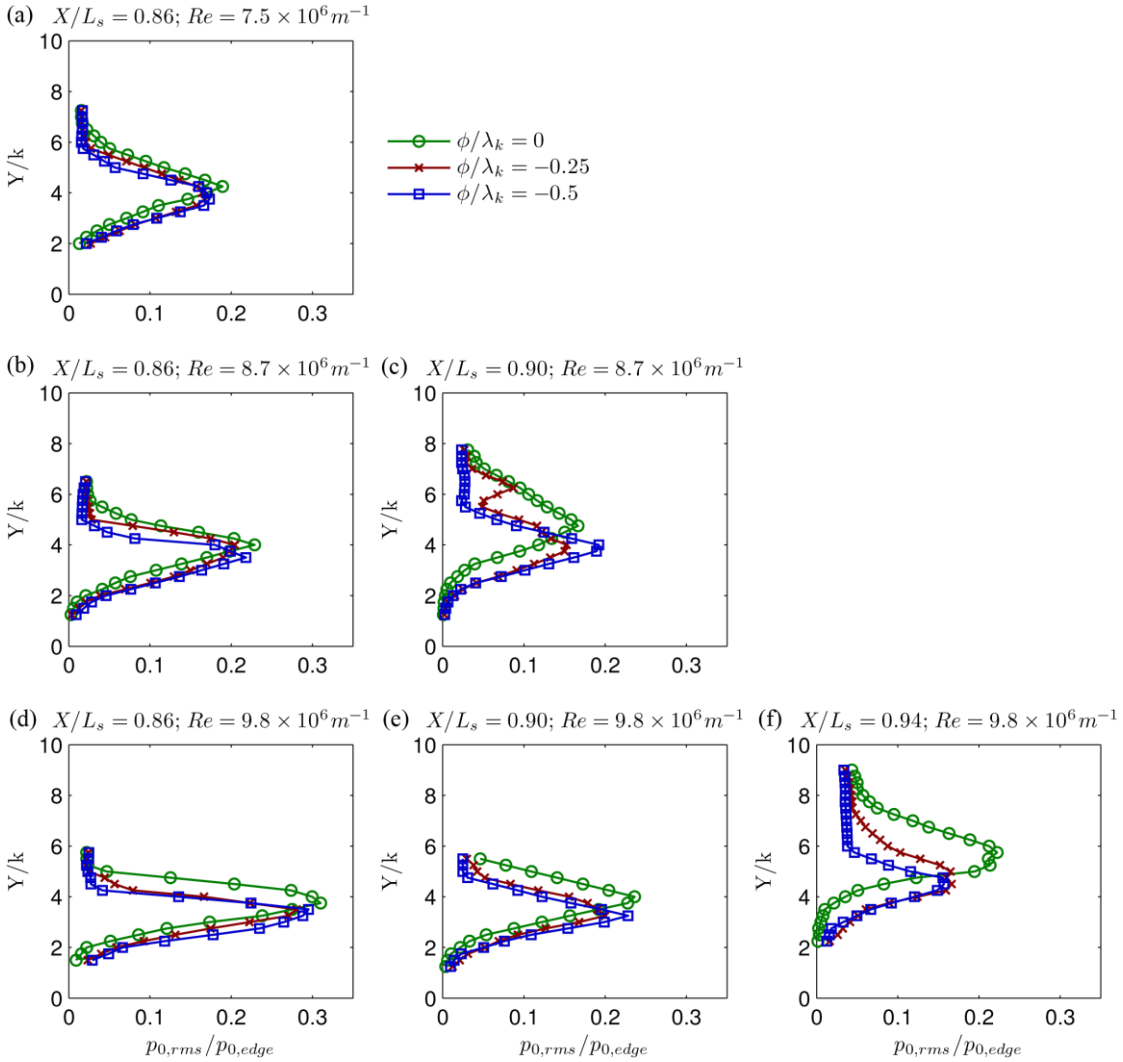

Figure 4-11. Wall-normal unsteady total pressure $p_{0,rms} / p_{0,edge}$ profiles by streamwise location and Reynolds number. Phase-locked averaged profiles are shown along the roughness element centerline $(\phi / \lambda_k = 0)$, at the roughness element edge $\phi / \lambda_k = -0.25$, and between the roughness elements $\phi / \lambda_k = -0.5$.

basic state and its magnitude is quite large. The peak unsteady fluctuations are between 15-28% of the total edge pressure.

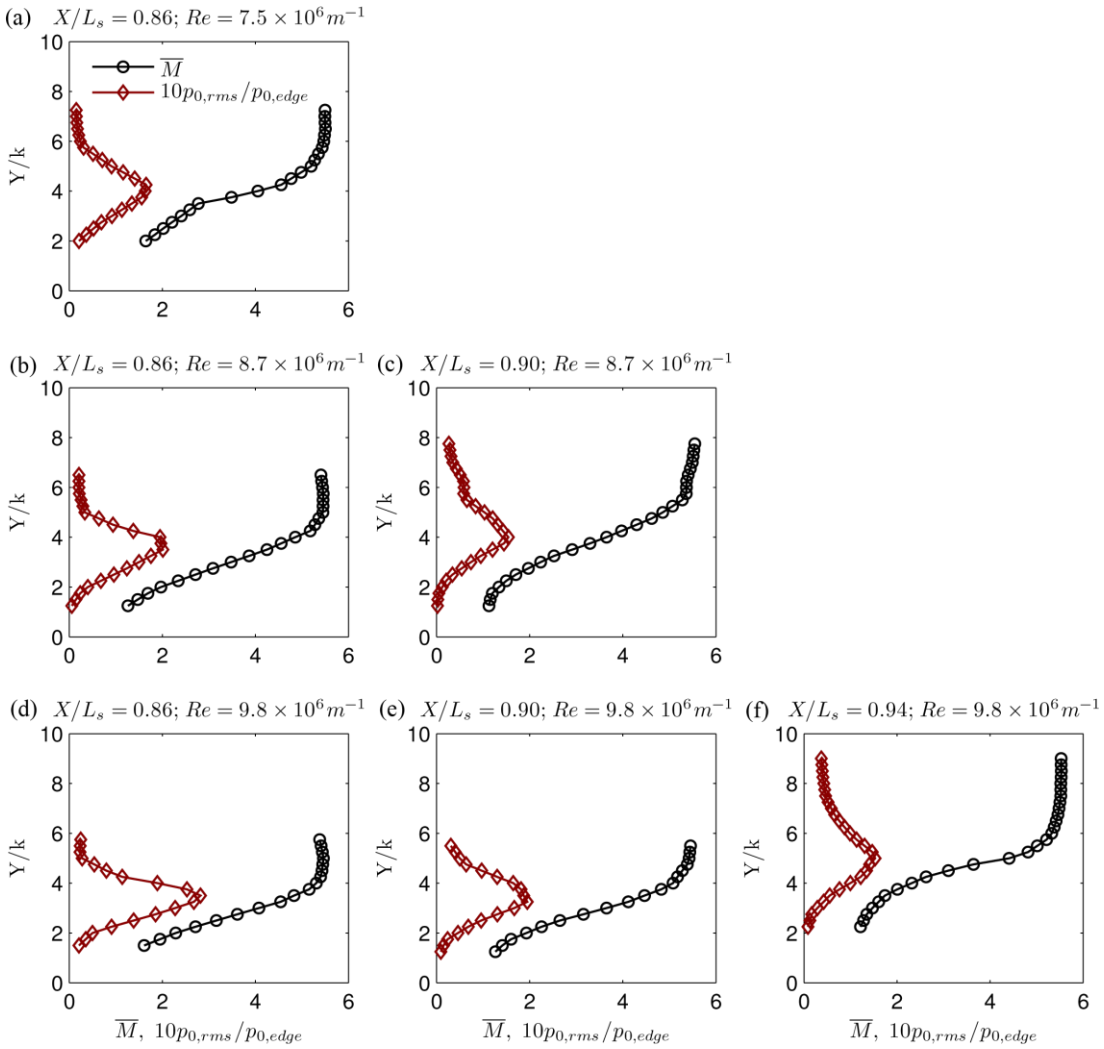

Figure 4-12. Wall-normal profiles of $\overline{M}$ and $p_{0,rms} / p_{0,edge}$ by streamwise location and Reynolds number.

The largest deviations in Mach number, steady disturbance, and unsteadiness are consistently observed along the roughness centerline; these quantities are shown together in Figure 4-13. Along the roughness centerline, the Mach number profiles have an inflection point near Mach 3, coinciding with the peak of the low-speed streak. The peak

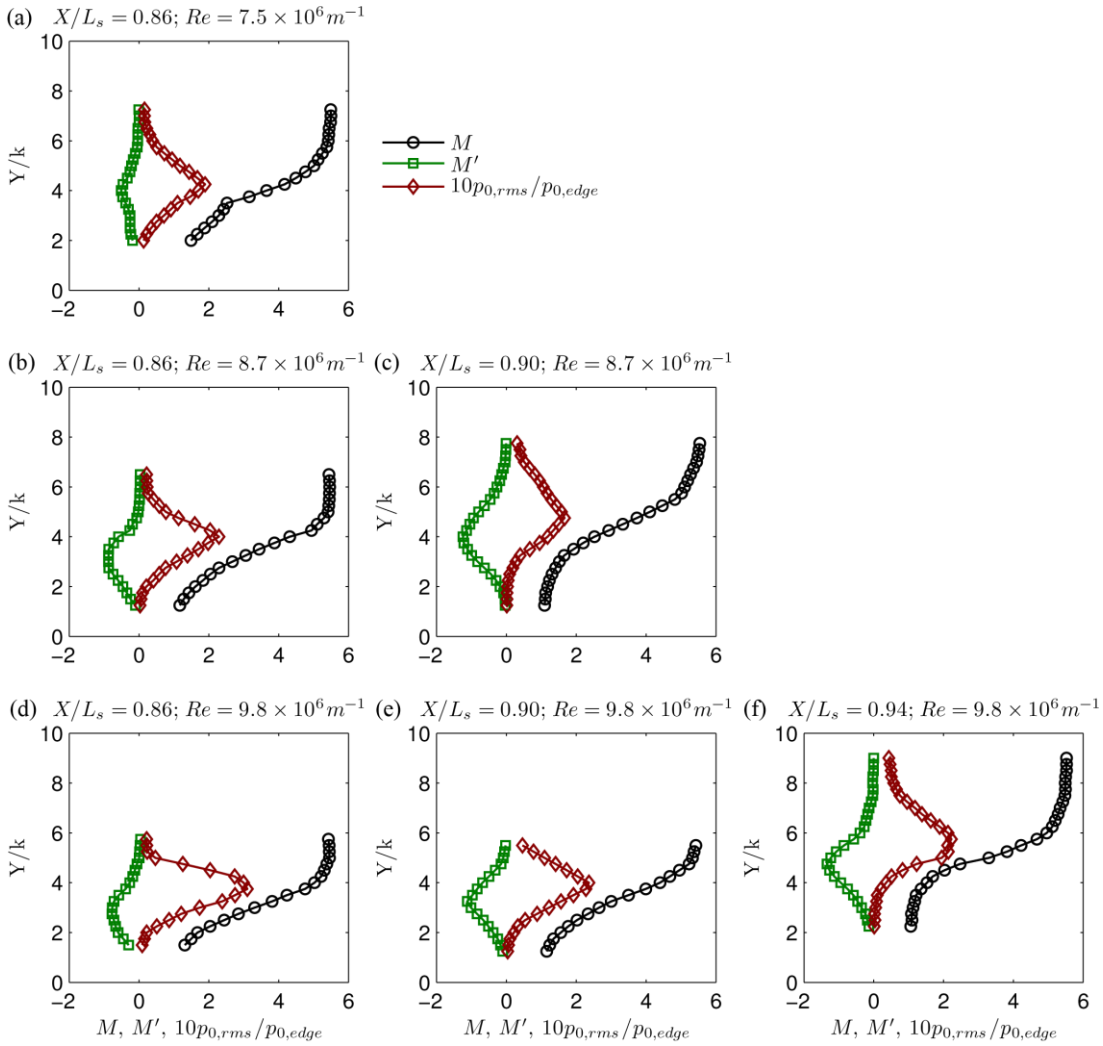

Figure 4-13. Wall-normal profiles of M , M', and $p_{0,rms} / p_{0,edge}$ along the centerline of a roughness element by streamwise location and Reynolds number.

unsteadiness is observed just above this inflection point, as would be expected for unsteadiness caused by the shear-layer.

4.5 Disturbance energy evolution

Evaluating transient growth in a flow requires a specific quantity that measures the disturbance and its evolution. In the incompressible framework, the quantity of choice is the kinetic energy of the disturbance. Using a velocity disturbance vector-function $\boldsymbol{q} = (\hat{u}, \hat{v}, \hat{w})^T$, the scalar energy norm based on kinetic energy density is:

$$\left\| \boldsymbol{q}^2 \right\| = \int_0^\infty \left(\hat{u}^2 + \hat{v}^2 + \hat{w}^2 \right) dy \tag{4.3}$$

Because the wall-normal and spanwise disturbance velocities are small and not easily measurable, experimentalists have approximated the disturbance energy using only the streamwise term (White 2002, White *et al.* 2005).

For a compressible flow, the choice of energy norm is complicated by the necessity of including temperature effects. Previous compressible optimal disturbance calculations have used the Mack energy norm (Hanifi *et al.* 1996, Tumin and Reshotko 2001, Zuccher *et al.* 2006). The disturbance vector-function is now $\boldsymbol{q} = \left(\hat{u}, \hat{v}, \hat{w}, \hat{\rho}, \hat{T} \right)^T$, and the scalar product is defined as:

$$\left(\boldsymbol{q}_1, \boldsymbol{q}_2 \right)_2 = \int_0^\infty \boldsymbol{q}_1^H \boldsymbol{M} \boldsymbol{q}_2 \, dy \tag{4.4}$$

where *H* indicates the complex conjugate transpose and the matrix $\boldsymbol{M}$ is:

$$\boldsymbol{M} = diag \left[\rho, \rho, \rho, \frac{T}{\gamma \rho M_e^2}, \frac{\rho}{\gamma(\gamma - 1) T M_e^2} \right] \tag{4.5}$$

Note that ρ and T are mean quantities, *not* disturbances. Both the mean and disturbance quantities are made non-dimensional by edge values. As Hanifi *et al.* (1996) note in their

derivation, there is no obvious or natural choice for the scalar product in the compressible form. Instead, Equations 4.4 and 4.5 represents an energy-density-like quantity defined in such a way that the pressure-related energy transfer terms (also called compression work) are eliminated. The corresponding energy norm, originally introduced by Mack (1969) is:

$$\left\| \boldsymbol{q}^{2} \right\| = \int_{0}^{\infty} \left\{ \rho \left(\hat{u}^{2} + \hat{v}^{2} + \hat{w}^{2} \right) + \frac{1}{\gamma M_{e}^{2}} \left[\frac{\hat{\rho}^{2} T}{\rho} + \frac{\rho \hat{T}^{2}}{(\gamma - 1) T} \right] \right\} dy \tag{4.6}$$

The right hand side (RHS) of Equation 4.6 contains the incompressible energy norm, as well as terms dependent on the density and temperature disturbances. There is no pressure variation across the boundary layer, so the density disturbance is directly connected to the temperature disturbance through the equation of state, and both the fourth and fifth terms of Equation 4.6 can be considered as temperature-dependent. To evaluate the relative importance of each disturbance component to the energy norm, it is helpful to consider an example.

Without a DNS, the obvious example to consider is an optimal disturbance calculation since every necessary basic state and disturbance quantity is included. Each term in Equation 4.6 was evaluated using an optimal disturbance calculation (see §2.2 for details) for a sharp, 5° half-angle cone at a Mach number and Reynolds number condition equal to the highest Reynolds number experimental case. As in the incompressible case, the streamwise velocity disturbance accounts for most of the velocity-related disturbance energy – two orders of magnitude more energy than the wall-normal or spanwise disturbances. This is consistent with Zuccher *et al.* (2006),

which found no significant effect on the outlet energy norm from the *v*- and *w*-components in supersonic flat-plate boundary layers at Reynolds numbers higher than 10^4. However, the temperature and density fluctuations account for 97% of the overall energy in the Mack energy norm, with the *u*-component representing about 2.8% of the overall energy.

This strong effect of temperature in the Mack energy norm is unsurprising. Both the *u*-disturbance and *T*-disturbance result from the lift-up effect shifting fluid across the boundary layer, which carries both momentum and heat. Numerous studies of high-speed roughness-induced transition have noted the presence of high-temperature streaks coinciding with the high-speed streaks on either side of a roughness element (Borg and Schneider 2008, Casper *et al.* 2011, Choudhari *et al.* 2010, Bathel *et al.* 2010). Iyer and Mahesh (2013) noted that these high-temperature streaks persisted for long distances downstream of the roughness even when transition was not observed.

None of the presently available diagnostics for the M6QT facility are suitable for measuring azimuthally-varying temperature disturbances in the boundary layer. Pitot pressure measurements are more closely related to velocity than temperature. Smits *et al.* (1983) found that constant temperature hot-wire anemometry was unsuitable for measuring temperature fluctuations due to the instrument's highly non-linear response to these changes. Optical diagnostics such as planar laser-induced fluorescence (Laufer *et al.* 1990) might be best suited to measuring these temperature disturbances, but such experiments would require a facility with greater optical access than the M6QT.

The remainder of the present analysis focuses only on the velocity-dependent terms of the Mack energy norm. As noted above, both the streamwise-velocity and temperature-disturbances are the result of the lift-up effect, and transient growth should be identifiable in either. However, for purposes of comparing the experimental work to compressible optimal disturbance calculations or future simulations, it is important to note that temperature-dependent terms of the Mack energy norm are being ignored.

Among the velocity-dependent disturbance terms in Equation 4.6, the *u*-component accounts for more than 98% of the disturbance energy. Thus, we neglect the wall-normal and spanwise components, giving:

$$\left\| \boldsymbol{q}^2 \right\| \approx \int_0^\infty \rho \hat{u}^2 dy \tag{4.7}$$

Knowing that $U >> V, W$ and $\hat{u} >> \hat{v}, \hat{w}$, we can re-express Equation 4.7 in terms of the Mach number:

$$\left\| \boldsymbol{q}^2 \right\| \approx \int_0^\infty \rho \left(M - \overline{M} \right)^2 a^2 dy \tag{4.8}$$

where *M* is the experimentally-measured Mach number, $\overline{M}$ is the mean Mach number, and *a* is the speed of sound based on mean flow quantities. By inserting the speed of sound and applying the perfect gas law, Equation 4.8 can be rewritten in terms of Mach numbers and mean static pressure:

$$\left\| \boldsymbol{q}^2 \right\| \approx \int_0^\infty \gamma p \left(M - \overline{M} \right)^2 dy \tag{4.9}$$

Equation 4.9 is an experimentally tractable approximation to the velocity-dependent terms of the Mack energy norm. The Mach numbers can be calculated from the total pressures measured with a Pitot tube, and the static pressure can be calculated analytically or estimated from measurements or simulations.

The total disturbance energy due to the steady disturbances is quantified by:

$$E_{rms}(x) = \int_{y=0}^{\infty} \gamma p M'_{rms}(x, y)^2 \, dy \tag{4.10}$$

where $M'_{rms}(x, y)$ is the azimuthal rms of the steady disturbance M' along an azimuthal line at a given height and streamwise location. The wall-normal coordinate is scaled by the roughness height *k*, and the static pressure *p* is scaled by the analytical $\rho_e U_e^2$ at the boundary layer edge. A proxy for the unsteady disturbance energy is defined using the temporal rms of the total Pitot pressure:

$$e_{rms}(x) = \int_{y=0}^{\infty} \int_{\phi=-\frac{1}{2}}^{\frac{1}{2}} p_{0,rms}(x, y, \phi) dy d\phi \tag{4.11}$$

where $p_{0,rms}$ is made non-dimensional by the total Pitot pressure at the edge, and the azimuthal coordinate ϕ is made non-dimensional by the disturbance wavelength, λ_k.

Since the disturbance is periodic in the azimuthal direction, the phase-locked averaged steady disturbance quantity data (i.e. $\sqrt{\gamma p} M'$) is additionally decomposed by wavelength using a discrete Fourier transform in the azimuthal direction for a given height and streamwise position. A power spectral density (PSD) is then defined as:

$$PSD = \left(\frac{2\left|H_n\right|^2 \lambda_k}{N^2} \right)^{1/2} \tag{4.12}$$

where H_n are the complex discrete Fourier coefficients and N is the number of spatially sampled points ($N = 20$). The PSD is normalized such that, at every height, Parseval's theorem is written as:

$$\sqrt{2}\gamma p M'^{2}_{rms} = \int_0^{1/2\Delta\phi} PSD\left(\lambda^{1/2}\right) d\left(\lambda^{-1/2}\right) \tag{4.13}$$

where, in this case, M'_{rms} is evaluated on the phase-locked averaged data. The upper bound in Equation 4.13 is the spatial Nyquist limit. The disturbance energy contained within a particular azimuthal wavelength is then quantified by integrating the appropriate component of the power spectrum across the boundary layer to obtain $E_\lambda(x)$, where λ is the azimuthal wavelength of interest.

Figure 4-14 shows profiles of the steady and unsteady disturbance quantities prior to integration. As observed in §4.3 and §4.4, the steady disturbance experiences sharp growth in the streamwise direction, whereas the unsteady disturbance decays in peak magnitude downstream. Note that error bars marking the uncertainty are included, but their extent is roughly the same size as the markers. Figure 4-15 breaks down the steady disturbance by wavelength, according to Equations 4.12 and 4.13. The energy in the fundamental wavelength, λ_k, clearly dominates, but energy is also present in the harmonics.

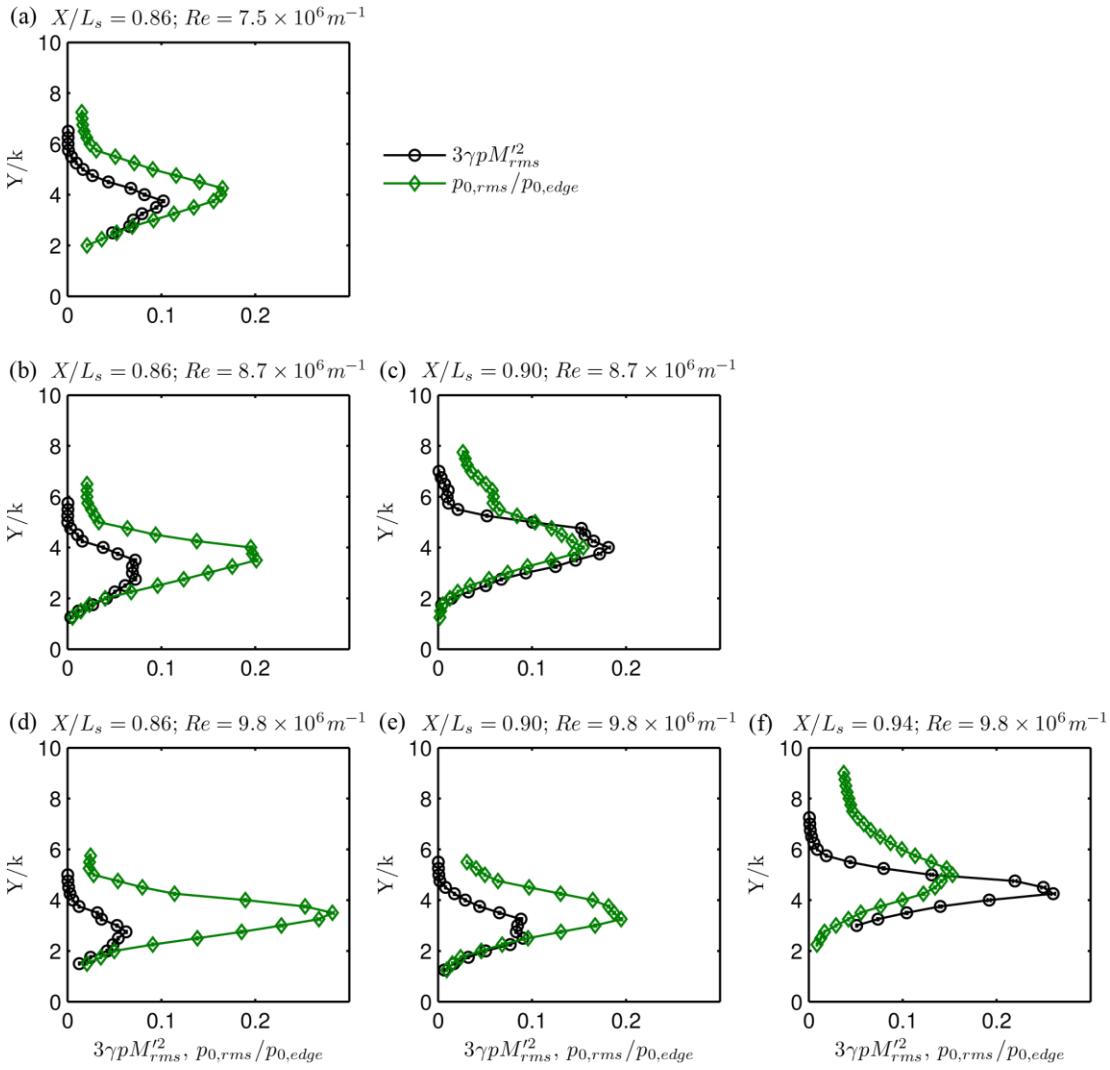

Figure 4-14. Steady disturbance and unsteady total Pitot pressure profiles $\gamma p M_{rms}'^2$ and $p_{0,rms} / p_{0,edge}$ by streamwise location and Reynolds number.

The profiles in Figures 4-14 and 4-15 were integrated numerically using the trapezoid rule. Note that some of these profile are incomplete near the lower boundary. In integrating the profiles the disturbance energy contribution from these lower regions was approximated. First, a linear curve fit to the final three points was used to

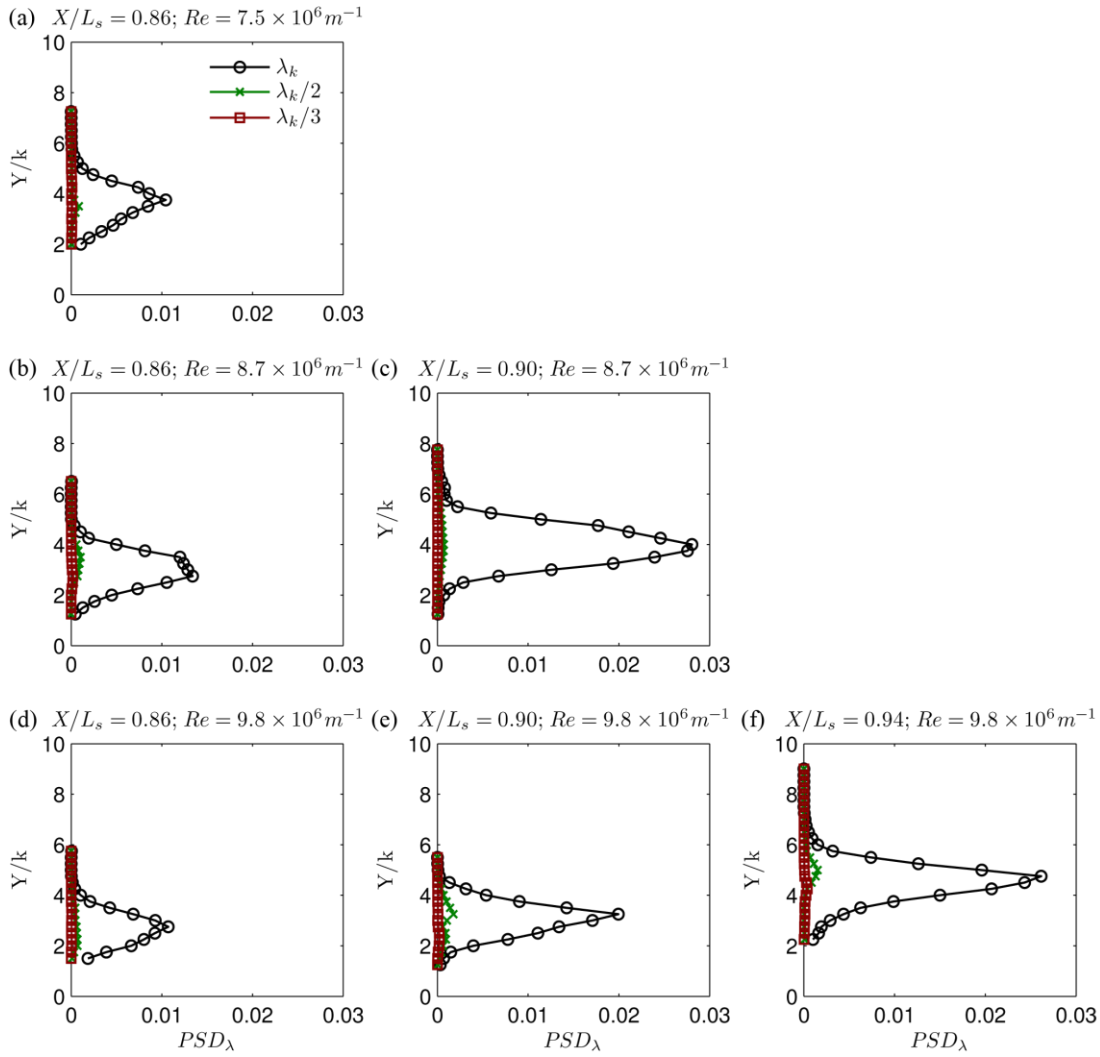

Figure 4-15. Steady disturbance profiles PSD_λ by wavelength component, streamwise location, and Reynolds number.

approximate the slope, *m*. Then a line with slope *m* was extended from the final measurement position to the wall, its contribution integrated analytically and added to the numerical integrals. Strictly, the tails of the disturbance profile are more like a decaying exponential than a straight line, but the overall uncertainty in the final disturbance energy due to this approximation was negligible. The technique described

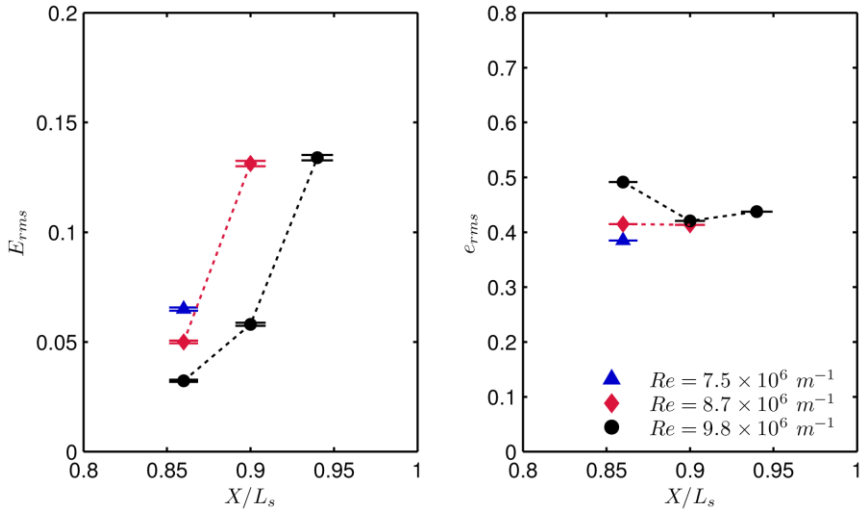

Figure 4-16. Streamwise evolution of total steady disturbance energy E_{rms} and total unsteady disturbance energy e_{rms} .

above was used on the steady and unsteady disturbance profiles from Figure 4-14 and the fundamental wavelength component profiles from Figure 4-15. Additionally, integration on the upper end of the unsteady profiles in Figure 4-14 was cut-off once pressure fluctuations were within 20% of their freestream value.

Integrating the profiles in Figure 4-14 according to Equations 4.10 and 4.11 gives the streamwise evolution of the total steady disturbance energy and the unsteady energy proxy. Figure 4-16 shows these quantities for all Reynolds number cases. The total steady disturbance energy shows significant growth across all Reynolds numbers, whereas the unsteady energy proxy decays or stagnates. This behavior is consistent with a decaying wake instability and the simultaneous growth of streak-related steady disturbances that are distorting the basic state. This corresponds to the mid-wake region measured experimentally at low-speeds for a periodic array of cylindrical roughness

elements (Ergin and White 2006). The previously noted similarities to Kegerise *et al.* (2010) in the Mach number profile and unsteady disturbance profile along the roughness centerline also support the notion that these measurements represent the mid-wake region behind the roughness array.

The streamwise evolution of the steady disturbance energy component by wavelength is given in Figure 4-17 for the fundamental wavelength, λ_k, and its first three harmonics, $\lambda_k/2$, $\lambda_k/3$, and $\lambda_k/4$. This is the result of integrating the profiles in Figure 4-15. The fundamental wavelength is the primary contributor to the overall energy and shows steady growth with increasing distance. The first harmonic, $\lambda_k/2$, is the second largest contributor overall but does not have the steady downstream growth of the fundamental wavelength. For the middle Reynolds number case, the second harmonic, $\lambda_k/3$, may be decaying, but in the higher Reynolds number case, it shows consistent growth. The energy contribution of the third harmonic, $\lambda_k/4$, is small, but, in the highest Reynolds number case in particular, the downstream position shows an increase in energy contribution from this smaller wavelength. The optimal disturbance calculations described in §2.2, which correspond to a sharp cone rather than a blunted one, indicate that the disturbance energy in the fundamental wavelength decays over the measurement region, which is inconsistent with the experiment's observations. Note that here the energy of the optimal disturbance calculation is evaluated using only the *u*-component of the Mack energy norm for consistency with the experiment.

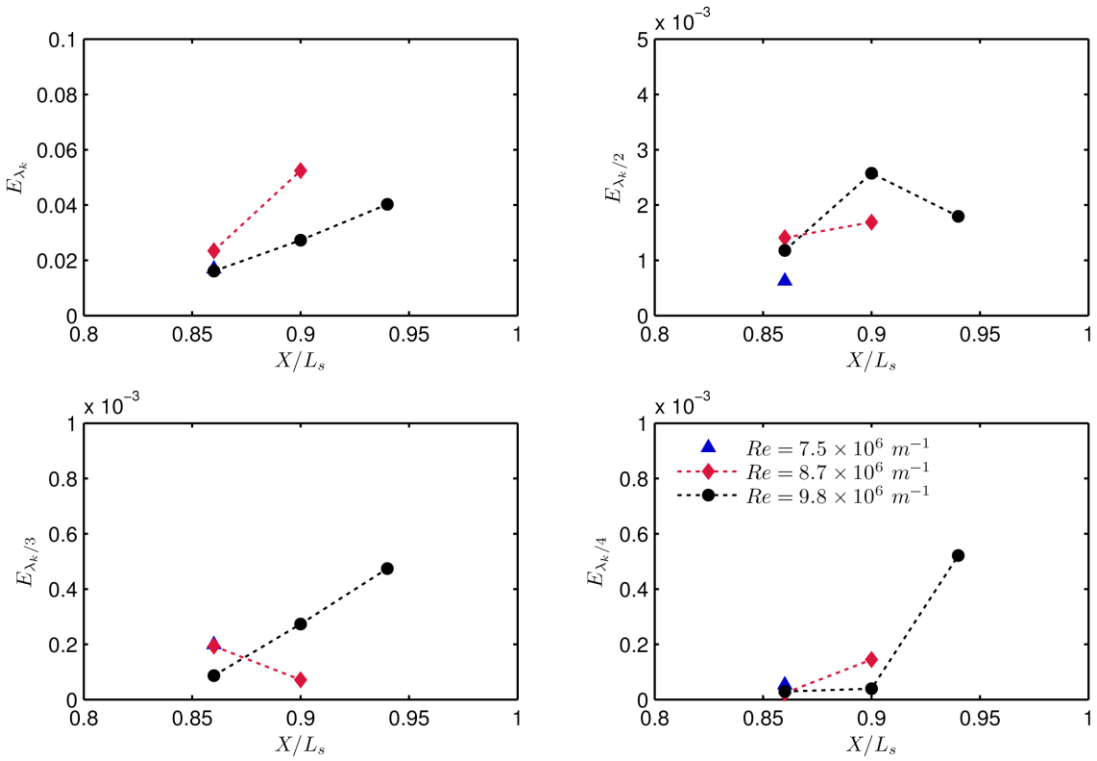

Figure 4-17. Streamwise evolution of steady disturbance energy component E_λ by wavelength.

Although the present experiments are limited in their streamwise extent, the individual wavelength components of the disturbance energy show both growth and decay in Figure 4-17. This is hypersonic roughness-induced transient growth, and, in terms of the disturbance energy's evolution, it shows remarkable similarity to low-speed results. These similarities suggest that low-speed interpretations of roughness effects may be helpful in analyzing high-speed transition.

At both low- and high-speeds, "critical" roughness behavior is observed behind three-dimensional roughness elements when increasing the roughness height results in a sudden upstream shift of the transition front. Ergin and White (2006) describe this

behavior as a competition between unsteady fluctuation growth caused by the roughness wake and the relaxation of the basic state toward spanwise uniformity in the far-wake. Between these lies the mid-wake region in which the unsteady effects of the wake instability are decaying while simultaneously the steady disturbances are transiently growing. Recently, Denissen and White (2013) show that, for incompressible roughness-induced transient growth, this mid-wake region is more unstable to secondary instabilities than the far-wake region. Specifically, the mid-wake region's new basic state, composed of the spanwise-invariant boundary layer and the spanwise-varying, transiently growing streaks, is itself unstable and susceptible to breakdown. The transition seen at the critical roughness height is then the point at which the mid-wake region becomes more unstable to secondary instabilities than the far-wake region is unstable to eigenmode growth.

In the absence of shock-induced unsteadiness (which Iyer and Mahesh (2013) found weak for hemispherical roughness at Mach 3, 5, and 8), the same mechanisms apply to roughness at high-speeds, although the details of their effects likely differ. For discrete roughness at high-speeds, this suggest several possible routes to transition. If the wake instability resulting from perturbation of the shear-layer by the system of vortices wrapped around the roughness creates sufficient unsteadiness, the boundary layer could transition in the near- to mid-wake region. This would account for the type of transition seen with so-called effective roughness. Alternatively, the wake instability may be insufficient to induce transition and instead decays with streamwise distance. Simultaneously, the vortices wrapped around the roughness element generate

transiently-growing streaks through the lift-up effect. If, as in the low-speed case, this mid-wake region is more unstable to secondary instabilities than the far-wake region is to eigenmode growth, then this critical roughness would move the transition location forward from the smooth-wall position.

In the context of the current experiment, no transition, critical or otherwise, is observed in the data. However, the behaviors of the steady disturbance energy and unsteady energy proxy in Figure 4-16 and the increasing distortion of the Mach number contours in Figures 4-2 and 4-3 suggests that the present work also falls into the mid-wake region, where a secondary instability of the modified basic state may be the likely path to transition. Secondary instability calculations based on these measurements are currently being conducted by other researchers.

In considering roughness effects on transition at low-speed versus high-speed, it is worth noting once more the magnitude of the unsteady fluctuations observed in the current experiment, which reach as high as 30% of the total Pitot pressure at the edge without causing transition to turbulence. It has long been understood that it is difficult to trip hypersonic boundary layers to transition with arrays of isolated three-dimensional roughness (Schneider 2008, Reda 2002). Further exploration of roughness-induced transient growth at hypersonic speeds may shed light on why this is the case.

4.6 Reshotko's roughness-induced transition model

Reshotko and Tumin (2004) and Reshotko (2008) present a transient-growth-based model for roughness-induced transition on a flat plate. The underlying concept is that the

energy at transition can be directly related to the energy input via a transient growth factor G:

$$E_{tr} = GE_{in} \tag{4.14}$$

By modeling the input energy using scaling arguments including the roughness height and by assuming that transition occurs once a particular energy level is reached, the model suggests that the Reynolds number at transition can be related to the transient growth factors calculated from optimal disturbances using:

$$\mathrm{Re}_{\theta,tr}\left(\frac{k}{\theta}\right) = \frac{U_e k}{\nu_e} = C\left(\frac{G^{1/2}}{\mathrm{Re}_\theta}\right)^{-1}\left(\frac{T_w}{T_{aw}}\right)^{1/2}\left[1 + r\left(\frac{\gamma-1}{2}\right)M_e^2\right]^{1/2} \tag{4.15}$$

where r is the laminar recovery factor for a boundary layer ($r = \sqrt{\mathrm{Pr}} \approx 0.84$), C is a constant ($C = 12.25$) based on data from an incompressible zero-pressure-gradient boundary layer subject to distributed roughness, and the factor $G^{1/2}/\mathrm{Re}_\theta$ is taken from the appropriate optimal disturbance calculation. Note that the LHS of Equation 4.15 is equivalent to Reda's critical roughness Reynolds number in Equation 1.4 (see discussion in §1.2; Reda 2002). Reshotko and Tumin (2004) use a similar relation for stagnation point flow to successfully correlate transition data for distributed roughness from the PANT dataset and Reda's ballistic range studies (Wool 1975a, 1975b, Reda 2002).

Transition was not observed in the present experiment at any Reynolds number, but the model can still be evaluated in a slightly different form:

$$\frac{U_e k}{\nu_e} < C\left(\frac{G^{1/2}}{\mathrm{Re}_\theta}\right)^{-1}\left(\frac{T_w}{T_{aw}}\right)^{1/2}\left[1 + r\left(\frac{\gamma-1}{2}\right)M_e^2\right]^{1/2} \tag{4.16}$$

	LHS of Equation 4.16	RHS of Equation 4.16
$Re = 7.5 \times 10^6$ m^{-1}	8800	1460
$Re = 8.7 \times 10^6$ m^{-1}	10100	1470
$Re = 9.8 \times 10^6$ m^{-1}	11400	1480

Table 4-3. Transition predictions using the Reshotko model.

In Equation 4.16**,** the RHS can be evaluated using optimal disturbance calculations. This value can then be compared with the experimentally measured LHS of Equation 4.16. If the model correctly describes the present situation, then the experimentally-derived $U_e k / \nu_e$ will be less than the optimal-disturbance-based RHS of Equation 4.16 since transition is not observed.

The optimal disturbance calculations described in §2.2 for a sharp, 5° half-angle cone were used to evaluate the RHS of Equation 4.16 for Reynolds number and temperature conditions equivalent to those of the experiment. The LHS of Equation 4.16 was evaluated using experimental data. A summary of the results is given in Table 4-3. In all cases, the LHS of Equation 4.16 is substantially larger than the value predicted at transition by the RHS, meaning that the model does not accurately describe the present discrete roughness experiment. This is unsurprising, given the large differences in transition location observed between isolated roughness elements and distributed roughness at high-speeds (Reda 2002). Like the stagnation point model, Equation 4.15 is best suited for correlating transition due to distributed roughness, not transition caused by isolated elements or arrays of discrete roughness.

4.7 Survey of recent high-speed roughness-induced transition results

Numerous recent studies have considered the effects of isolated roughness elements in super- and hypersonic flow both experimentally (Danehy *et al.* 2007, Borg and Schneider 2008, Danehy *et al.* 2009, Danehy *et al.* 2010, Bathel *et al.* 2010, Kegerise *et al.* 2010, Casper *et al.* 2011, Wheaton and Schneider 2012 and 2013, Bathel *et al.* 2013) and computationally (Choudhari *et al.* 2010, Bartkowicz *et al.* 2010, Iyer and Mahesh 2013). It is illustrative to compare these studies and the present work in a summary of recent high-speed roughness-induced transition results.

Since these results include roughness on flat plates, oblique wedges, and cones of various geometry, the reported data for each study have been converted into four variables relevant to a zero-pressure-gradient compressible boundary layer: edge Mach number M_e, edge unit Reynolds number Re_e, adiabatic wall temperature ratio T_w/T_{aw}, and roughness height ratio k/δ. Note that the edge Reynolds number is *not* equivalent to the Reynolds number at transition.

Each study had its own method for calculating the boundary layer thickness used to compare to roughness height; some authors used a definition based on enthalpy whereas others chose values based on velocity. (For example, lacking simulations of the smooth-wall blunt-nosed cone, the data from the current experiment is displayed using the boundary layer thickness at 99% of the edge mass-flux value based on a sharp, 5° half-angle cone.) It is, therefore, troublesome to compare one study to another in a strict numerical fashion. Instead, they have been divided into categories based on roughness

smaller than the boundary layer ($k/\delta < 0.8$), roughness of the order of the boundary layer ($0.8 < k/\delta < 1.2$), and roughness larger than the boundary layer ($k/\delta > 1.2$).

Similarly, authors have included varying degrees of information about their wall temperature conditions. In some cases, wall temperatures have been projected for studies based on their counterpart simulation or other experiments using the same facility. The data break down into two basic categories: cold-wall data ($T_w/T_{aw} > 0.5$) and near-adiabatic wall data ($T_w/T_{aw} \sim 0.8$-1.0).

In addition to compiling the boundary-layer characteristics of each study, the transition status of each flow is noted. In general, a flow was classified as laminar or transitional unless the authors noted an explicit transition to turbulence within the observation region. In particular, this means that some experimental studies are marked as laminar/transitional when the flow may transition to turbulence at this edge Reynolds number, albeit outside of the measured region.

The data represent an assortment of roughness element shapes and include varying levels of freestream influence, from quiet-flow experiments and DNS to conventional hypersonic tunnels. The data are displayed graphically in Figures 4-18 and 4-19. The current study, shown in square data points in both figures, falls squarely within the bounds of the other recent studies.

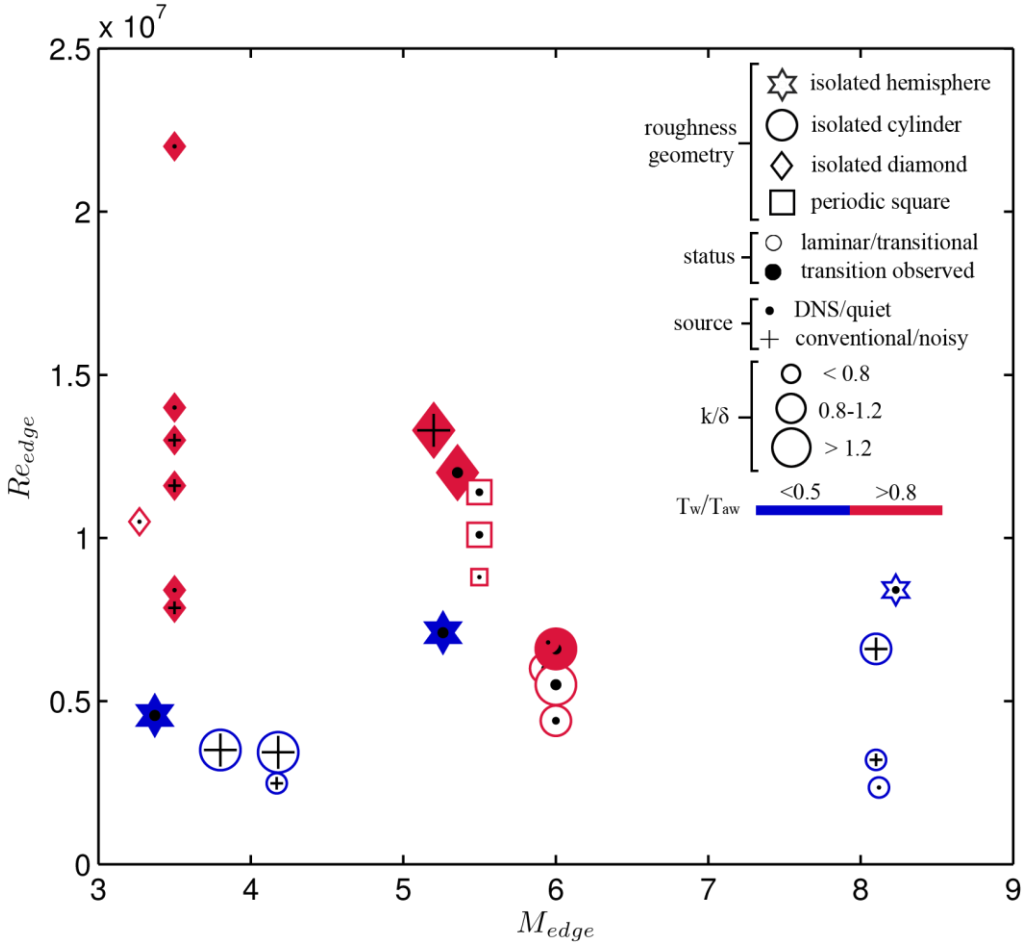

Figure 4-18. Summary of recent high-speed roughness-induced transition studies by edge Mach number and Reynolds number. Data are included from Kegerise *et al.* (2010), Bartkowicz *et al.* (2010), Danehy *et al.* (2010), Bathel *et al.* (2010, 2013), Casper *et al.* (2011), Wheaton and Schneider (2012, 2013), Iyer and Mahesh (2013), and the current work.

Figure 4-18 shows recent hypersonic results as a function of edge Mach number and Reynolds number. The data indicate that compressibility is generally stabilizing to roughness-perturbed flows, with transition to turbulence occurring at lower edge Reynolds numbers for lower Mach numbers. For a given Mach number, transition to

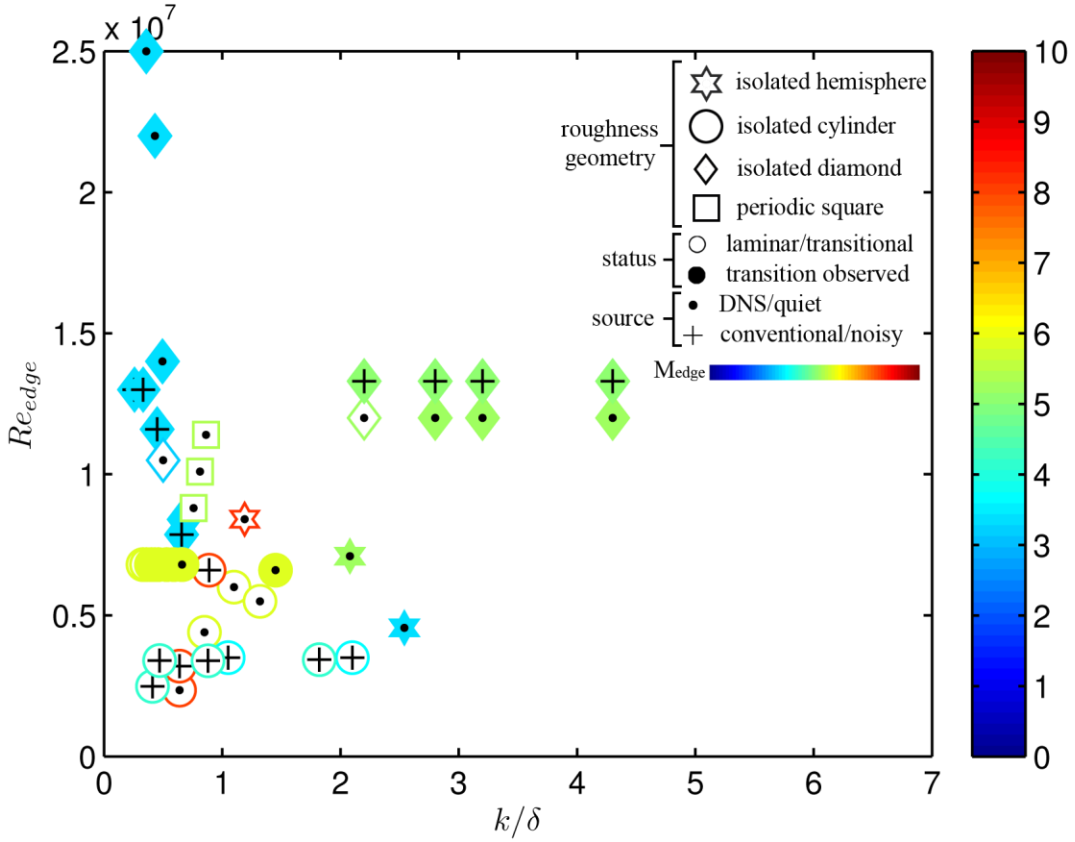

Figure 4-19. Summary of recent high-speed roughness-induced transition studies by roughness height and Reynolds number. Data are included from Kegerise *et al.* (2010), Bartkowicz *et al.* (2010), Danehy *et al.* (2010), Bathel *et al.* (2010, 2013), Casper *et al.* (2011), Wheaton and Schneider (2012, 2013), Iyer and Mahesh (2013), and the current work.

turbulence also appears to occur at lower Reynolds numbers when the roughness element is larger than the boundary layer, as one would expect.

Alternatively, one can look at the data in terms of k/δ and Reynolds number, recalling the earlier caveat that each study's estimation of δ relies on a different estimation method; this is shown in Figure 4-19. This highlights the likelihood of very large roughness elements to cause transition to turbulence. Among roughness heights smaller than the boundary layer thickness, transition is only seen for cases when the

Reynolds number is very high—and the edge Mach number low (Kegerise *et al.* 2010)—or for studies in which the streamwise distance over which the boundary layer developed is very large (Wheaton and Schneider 2013). Oddly enough, there are no transitioned data points for roughness elements approximately the same height as the boundary layer, although this is likely more indicative of the sparseness of the data set and the limitations of finite observable streamwise expanse than an indication of boundary-layer physics.

Presently, the data set is too sparse to estimate what roughness element height will cause transition for a given Mach number and Reynolds number combination or even what effect roughness shape has on transition. Although it is known that noisy flow causes transition at lower Reynolds numbers than quiet flow (Borg and Schneider 2008, Kegerise *et al.* 2010, Casper *et al.* 2011), there are no obvious patterns in the data set depending on the presence of freestream noise. This, too, is likely a result of the sparseness of the current data. With the addition of appropriate historic data and continuing super- and hypersonic studies of discrete roughness elements in zero-pressure-gradient boundary layers, these trends may grow clearer.

5. CONCLUSIONS

It is the objective of this work to provide the first quantitative measurements of experimentally-realized, roughness-induced transient growth in a hypersonic boundary layer. In the past decade, experiments and numerical simulations at subsonic speeds have advanced the physics-based understanding of roughness effects on boundary layer transition, while simultaneously revealing significant differences between optimal disturbances and experimentally-realized transient growth. For compressible boundary layers, the only transient growth analysis prior to this work was for optimal disturbances.

In order to measure roughness effects on transient growth, a 5° half-angle straight cone model with interchangeable nosetips was designed and manufactured. Experiments were conducted using a slightly blunted nosetip with a ring array of 18 periodically-spaced cube-like discrete roughness elements 1-mm tall by 1.78-mm wide by 1.78-mm long. Additional nosetips were also manufactured for the experimental model to facilitate future studies including the effects of varying nose bluntness and distributed, rather than discrete, roughness.

An experimental technique for measuring high-speed transient growth was designed and executed using high-bandwidth Pitot tube measurements. The limited run-time of hypersonic low-disturbance facilities relative to their subsonic counterparts necessitated combining data from numerous runs into a single data set with carefully matched experimental conditions. In particular, significant run-to-run variations were observed for adiabatic wall temperature ratios that varied by less than 11%. This variation highlights the importance—not only for transient growth experiments but for

all high-speed roughness experiments—of monitoring and recording wall temperature variations between runs. The final data sets used to analyze transient growth behavior represented 111 on-condition runs and approximately 46 minutes of quiet hypersonic flow, divided across three Reynolds number conditions.

Prior high-speed transient growth studies consisted of compressible optimal disturbance calculations using the Mack energy norm to optimize disturbance growth. As the first experiment to examine high-speed transient growth, this work analyzed disturbance energy using a simplified version of the Mack energy norm that considered only velocity-dependent terms. This experimental analysis was explicitly related to that used in optimal disturbance calculations so that the present measurements can be compared with such simulations.

Pitot measurements revealed azimuthally-alternating regions of high- and low-momentum fluid in the cone boundary layer. Low-speed streaks were centered behind roughness elements and were generally stronger than the high-speed streaks between roughness elements. Transition was not observed, but the steady disturbances did intensify with streamwise distance and caused increasing distortion of the boundary layer. Unsteady disturbances as large as 30% of the total Pitot pressure at the edge were insufficient to trip to turbulence and decayed with increasing distance. Mean and fluctuating profiles along the roughness centerline resembled those along the centerline of an isolated diamond roughness element in supersonic flow (Kegerise *et al.* 2010).

Analysis of the total steady disturbance energy showed what appears to be algebraic growth of streaks across the measurement region. The total unsteady energy, in

contrast, decayed or stagnated with increasing streamwise distance. This behavior is consistent with low-speed experiments of transient growth in the mid-wake region behind periodically-spaced cylindrical roughness (Ergin and White 2006). When decomposed by wavelength, the fundamental wavelength's disturbance energy component dominated, although transient growth and decay were also observed in other wavelengths.

This work's steady and unsteady measurements bear strong resemblance to recent studies of high-speed roughness-induced transition. At the same time, this work's disturbance energy evolution behaves much like low-speed roughness-induced transient growth experiments. This similarity suggests that further studies of high-speed roughness effects following the vein of low-speed transient growth work may provide insight into the underlying physics.

The work in this dissertation makes several significant contributions to the understanding of hypersonic transition to turbulence. It represents the first quantitative measurements of experimentally-realized, roughness-induced transient growth in a hypersonic boundary layer. The work establishes a methodology for making high-speed transient growth measurements given the short run-times of hypersonic blow-down facilities, and it provides a framework for relating experimental measurements to optimal disturbance calculations for the benefit of future studies. Finally, the disturbance energy evolution of this experimentally-realized hypersonic transient growth, and its resemblance to similar results at low-speeds, sets the stage for future studies of high-

speed roughness-induced transition. To that end, recommendations for future work are given in the following section.

6. RECOMMENDATIONS

Several recommendations are made for future research in high-speed roughness-induced transient growth. Below, these recommendations are discussed for hypersonic transient growth experiments in general and in specific detail for future studies conducted in the M6QT using the TG Cone model. Additionally, several avenues for future computational, theoretical, and experimental studies are suggested.

6.1 Guidelines for hypersonic transient growth experiments

The current investigation utilized a slightly-blunted nosetip and an array of periodically-spaced discrete roughness elements of the order of the boundary layer thickness to conduct the first quantitative measurements of transient growth. The bluntness of the nose added a complicating factor to the investigation. Experimentally, it increased the blockage of the model, thereby complicating start-up of hypersonic flow. The bluntness of the nose also hindered numerical simulations for the geometry, both with and without roughness. The purpose of the bluntness was to inhibit growth of the second-mode instability; however, for the straight cone geometry and Reynolds numbers achievable in the M6QT, it is unlikely that second-mode instabilities would have achieved sufficient growth to be a factor, even without the blunted nosetip.

Given the nascent state of high-speed transient growth experiments, it is recommended that future studies begin with the simplest base geometries (i.e. an aerodynamically sharp flat-plate and/or cone) and roughness geometries before progressing to more complicated ones. Isolated and periodically-spaced discrete roughness elements can be used as stepping stones toward measurements of transient

growth with distributed roughness, as has been done at low-speed (White *et al.* 2005, Rizzetta and Visbal 2007, Downs *et al.* 2008, Drews *et al.* 2011). Given the significant run-to-run variations described in §3.4.1, future experimental studies should also closely monitor—if not independently control—the model wall temperature between and during runs.

6.2 Facility- and model-specific recommendations

The Transient Growth Cone, described in §2.1, provides a good baseline model for use in transient growth experiments. Additional existing nosetips, including quasi-random distributed roughness, are available for future studies, and new nosetips following the guidelines in §6.1 can be manufactured to fit the existing frustrum and sting shaft. Additionally, the hollow frustum can be retrofitted with instrumentation and other modifications to simplify future experiments. Integrating thermocouples along a ray of the frustum would help monitor wall temperature during and between runs, and, for roughness configurations in which transition occurs, would aid in determining transition location. One or more static pressure ports would improve conversions from total pressure measurements to Mach number, and, if mounted on opposite rays of the model, could be used to align the model relative to the flow.

Currently, nosetips are attached to the frustum as screws using a chemical threadlocker for added security. The threadlocker has proven overly secure, causing difficulties in removing nosetips using hand tools without damaging either the nosetip or the frustum. Because nosetips attach to the frustum via a fully-threaded through-hole, it

is recommended that new nosetips extend further into the frustum and be secured from behind during an experiment using hardware in place of chemical threadlocker.

Future experiments conducted in the M6QT will also benefit from the new three-axis azimuthal traverse currently undergoing shakedown testing. This traverse will enable future experiments to reach a larger azimuthal range and streamwise extent on the model. Additionally, the traverse's range of motion is sufficient to determine model alignment through measurement of boundary layer profiles on different rays of the cone.

In terms of diagnostics, future experiments in the M6QT would benefit from a Pitot probe with a smaller mouth using a permanently-mounted non-threaded pressure sensor (such as the Kulite XCE-093, unavailable at the time of testing) located as near to the mouth of the probe as possible. This would provide improved spatial resolution without sacrificing frequency response. Additionally, avoiding the Endevco Model 136 signal conditioner (§3.2.1) would enable evaluation of the spectral content within the wake instability, which would be useful for comparison with existing roughness transition experiments and computations.

6.3 On-going and future research objectives

As mentioned in §2.2, several computational efforts based on the geometry of the present work are on-going with researchers at University of California, Los Angeles and Texas A&M University. Results for the smooth-wall experimental geometry will enable better comparisons with existing roughness transition data in terms of k/δ and Re_{kk}, the Reynolds number based on roughness height and smooth-wall conditions at the roughness location. The smooth wall basic state can also be used for optimal disturbance

calculations as in §2.2, allowing more direct comparison between the experiment and optimal disturbance theory.

Direct numerical simulations including the periodic roughness are also underway. Once complete, comparison of the computational results with this experiment should indicate the effects of factors unmeasured in the present work. In particular, the disturbance energy will be observable over a larger streamwise extent, and it will be feasible to evaluate the impact of temperature disturbances—which were ignored in the experiment—on the evolution of disturbance energy. Moreover, a full DNS will provide the data necessary to extend Denissen's (2011) decomposition technique to compressible boundary layers, which would enable analysis of roughness receptivity via the continuous spectrum. Such an analysis may provide insight into the differences between optimal and experimentally-realized disturbance growth at high-speeds.

It is worth noting that existing high-speed roughness studies, particularly DNS results like those of Choudhari *et al.* (2010), Bartkowicz *et al.* (2010), and Iyer and Mahesh (2013), could be re-examined through the lens of transient growth by analyzing the streamwise evolution of their disturbance growth. Iyer and Mahesh (2013) is a particularly attractive candidate for such analysis, since the data include a range of edge Mach numbers and cases with and without observed transition.

Finally, there is tremendous opportunity to expand experimental studies of high-speed transient growth. At present, the methodology developed in this work is feasible only for facilities with sufficiently long run-times at a constant condition to enable detailed scans within the boundary layer. Such measurements are possible in other quiet

and conventional high-speed facilities. Experiments in other facilities can also benefit from the use of diagnostic techniques not possible in the M6QT due to its limited optical access. Techniques such as planar laser-induced fluorescence or temperature sensitive paint would give insight into the evolution of temperature disturbances behind roughness, a factor that was unobservable in the present work. In particular, the latter technique could be readily used on an identical geometry at quiet conditions comparable to the present work inside Purdue University's Boeing/AFOSR Mach 6 Quiet Tunnel. Such an experiment would be in keeping with the recommendations of the Transition Study Group (Reshotko 1976) that common experiments and geometries be tested across different facilities, allowing researchers to better gauge facility effects and providing context for overall conclusions.

REFERENCES

BARTKOWICZ, M. D., SUBBAREDDY, P. K., AND CANDLER, G. V. 2010. Numerical simulations of roughness induced instability in the Purdue Mach 6 wind tunnel. *AIAA Paper 2010-4723*.

BATHEL, B. F., DANEHY, P.M., INMAN, J. A., WATKINS, A. N., JONES, S. B., LIPFORD, W. E., GOODMAN, K. Z., IVEY, C. B., AND GOYNE, C. P. 2010. Hypersonic laminar boundary layer velocimetry with discrete roughness on a flat plate. *AIAA Paper 2010-4998*.

BATHEL, B. F., DANEHY, P. M., JONES, S. B., JOHANSEN, C. T., AND GOYNE, C. P. 2013. Trip-induced transition measurements in a hypersonic boundary layer using molecular tagging velocimetry. *AIAA Paper 2013-0042*.

BATT, R. G., AND LEGNER, H. H. 1983. A review of roughness-induced nosetip transition. *AIAA J.* **21**(1), 7-22.

BLANCHARD, A. E., AND SELBY, G. V. 1996. An experimental investigation of wall cooling effects on hypersonic boundary-layer stability in a quiet wind tunnel. *NASA CR 198287*.

BORG, M. P., AND SCHNEIDER, S. P. 2008. Effect of freestream noise on roughness-induced transition for the X-51A forebody. *J. Spacecraft Rockets*. **45**(6), 1106-1116.

BUTLER, K., AND FARRELL, B. 1992. Three-dimensional optimal perturbations in viscous shear flow. *Phys. Fluids A*. **4**(8), 1637-1650.

CASPER, K. M., JOHNSON, H. B. AND SCHNEIDER, S. P. 2011. Effect of freestream noise on roughness-induced transition for a slender cone. *J. Spacecraft Rockets.* **48**(3), 406-413.

CHOUDHARI, M., LI, F., WU, M., CHANG, C., EDWARDS, J., KERGERISE, M., AND KING, R. A. 2010. Laminar-turbulent transition behind discrete roughness elements in a high-speed boundary layer. *AIAA Paper 2010-1575*.

DANEHY, P. M., GARCIA, A. P., BORG, S., DYAKONOV, A. A., BERRY, S. A., INMAN, J. A., ALDERFER, D. W. 2007. Fluorescence visualization of hypersonic flow past triangular and rectangular boundary-layer trips. *AIAA Paper 2007-536.*

DANEHY, P. M., BATHEL, B., IVEY, C., INMAN, J. A., JONES, S. B. 2009. NO PLIF study of hypersonic transition over a discrete hemispherical roughness element. *AIAA Paper 2009-394*.

DANEHY, P. M., IVEY, C. B., INMAN, J. A., BATHEL, B. F., JONES, S. B., MCCREA, A. C., JIANG, J., WEBSTER, M., LEMPERT, W., MILLER, J., AND MEYER, T. 2010. High-

speed PLIF imaging of hypersonic transition over discrete cylindrical roughness. *AIAA 2010-703.*

DENISSEN, N. A. 2011. *Roughness-induced transient growth: Continuous-spectrum receptivity and secondary instability analysis.* Ph.D. Thesis. Texas A&M University, College Station, Texas.

DENISSEN, N. A., AND WHITE, E. B. 2009. Continuous spectrum analysis of roughness-induced transient growth. *Phys. Fluids.* **21**, 114105-(1-13).

DENISSEN, N. A., AND WHITE, E. B. 2013. Secondary instability of roughness-induced transient growth. *Phys. Fluids.* **25**, 114108-(1-18).

DOWNS III, R. S., WHITE, E. B., AND DENISSEN, N. A. 2008. Transient growth and transition induced by random distributed roughness. *AIAA J*. **46**(2), 451-462.

DREWS, S. D., DOWNS III, R. S., DOOLITTLE, C. J., GOLDSTEIN, D. B., AND WHITE, E. B. 2011. Direct numerical simulations of flow past random distributed roughness. *AIAA Paper 2011-564.*

ELLINGSEN, T., AND PALM, E. 1975. Stability of linear flow. *Phys. Fluids*. **18**, 487-488.

ERGIN, F. G., AND WHITE, E. B. 2006. Unsteady and transitional flow behind roughness elements. *AIAA J.* **44**(11), 2504-2514.

FRANSSON, J. H. M., BRANDT, L., TALAMELLI, A., AND COSSU, C. 2004. Experimental and theoretical investigation of the non-modal growth of steady streaks in a flat plate boundary layer. *Phys. Fluids.* **16**, 3627-3638.

HANIFI, A., SCHMID, P. J., AND HENNINGSON, D. S. 1996. Transient growth in compressible boundary layer flow. *Phys. Fluids.* 8(3), 826-837.

HOFFERTH, J. W. 2013. *Boundary-layer stability and transition on a flared cone in a Mach 6 quiet tunnel.* Ph.D. Thesis. Texas A&M University, College Station, Texas.

HOFFERTH, J. W., BOWERSOX, R. D. W., AND SARIC, W. S. 2010. The Mach 6 Quiet Tunnel at Texas A&M: Quiet flow performance. *AIAA Paper 2010-4794.*

HOFFERTH, J. W., AND SARIC, W. S. 2012. Boundary-layer transition on a flared cone in the Texas A&M Mach 6 Quiet Tunnel. *AIAA Paper 2012–0923*.

IYER, P. S., AND MAHESH, P. 2013. High-speed boundary-layer transition induced by a discrete roughness element. *J. Fluid Mech.* **729**, 524-562.

KEGERISE, M. A., OWENS, L. R., AND KING, R. A. 2010. High-speed boundary-layer transition induced by an isolated roughness element. *AIAA Paper 2010-4999*.

KIMMEL, R. L., ADAMCZAK, D., GAITONDE, D., ROUGEUX, A., AND HAYES, J. R. 2007. HIFiRE-1 boundary layer transition experiment design. *AIAA Paper 2007-534.*

LANDAHL, M. T. 1980. A note on an algebraic instability of inviscid parallel shear flows. *J. Fluid Mech.* **98**, 243-251.

LAUFER, G., MCKENZIE, R. L., AND FLETCHER, D. G. 1990. Method for measuring temperatures and densities in hypersonic wind tunnel air flows using laser-induced O_2 fluorescence. *Appl. Opt.* **29**(33), 4873-4883.

MACK, L. M. 1969. Boundary-layer stability theory. *Jet Propulsion Laboratory*, Pasadena, California.

MACK, L. M. 1984. Boundary-layer stability theory. *AGARD Rep. No. 709*, Von Karman Inst., Rhode-St.-Genese, Belgium.

MORKOVIN, M. V. 1969. Critical evaluation of transition from laminar to turbulent shear layers with emphasis on hypersonically traveling bodies. *Air Force Flight Dyn. Lab. Rep.* AFFDL-TR-68-149, Baltimore, Maryland.

MORKOVIN, M. V., RESHOTKO, E., AND HEBERT, T. 1994. Transition in open flow systems: A reassessment. *Bull. APS*. **39**(9), 1-31.

REDA, D. C. 2002. Review and synthesis of roughness-dominated transition correlations for re-entry applications. *J. Spacecraft Rockets.* **39**(2), 161-167.

REDA, D. C., WILDER, M. C., BOGDANOFF, D. W., AND PRABHU, D. K. 2008. Transition experiments on blunt bodies with distributed roughness in hypersonic free flight. *J. Spacecraft Rockets*. **45**(2), 210-215.

REDA, D. C., WILDER, M. C., AND PRABHU, D. K. 2010. Transition experiments on blunt bodies with isolated roughness elements in hypersonic flight. *J. Spacecraft Rockets*. **47**(5), 828-835.

REDA, D. C., WILDER, M. C., AND PRABHU, D. K. 2012a. Transition experiments on slightly blunted cones with distributed roughness in hypersonic flight. *AIAA J.* **50**(10), 2248-2254.

REDA, D. C., WILDER, M. C., AND PRABHU, D. K. 2012b. Transition experiments on large bluntness cones with distributed roughness in hypersonic flight. *AIAA Paper 2012-0446*.

REDA, D. C., WILDER, M. C., AND PRABHU, D. K. 2013. Transition experiments on blunt cones with distributed roughness in hypersonic flight. *J. Spacecraft Rockets*. **50**(3), 504-508.

RESHOTKO, E. 1976. Boundary-layer stability and transition. *Ann. Rev. Fluid Mech.* **8**, 311–349.

RESHOTKO, E. 2001. Transient growth: A factor in bypass transition. *Phys. Fluids*. **13**, 1067-1075.

RESHOTKO, E. 2008. Roughness-induced transition, experiment and modeling. *AIAA Paper 2008-4294.*

RESHOTKO, E., AND TUMIN, A. 2004. Role of transient growth in roughness-induced transition. *AIAA J*. **42**(4), 766-770.

RIZZETTA, D. P., AND VISBAL, M. R. 2007. Direct numerical simulations of flow past an array of distributed roughness elements. *AIAA J.* **45**(8), 1967-1976.

SARIC, W. S. 1994. Görtler vortices. *Ann. Rev. Fluid Mech.* **26**, 379-409.

SARIC, W. S., REED H. L., AND WHITE, E. B. 2003. Stability and transition of three-dimensional boundary layers. *Ann. Rev. Fluid Mech.* **35**, 413-440.

SCHMID, P. J., AND HENNINGSON, D. S. 2001. *Stability and transition in shear flows*. Springer, New York City, New York.

SCHNEIDER, S. P. 2008. Effects of roughness on hypersonic boundary-layer transition. *J. Spacecraft Rockets*. **45**(2), 193-209.

SHARP, N. S., AND WHITE, E. B. 2014. Roughness-induced transient growth on a hypersonic blunt cone. *AIAA Paper 2014-0432*.

SMITS, A. J., HAYAKAWA, K., AND MUCK, K. C. 1983. Constant temperature hot-wire anemometer practice in supersonic flows. *Exp. Fluids*. **1**(2), 83-92.

TEMPELMANN, D., HANIFI, A., AND HENNINGSON, D. S. 2012. Spatial optimal growth in three-dimensional compressible boundary layer. *J. Fluid Mech.* **704**, 251-279.

TUMIN, A. 2003. Multimode decomposition of spatially growing perturbations in a two-dimensional boundary layer. *Phys. Fluids.* **15**(9), 2525-2540.

TUMIN, A. 2011. The biorthogonal eigenfunction system of linear stability equations: A survey of applications to receptivity problems and to analysis of experimental and computational results. *AIAA Paper 2011-3244.*

TUMIN, A., AND RESHOTKO, E. 2001. Spatial theory of optimal disturbances in boundary layers. *Phys. Fluids*. **13**(7), 2097-2104.

WHEATON, B. M., AND SCHNEIDER, S. P. 2012. Roughness-induced instability in a hypersonic laminar boundary layer. *AIAA J*. **50**(6), 1245-1256.

WHEATON, B. M., AND SCHNEIDER, S. P. 2013. Hypersonic boundary-layer instability to near-critical roughness. *J. Spacecraft Rockets.* AIAA Early Edition, doi: 10.2514/1.A32554, 1-16.

WHITE, E. B. 2002. Transient growth of stationary disturbances in a flat plate boundary layer. *Phys. Fluids.* **14**, 4429-4439.

WHITE, E. B., RICE, J. M., AND ERGIN, F. G. 2005. Receptivity of stationary transient disturbances to surface roughness. *Phys. Fluids.* **17**, 064109-(1-12).

WHITEHEAD, A. H. 1969. Flow field and drag characteristics of several boundary-layer tripping elements in hypersonic flow. *NASA Langley Research Center*. TN D-5454, Hampton, Virginia.

WILKINSON, S. P. 1997. A review of hypersonic boundary layer stability experiments in a quiet Mach 6 wind tunnel. *AIAA Paper 1997-1819*.

WOOL, M. R. 1975a. Final summary report Passive Nosetip Technology (PANT) program. *Acurex Corporation*. SAMSO-TR-75-250, Mountain View, California.

WOOL, M.R. 1975b. Passive Nosetip Technology (PANT) program, Volume X, Summary of experimental and analytical results. *Acurex Corporation*. SAMSO-TR-74-86, Mountain View, California.

ZUCCHER S., TUMIN, A., AND RESHOTKO, E. 2006. Parabolic approach to optimal perturbations in compressible boundary layers. *J. Fluid Mech.* **556**, 189-216.

ZUCCHER, S., SHALAEV, I., TUMIN, A., AND RESHOTKO, E. 2007. Optimal disturbances in the supersonic boundary layer past a sharp cone. *AIAA J*. **45**(2), 366-373.

APPENDIX A

FIGURES

The figures contained within this appendix are enlarged versions of the figures in §4.

They are included for comparisons with future experiments and simulations.

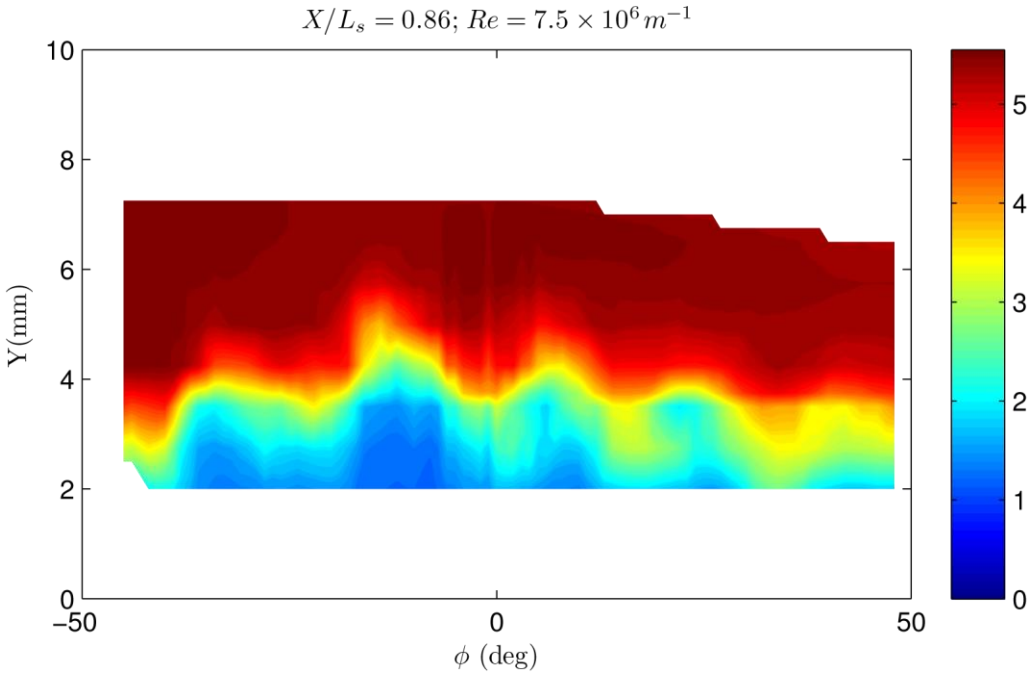

Figure A-1. Enlarged version of Figure 4-2(a). Contours of Mach number at X/L_s = 0.86 and Re = 7.5 × 10^6 m^{-1}.

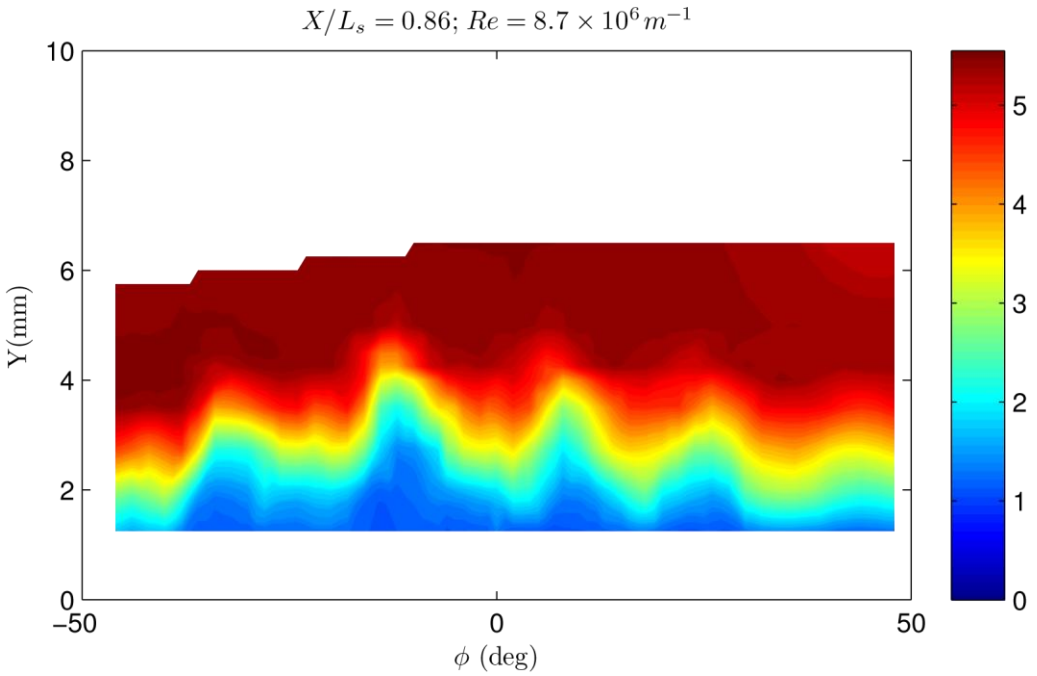

Figure A-2. Enlarged version of Figure 4-2(b). Contours of Mach number at $X/L_s = 0.86$ and $Re = 8.7 \times 10^6$ m^{-1}.

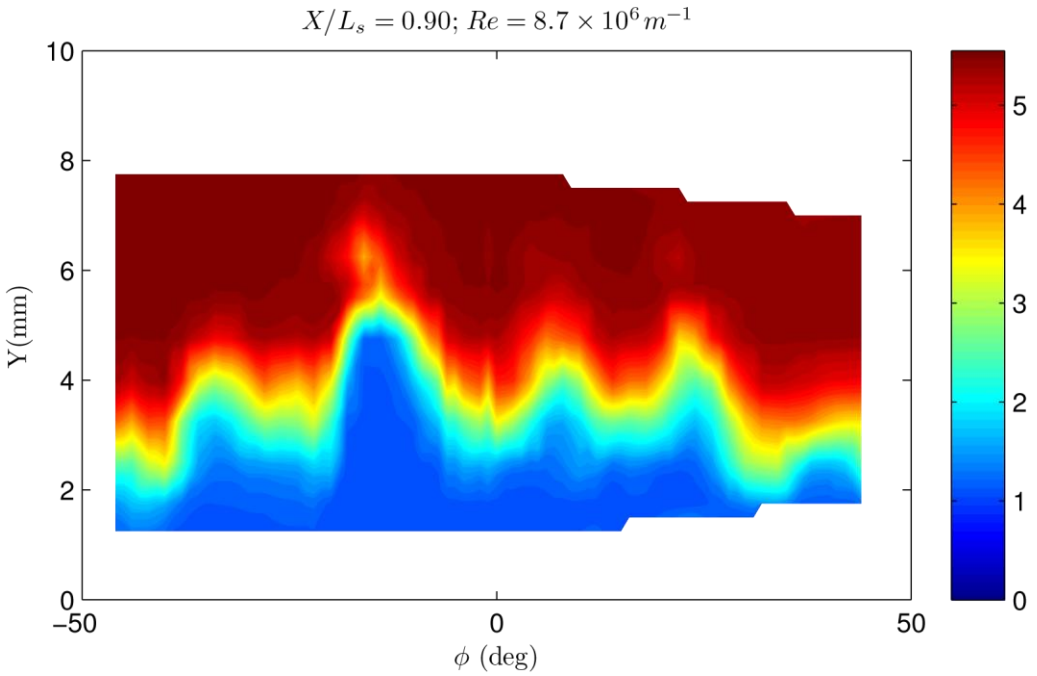

Figure A-3. Enlarged version of Figure 4-2(c). Contours of Mach number at $X/L_s = 0.90$ and $Re = 8.7 \times 10^6$ m^{-1}.

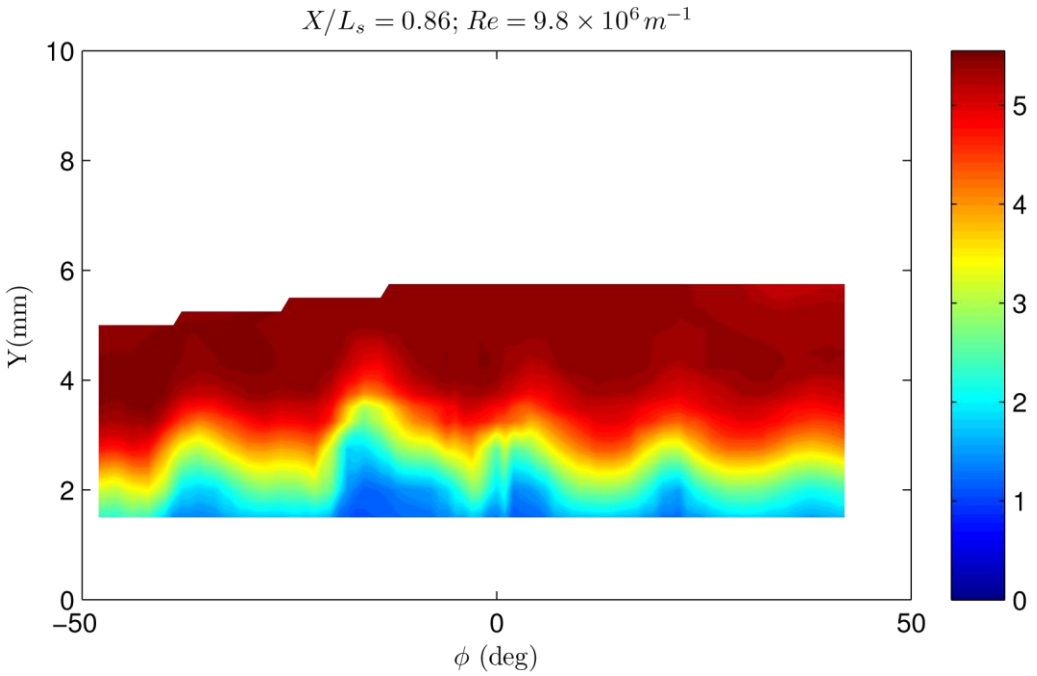

Figure A-4. Enlarged version of Figure 4-2(d). Contours of Mach number at $X/L_s = 0.86$ and $Re = 9.8 \times 10^6$ m^{-1}.

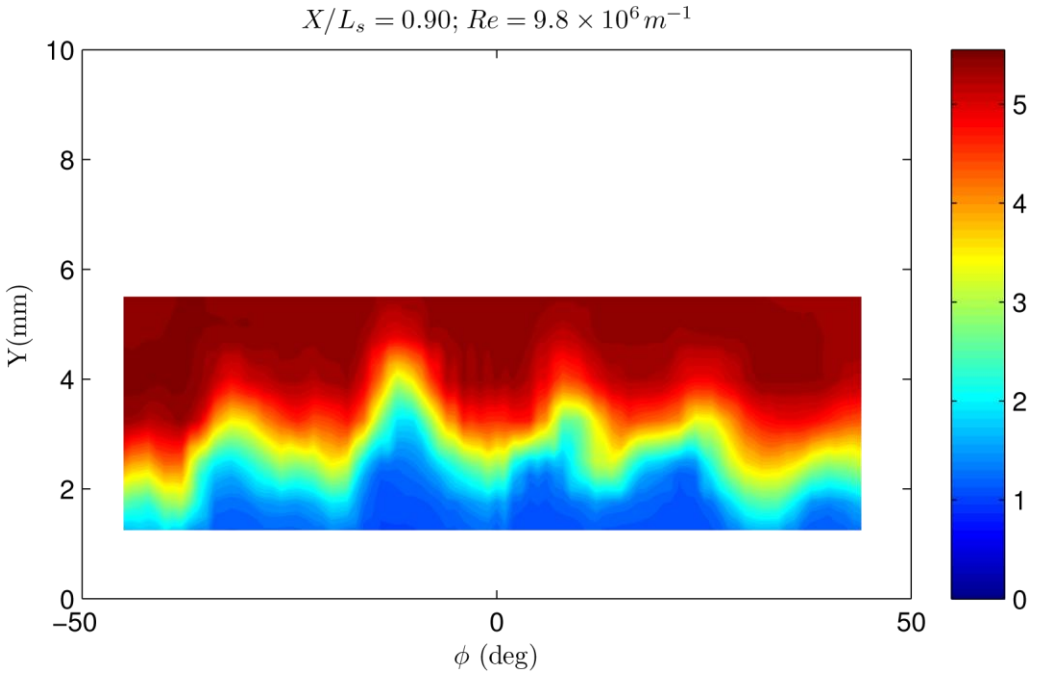

Figure A-5. Enlarged version of Figure 4-2(e). Contours of Mach number at $X/L_s = 0.90$ and $Re = 9.8 \times 10^6$ m^{-1}.

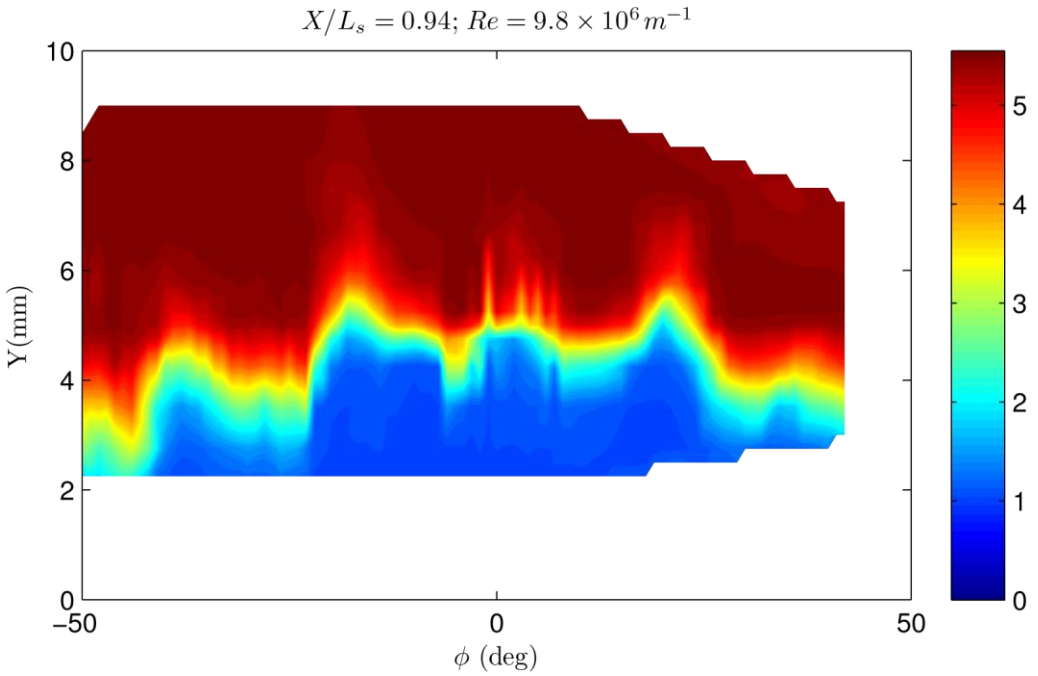

Figure A-6. Enlarged version of Figure 4-2(f). Contours of Mach number at $X/L_s = 0.94$ and $Re = 9.8 \times 10^6$ m^{-1}.

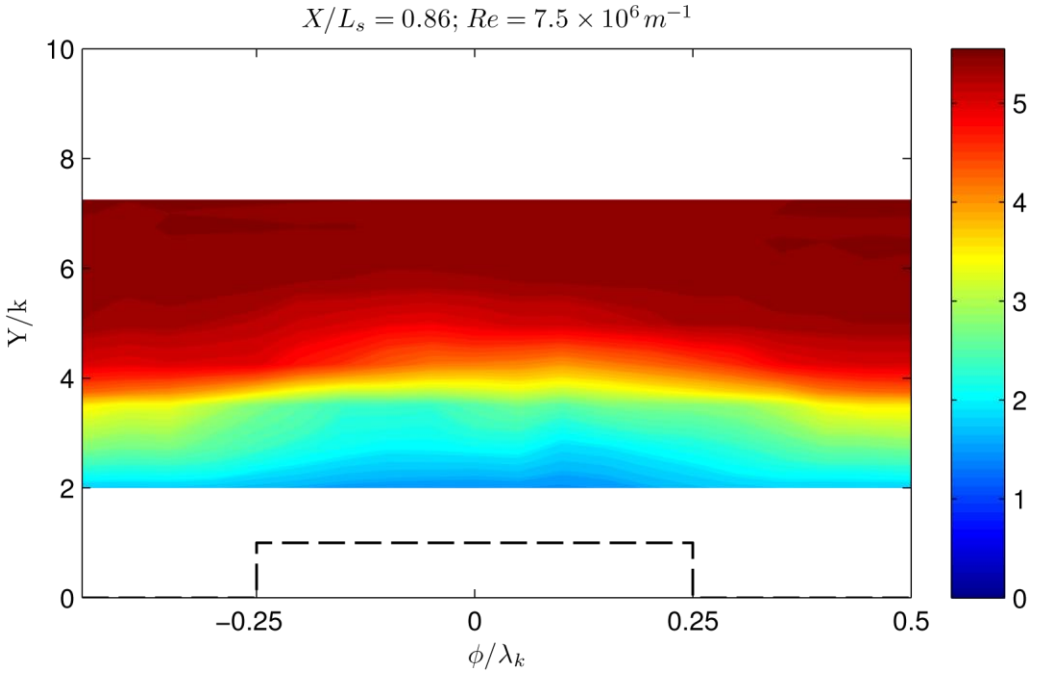

Figure A-7. Enlarged version of Figure 4-3(a). Phase-locked averaged contours of Mach number at $X/L_s = 0.86$ and $Re = 7.5 \times 10^6$ m^{-1}. Dashed lines indicate the projection of a roughness element into the measurement plane.

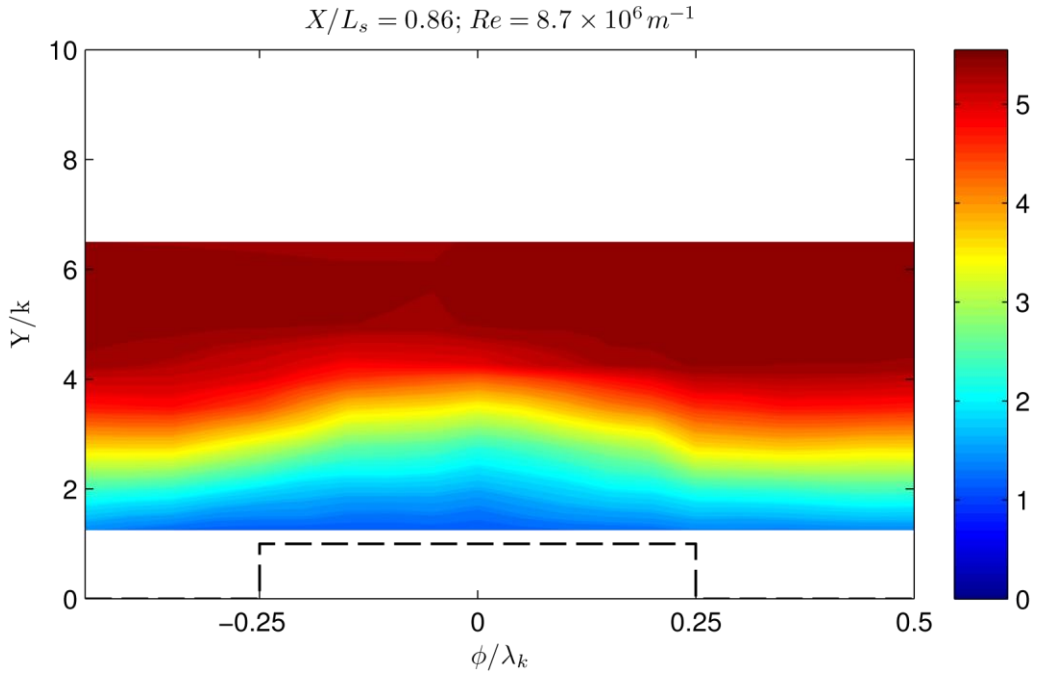

Figure A-8. Enlarged version of Figure 4-3(b). Phase-locked averaged contours of Mach number at X/L_s = 0.86 and Re = 8.7 × 10^6 m^{-1}. Dashed lines indicate the projection of a roughness element into the measurement plane.

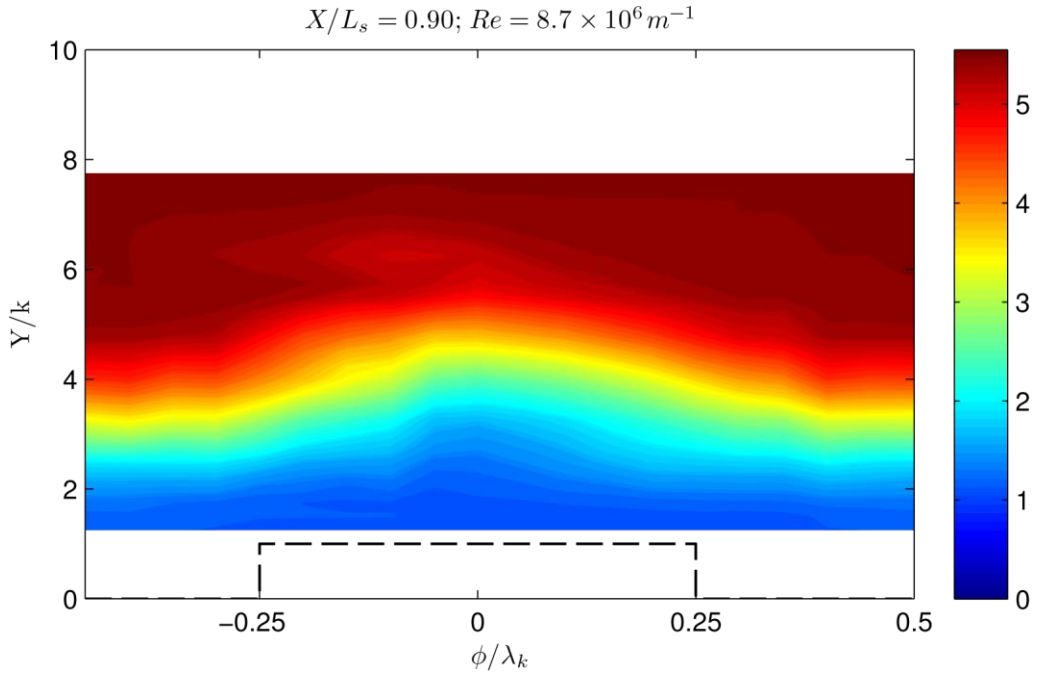

Figure A-9. Enlarged version of Figure 4-3(c). Phase-locked averaged contours of Mach number at X/L_s = 0.90 and Re = 8.7 × 10^6 m^{-1}. Dashed lines indicate the projection of a roughness element into the measurement plane.

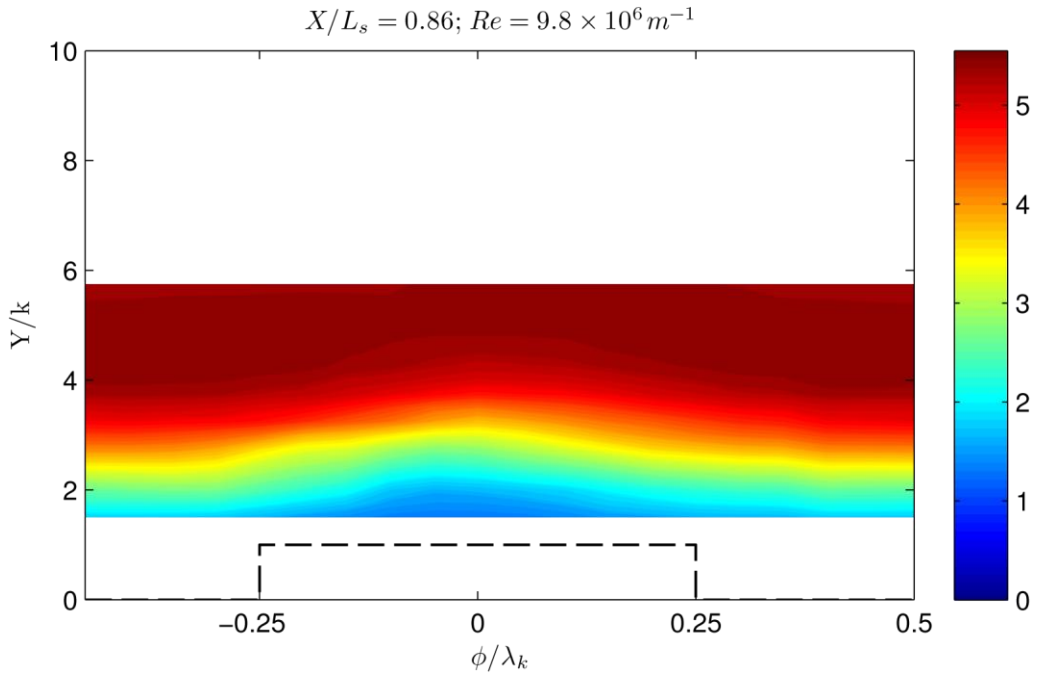

Figure A-10. Enlarged version of Figure 4-3(d). Phase-locked averaged contours of Mach number at $X/L_s = 0.86$ and $Re = 9.8 \times 10^6$ m^{-1}. Dashed lines indicate the projection of a roughness element into the measurement plane.

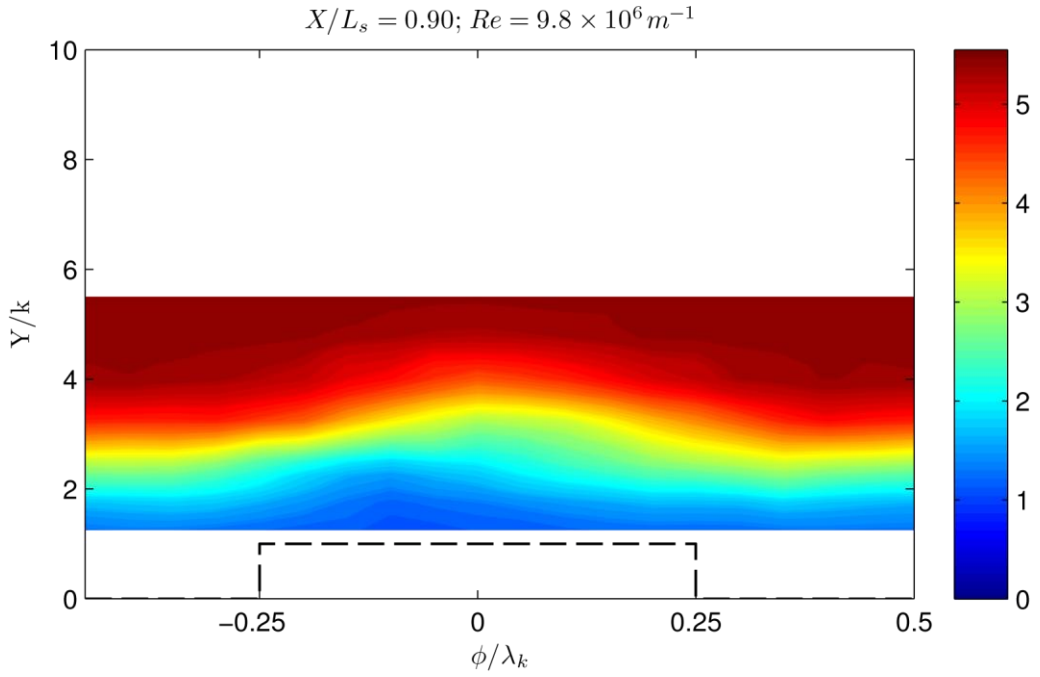

Figure A-11. Enlarged version of Figure 4-3(e). Phase-locked averaged contours of Mach number at $X/L_s = 0.90$ and $Re = 9.8 \times 10^6$ m^{-1}. Dashed lines indicate the projection of a roughness element into the measurement plane.

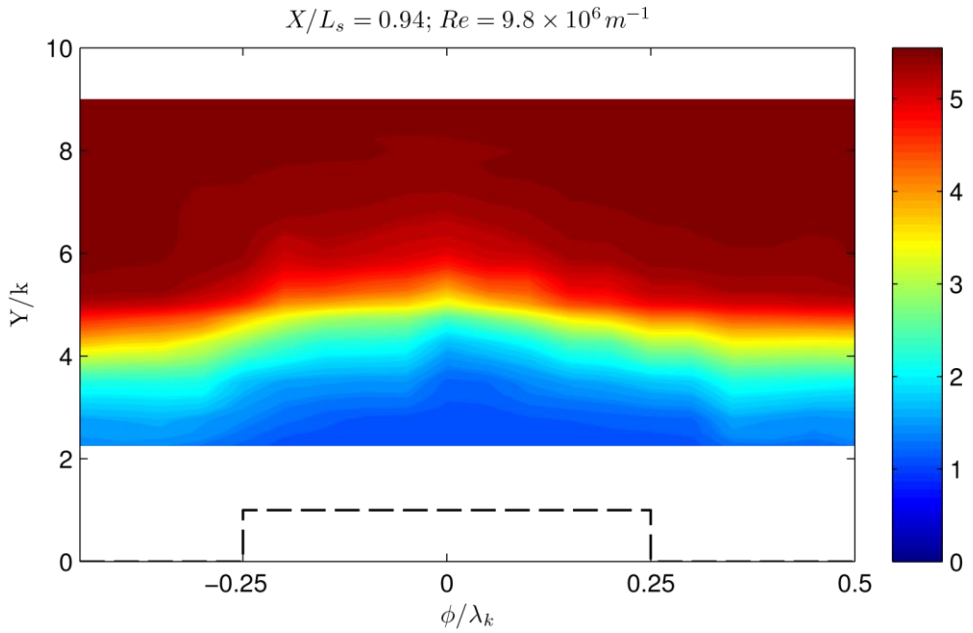

Figure A-12. Enlarged version of Figure 4-3(f). Phase-locked averaged contours of Mach number at X/L_s = 0.94 and Re = 9.8 × 10^6 m^{-1}. Dashed lines indicate the projection of a roughness element into the measurement plane.

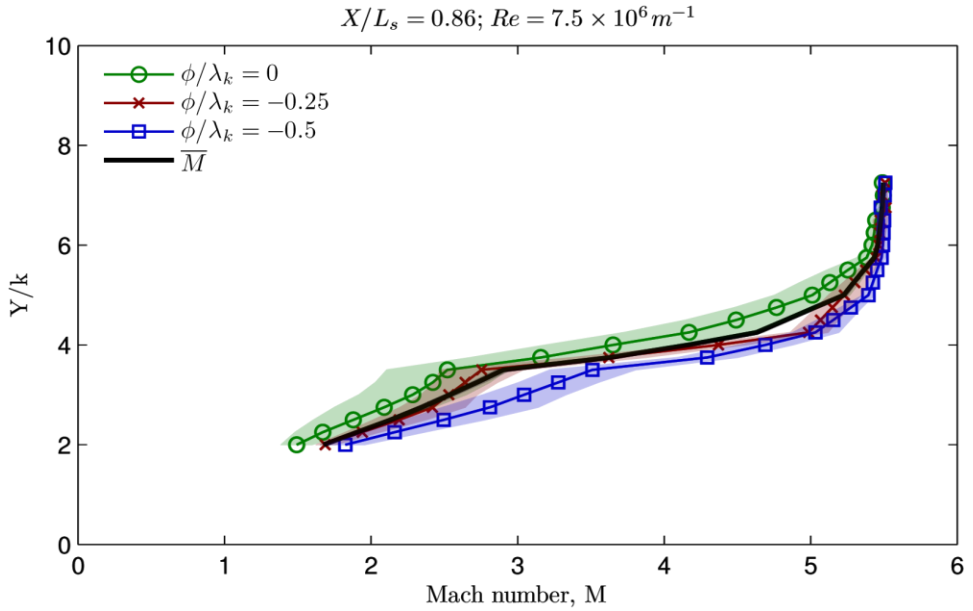

Figure A-13. Enlarged version of Figure 4-4(a). Wall-normal Mach number profiles at X/L_s = 0.86 and Re = 7.5 × 10^6 m^{-1}. Phase-locked averaged profiles are shown along the roughness element centerline $(\phi / \lambda_k = 0)$, at the roughness element edge $(\phi / \lambda_k = -0.25)$, and between the roughness elements $(\phi / \lambda_k = -0.5)$. The solid black line indicates the azimuthal average Mach number profile. The shaded regions indicate the standard error of the phase-locked mean.

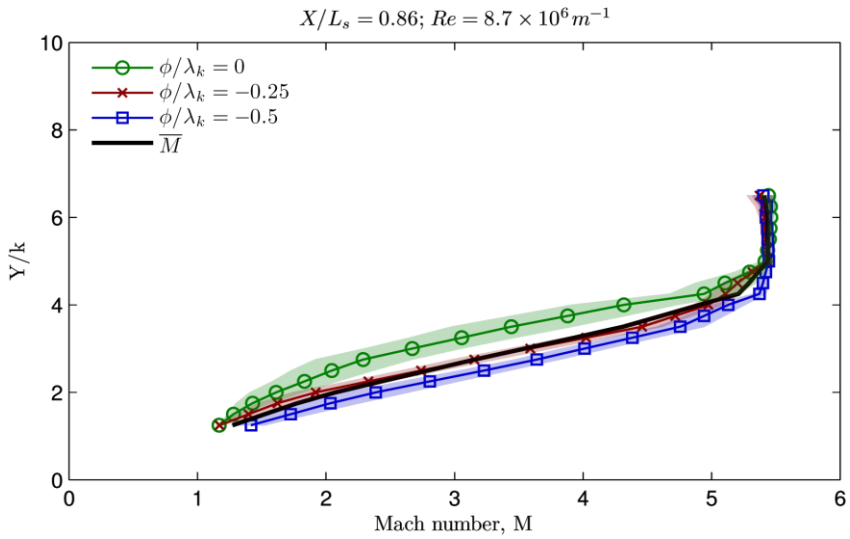

Figure A-14. Enlarged version of Figure 4-4(b). Wall-normal Mach number profiles at X/L_s = 0.86 and Re = 8.7 × 10^6 m^{-1}. Phase-locked averaged profiles are shown along the roughness element centerline $(\phi / \lambda_k = 0)$, at the roughness element edge $(\phi / \lambda_k = -0.25)$, and between the roughness elements $(\phi / \lambda_k = -0.5)$. The solid black line indicates the azimuthal average Mach number profile. The shaded regions indicate the standard error of the phase-locked mean.

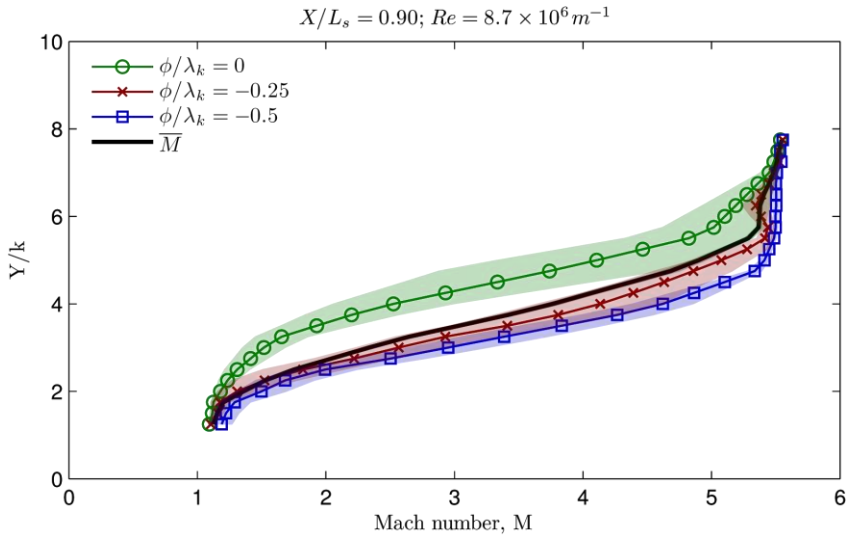

Figure A-15. Enlarged version of Figure 4-4(c). Wall-normal Mach number profiles at X/L_s = 0.90 and Re = 8.7 × 10^6 m^{-1}. Phase-locked averaged profiles are shown along the roughness element centerline $(\phi / \lambda_k = 0)$, at the roughness element edge $(\phi / \lambda_k = -0.25)$, and between the roughness elements $(\phi / \lambda_k = -0.5)$. The solid black line indicates the azimuthal average Mach number profile. The shaded regions indicate the standard error of the phase-locked mean.

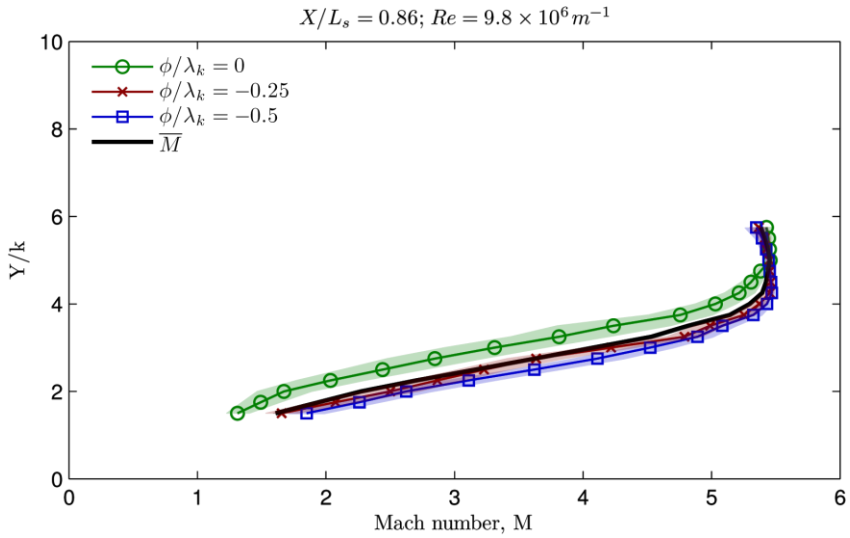

Figure A-16. Enlarged version of Figure 4-4(d). Wall-normal Mach number profiles at $X/L_s = 0.86$ and $Re = 9.8 \times 10^6$ m^{-1}. Phase-locked averaged profiles are shown along the roughness element centerline $(\phi / \lambda_k = 0)$, at the roughness element edge $(\phi / \lambda_k = -0.25)$, and between the roughness elements $(\phi / \lambda_k = -0.5)$. The solid black line indicates the azimuthal average Mach number profile. The shaded regions indicate the standard error of the phase-locked mean.

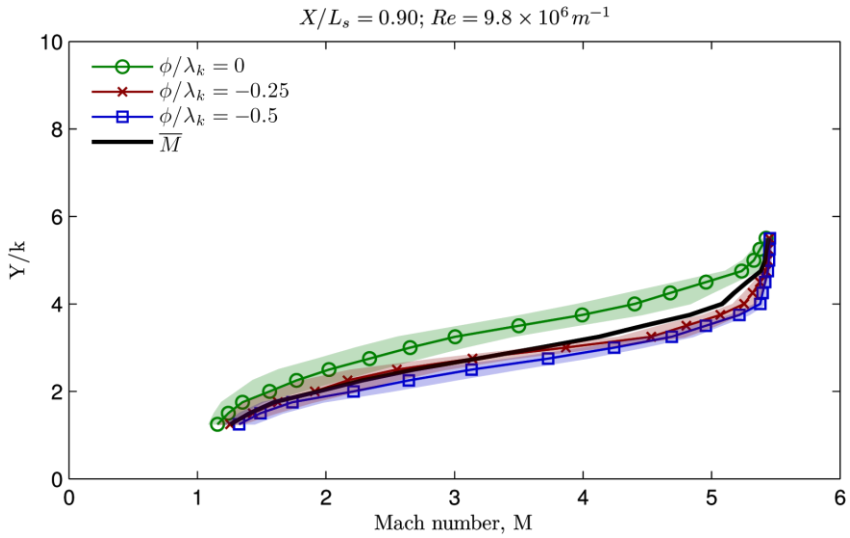

Figure A-17. Enlarged version of Figure 4-4(e). Wall-normal Mach number profiles at $X/L_s = 0.90$ and $Re = 9.8 \times 10^6$ m^{-1}. Phase-locked averaged profiles are shown along the roughness element centerline $(\phi / \lambda_k = 0)$, at the roughness element edge $(\phi / \lambda_k = -0.25)$, and between the roughness elements $(\phi / \lambda_k = -0.5)$. The solid black line indicates the azimuthal average Mach number profile. The shaded regions indicate the standard error of the phase-locked mean.

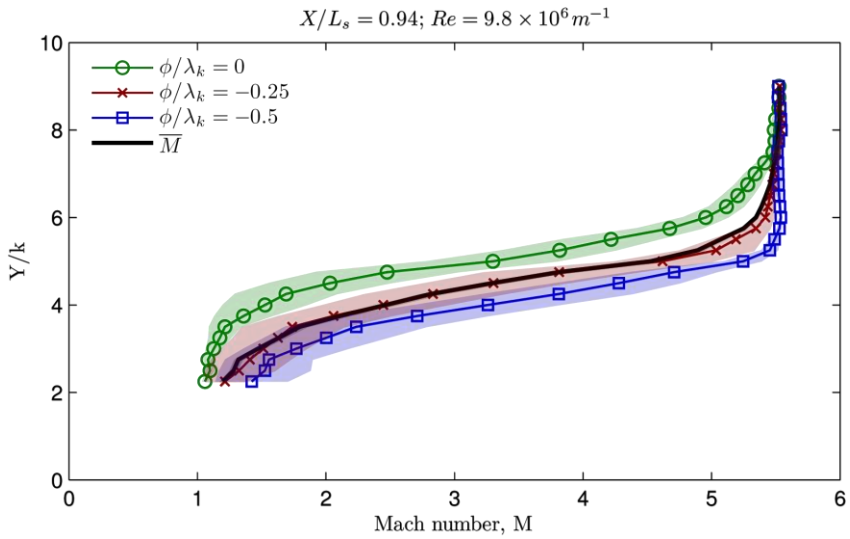

Figure A-18. Enlarged version of Figure 4-4(f). Wall-normal Mach number profiles at X/L_s = 0.94 and Re = 9.8 × 10^6 m^{-1}. Phase-locked averaged profiles are shown along the roughness element centerline $(\phi / \lambda_k = 0)$, at the roughness element edge $(\phi / \lambda_k = -0.25)$, and between the roughness elements $(\phi / \lambda_k = -0.5)$. The solid black line indicates the azimuthal average Mach number profile. The shaded regions indicate the standard error of the phase-locked mean.

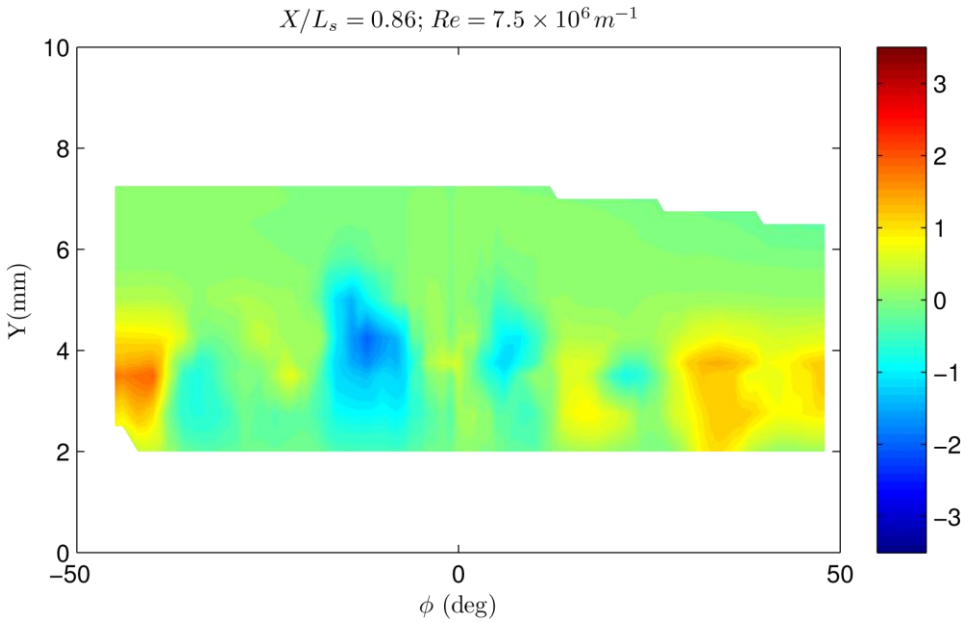

Figure A-19. Enlarged version of Figure 4-5(a). Contours of steady disturbance M' at X/L_s = 0.86 and Re = 7.5 × 10^6 m^{-1}.

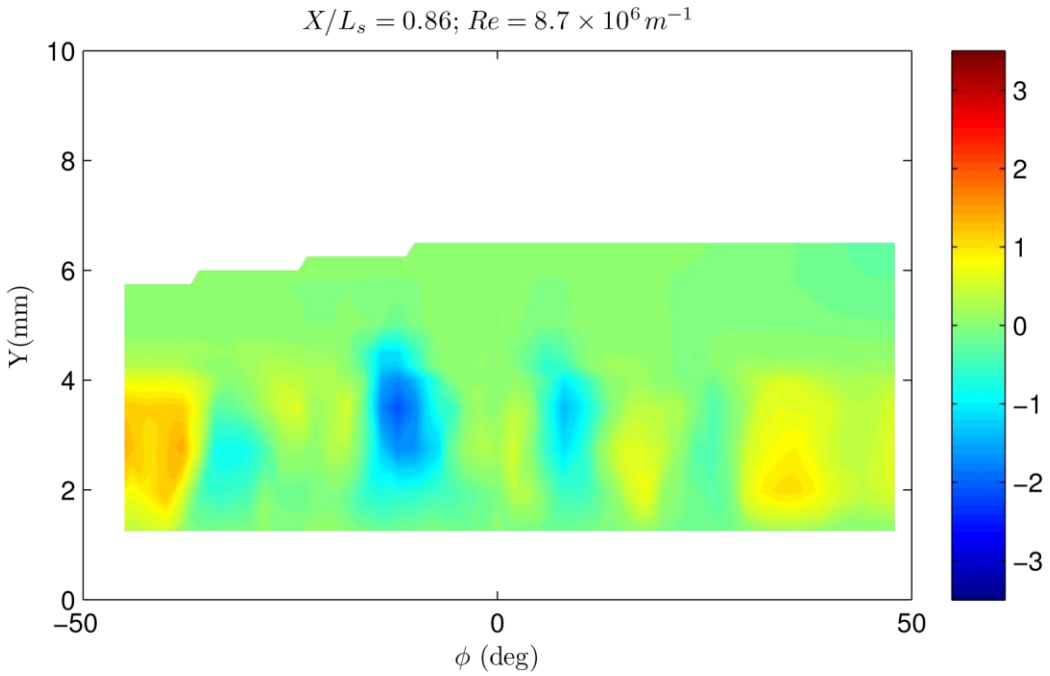

Figure A-20. Enlarged version of Figure 4-5(b). Contours of steady disturbance M' at $X/L_s = 0.86$ and $Re = 8.7 \times 10^6$ m^{-1}.

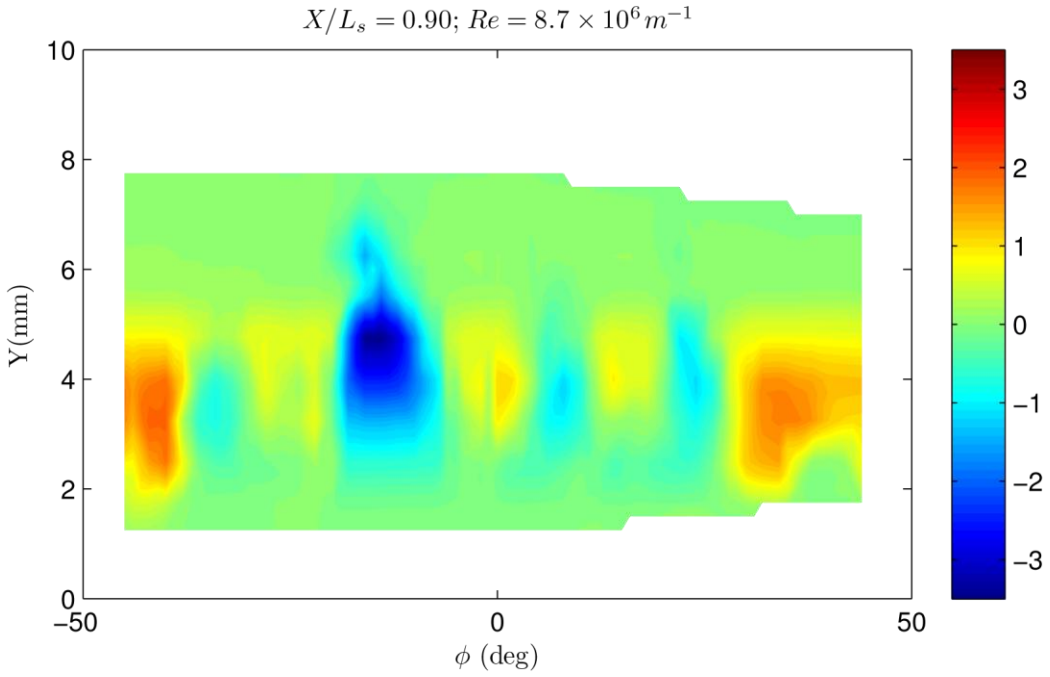

Figure A-21. Enlarged version of Figure 4-5(c). Contours of steady disturbance M' at $X/L_s = 0.90$ and $Re = 8.7 \times 10^6$ m^{-1}.

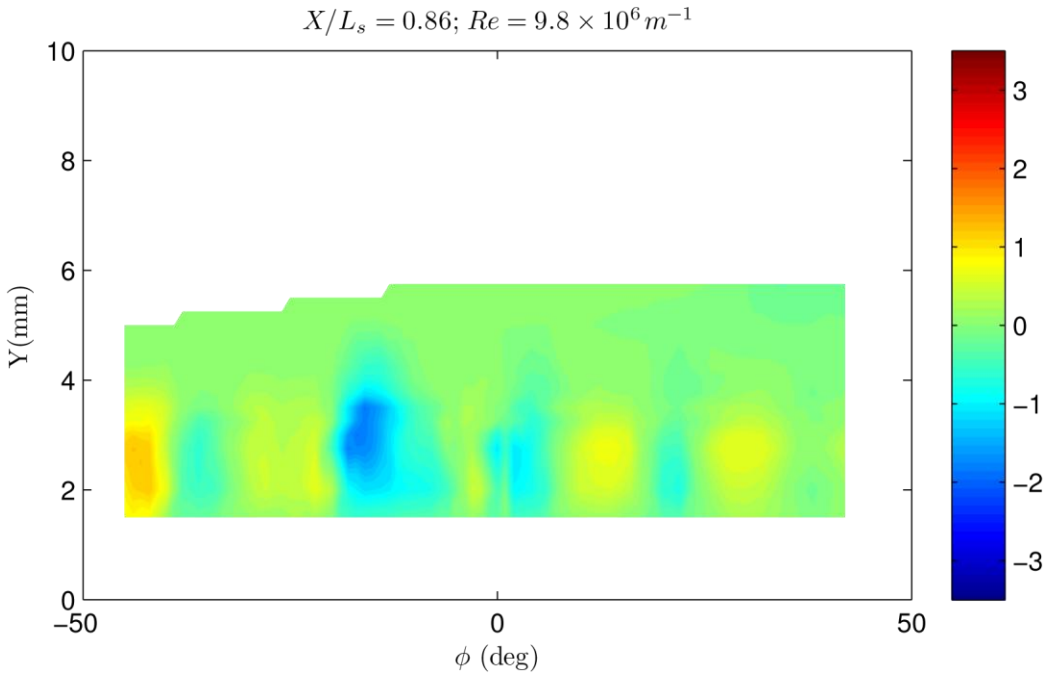

Figure A-22. Enlarged version of Figure 4-5(d). Contours of steady disturbance M' at $X/L_s = 0.86$ and $Re = 9.8 \times 10^6$ m^{-1}.

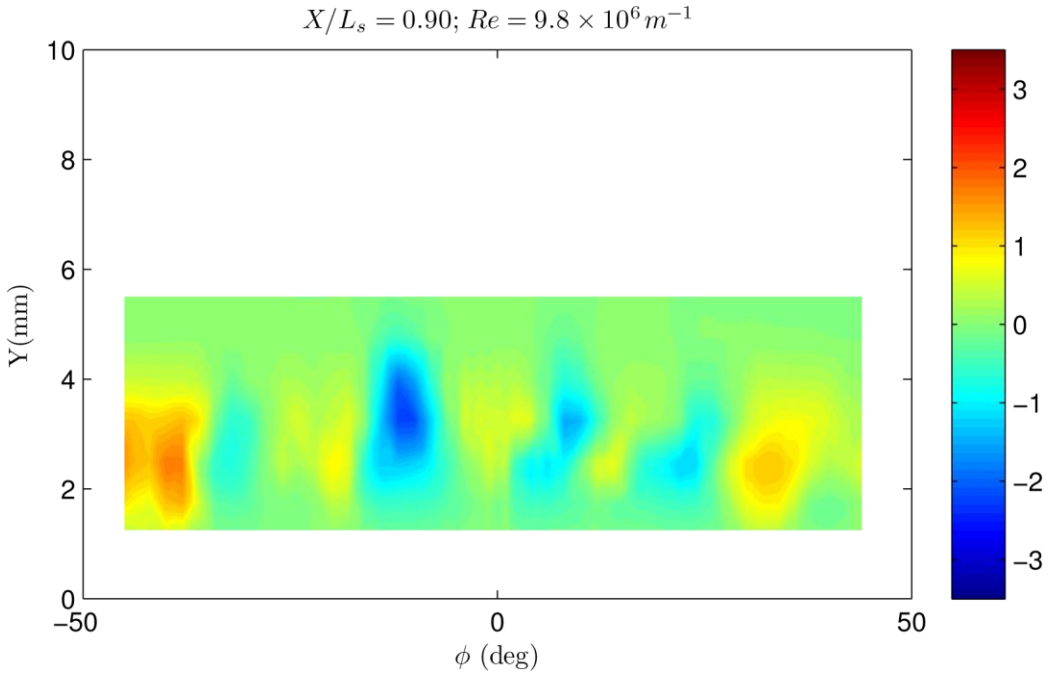

Figure A-23. Enlarged version of Figure 4-5(e). Contours of steady disturbance M' at $X/L_s = 0.90$ and $Re = 9.8 \times 10^6$ m^{-1}.

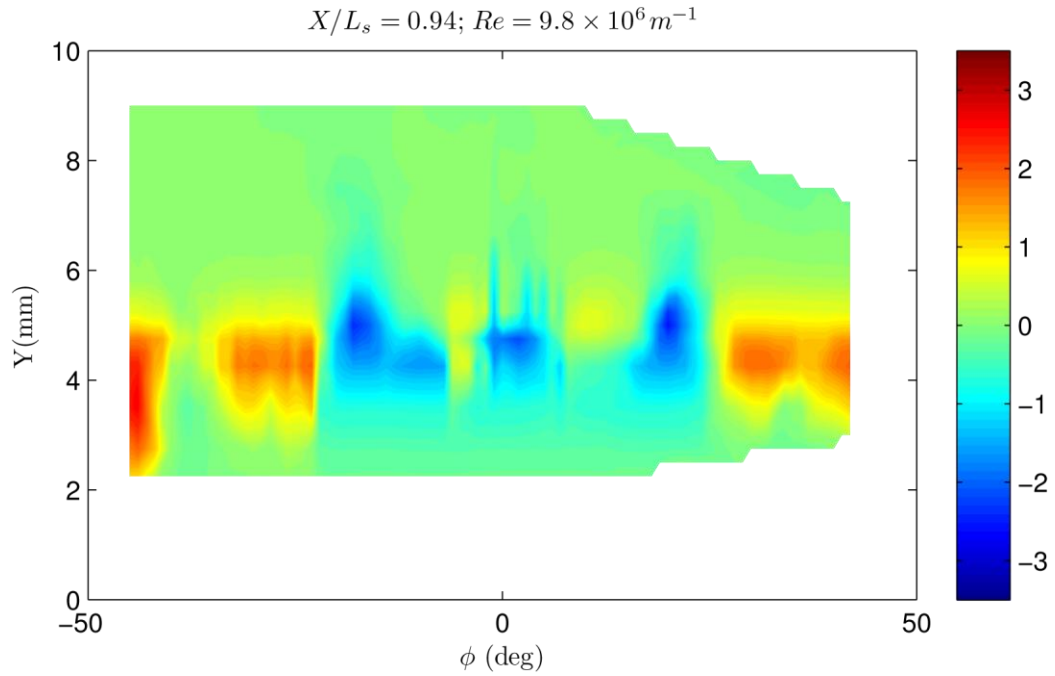

Figure A-24. Enlarged version of Figure 4-5(f). Contours of steady disturbance M' at $X/L_s = 0.94$ and $Re = 9.8 \times 10^6$ m^{-1}.

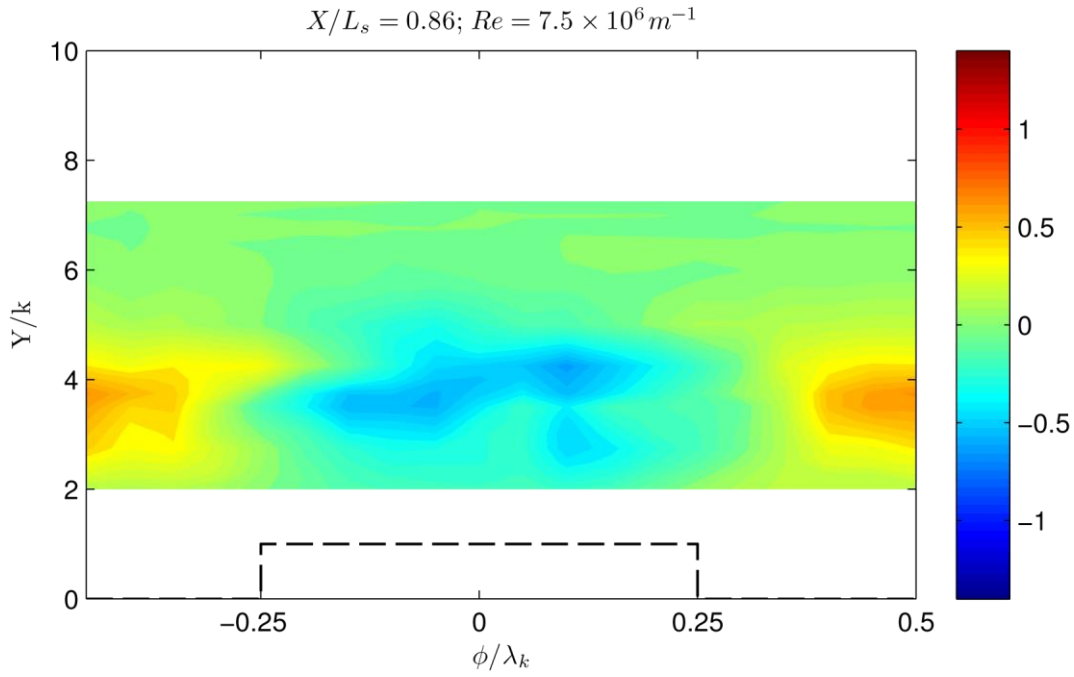

Figure A-25. Enlarged version of Figure 4-6(a). Phase-locked averaged contours of steady disturbance M' at $X/L_s = 0.86$ and $Re = 7.5 \times 10^6$ m^{-1}. Dashed lines indicate the projection of a roughness element into the measurement plane.

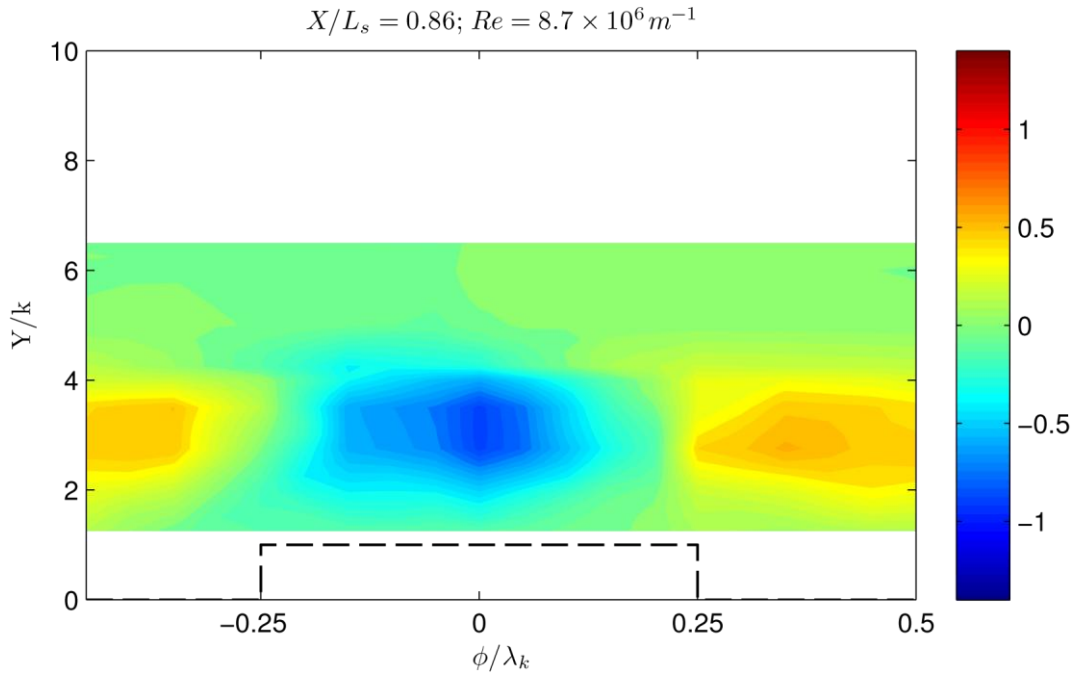

Figure A-26. Enlarged version of Figure 4-6(b). Phase-locked averaged contours of steady disturbance M' at $X/L_s = 0.86$ and $Re = 8.7 \times 10^6$ m^{-1}. Dashed lines indicate the projection of a roughness element into the measurement plane.

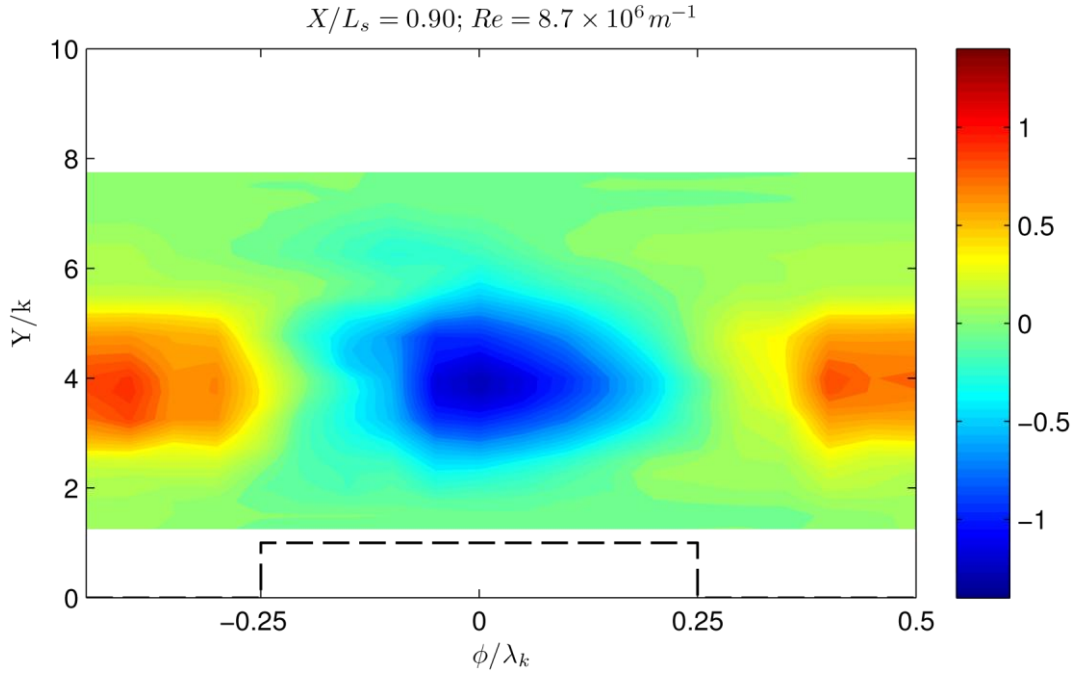

Figure A-27. Enlarged version of Figure 4-6(c). Phase-locked averaged contours of steady disturbance M' at $X/L_s = 0.90$ and $Re = 8.7 \times 10^6$ m^{-1}. Dashed lines indicate the projection of a roughness element into the measurement plane.

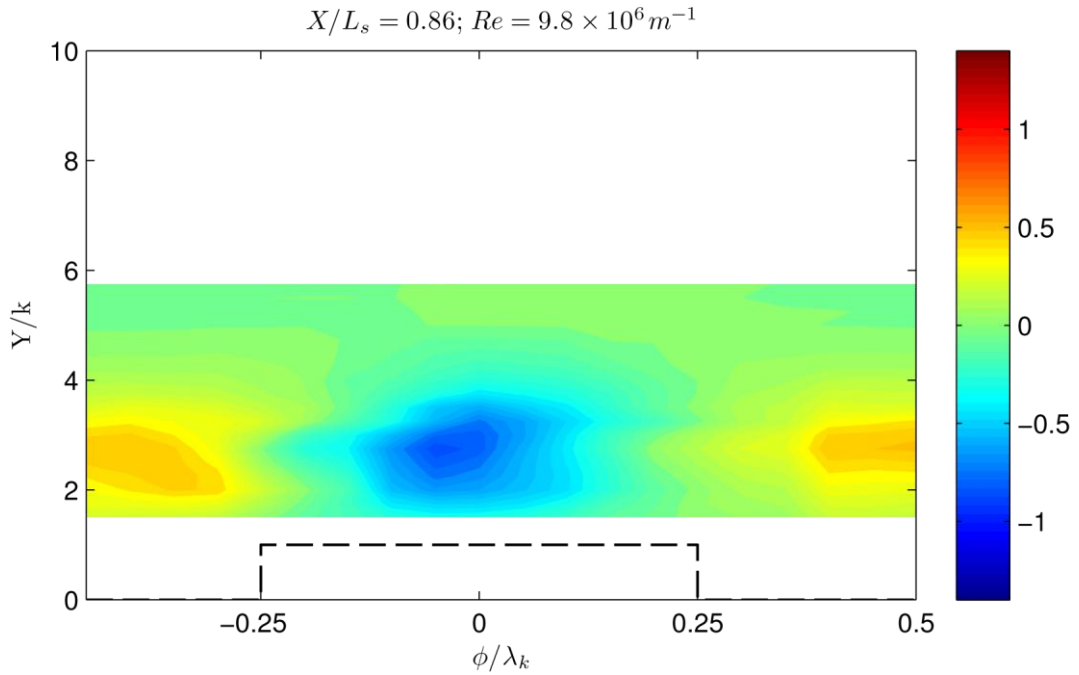

Figure A-28. Enlarged version of Figure 4-6(d). Phase-locked averaged contours of steady disturbance M' at $X/L_s = 0.86$ and $Re = 9.8 \times 10^6$ m^{-1}. Dashed lines indicate the projection of a roughness element into the measurement plane.

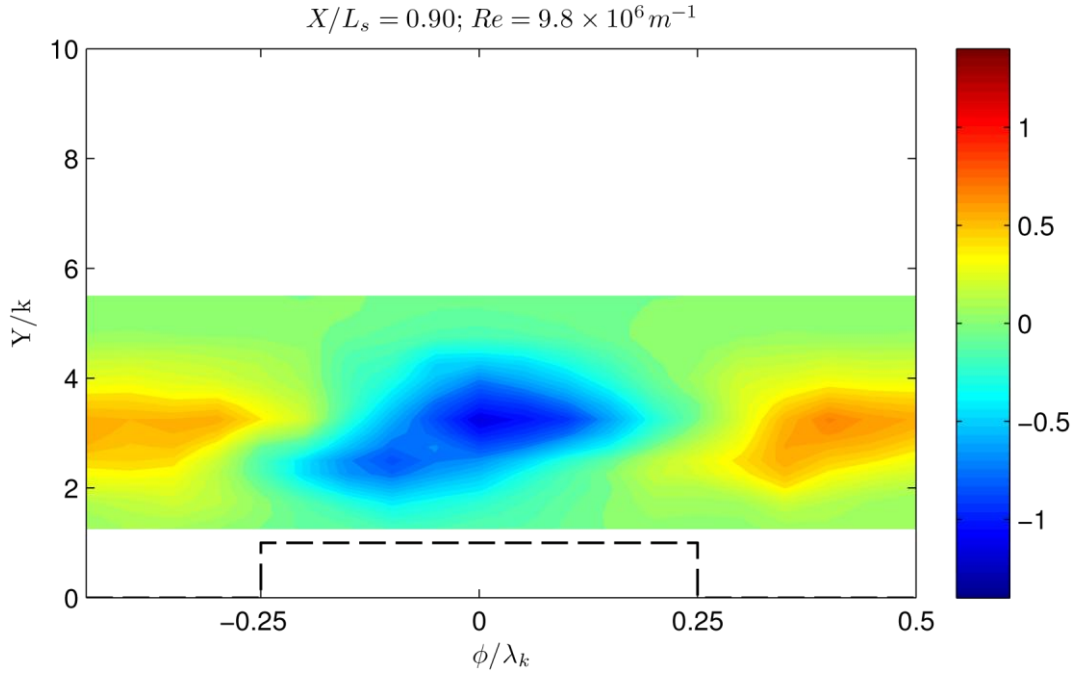

Figure A-29. Enlarged version of Figure 4-6(e). Phase-locked averaged contours of steady disturbance M' at $X/L_s = 0.90$ and $Re = 9.8 \times 10^6$ m^{-1}. Dashed lines indicate the projection of a roughness element into the measurement plane.

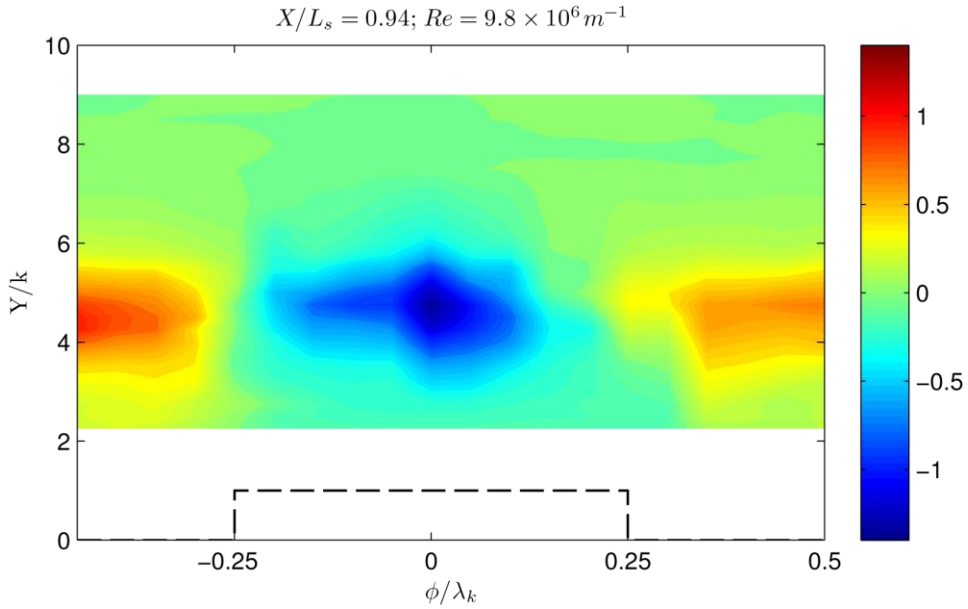

Figure A-30. Enlarged version of Figure 4-6(f). Phase-locked averaged contours of steady disturbance M' at $X/L_s = 0.94$ and $Re = 9.8 \times 10^6$ m^{-1}. Dashed lines indicate the projection of a roughness element into the measurement plane.

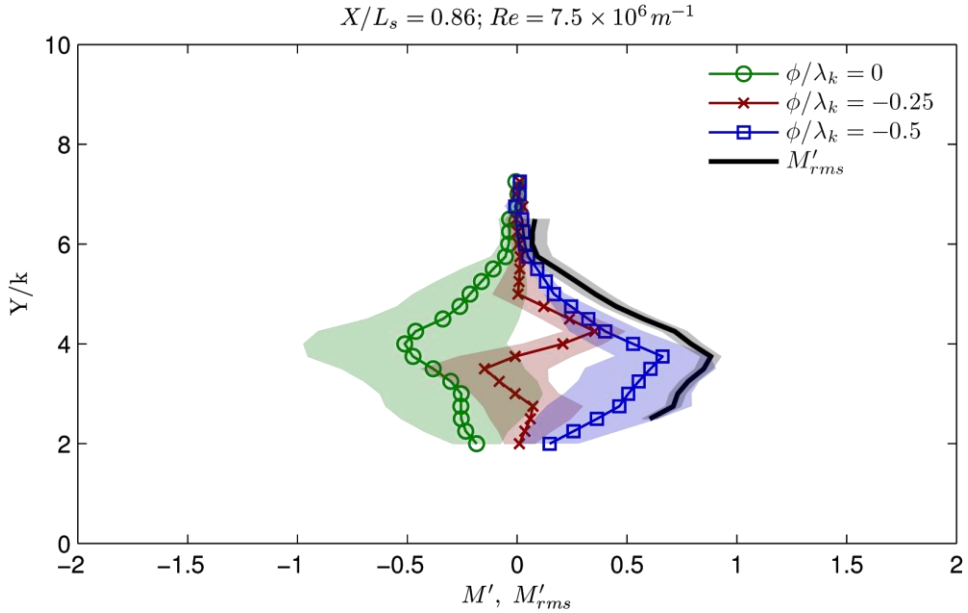

Figure A-31. Enlarged version of Figure 4-7(a). Wall-normal steady disturbance M' profiles at $X/L_s = 0.86$ and $Re = 7.5 \times 10^6$ m^{-1}. Phase-locked averaged profiles are shown along the roughness element centerline $(\phi / \lambda_k = 0)$, at the roughness element edge $(\phi / \lambda_k = -0.25)$, and between the roughness elements $(\phi / \lambda_k = -0.5)$. The solid black line indicates the full-span azimuthal root-mean-square steady disturbance profile. The shaded regions indicate the standard error of the phase-locked mean.

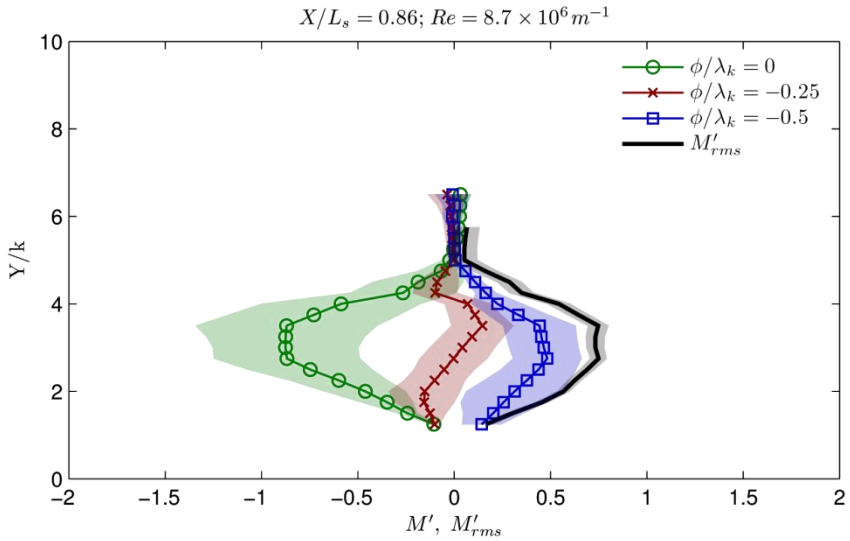

Figure A-32. Enlarged version of Figure 4-7(b). Wall-normal steady disturbance M' profiles at X/L_s = 0.86 and Re = 8.7 × 10^6 m^{-1}. Phase-locked averaged profiles are shown along the roughness element centerline $(\phi / \lambda_k = 0)$, at the roughness element edge $(\phi / \lambda_k = -0.25)$, and between the roughness elements $(\phi / \lambda_k = -0.5)$. The solid black line indicates the full-span azimuthal root-mean-square steady disturbance profile. The shaded regions indicate the standard error of the phase-locked mean.

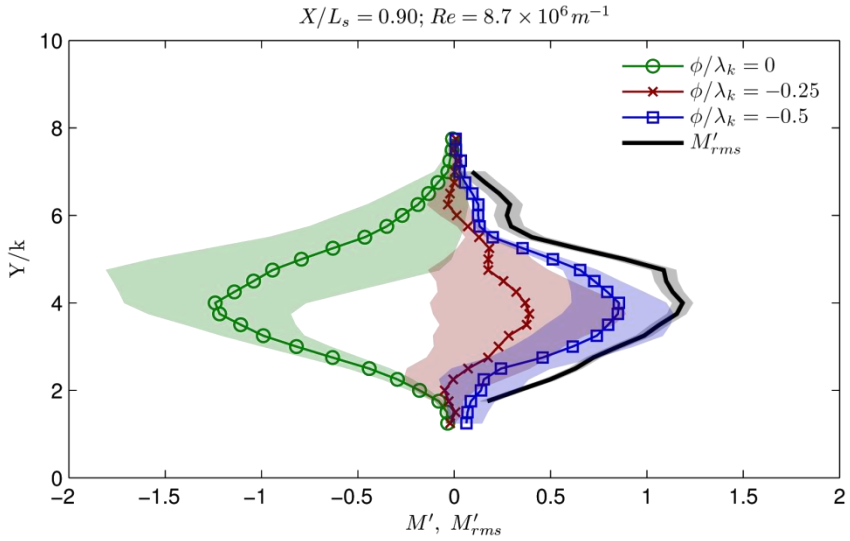

Figure A-33. Enlarged version of Figure 4-7(c). Wall-normal steady disturbance M' profiles at X/L_s = 0.90 and Re = 8.7 × 10^6 m^{-1}. Phase-locked averaged profiles are shown along the roughness element centerline $(\phi / \lambda_k = 0)$, at the roughness element edge $(\phi / \lambda_k = -0.25)$, and between the roughness elements $(\phi / \lambda_k = -0.5)$. The solid black line indicates the full-span azimuthal root-mean-square steady disturbance profile. The shaded regions indicate the standard error of the phase-locked mean.

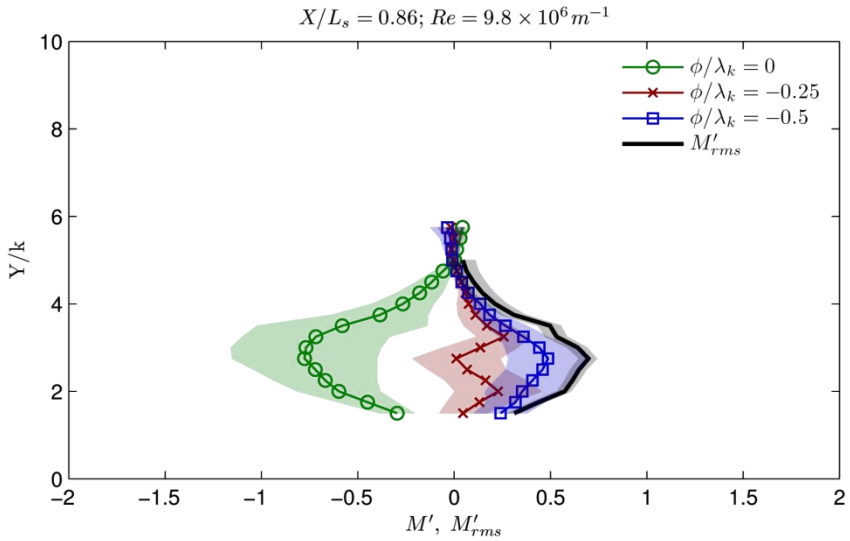

Figure A-34. Enlarged version of Figure 4-7(d). Wall-normal steady disturbance M' profiles at X/L_s = 0.86 and Re = 9.8 × 10^6 m^{-1}. Phase-locked averaged profiles are shown along the roughness element centerline $(\phi / \lambda_k = 0)$, at the roughness element edge $(\phi / \lambda_k = -0.25)$, and between the roughness elements $(\phi / \lambda_k = -0.5)$. The solid black line indicates the full-span azimuthal root-mean-square steady disturbance profile. The shaded regions indicate the standard error of the phase-locked mean.

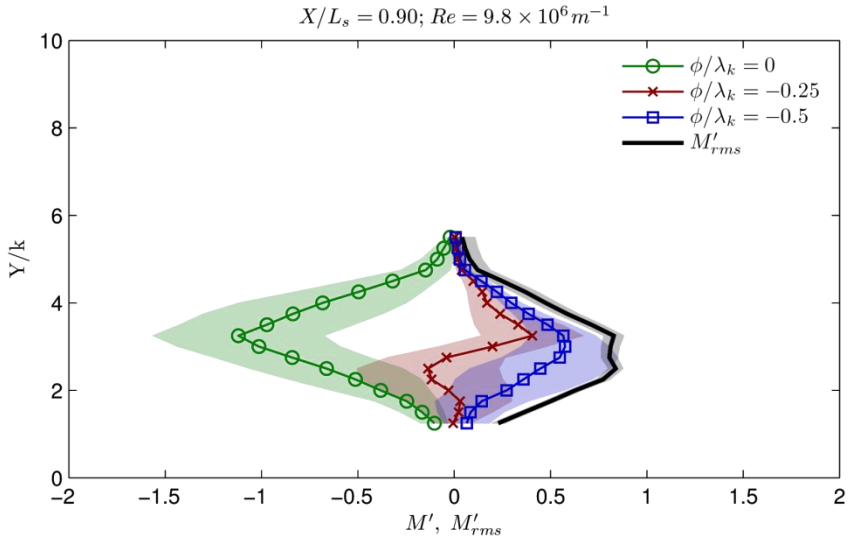

Figure A-35. Enlarged version of Figure 4-7(e). Wall-normal steady disturbance M' profiles at X/L_s = 0.90 and Re = 9.8 × 10^6 m^{-1}. Phase-locked averaged profiles are shown along the roughness element centerline $(\phi / \lambda_k = 0)$, at the roughness element edge $(\phi / \lambda_k = -0.25)$, and between the roughness elements $(\phi / \lambda_k = -0.5)$. The solid black line indicates the full-span azimuthal root-mean-square steady disturbance profile. The shaded regions indicate the standard error of the phase-locked mean.

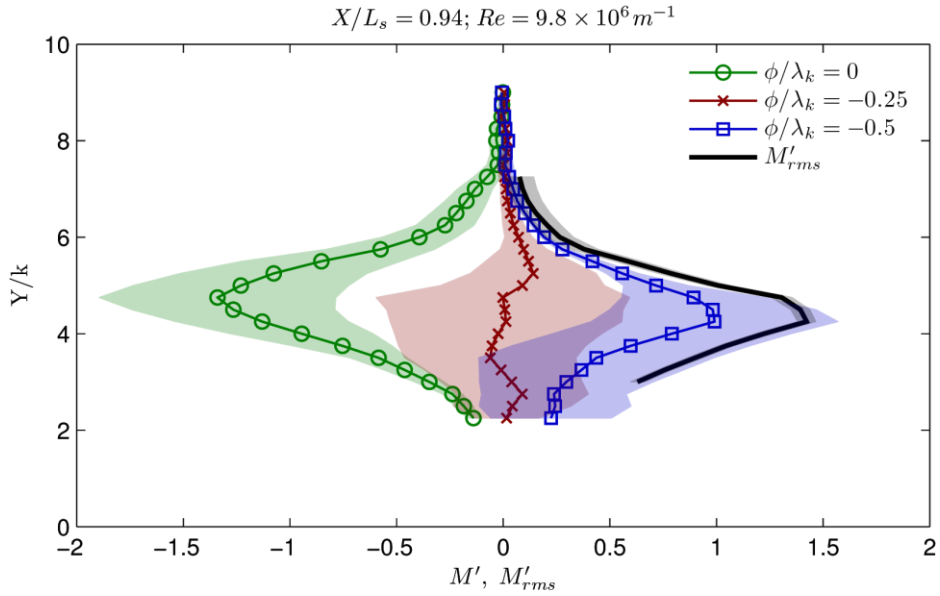

Figure A-36. Enlarged version of Figure 4-7(f). Wall-normal steady disturbance M' profiles at $X/L_s = 0.94$ and $Re = 9.8 \times 10^6$ m^{-1}. Phase-locked averaged profiles are shown along the roughness element centerline $(\phi / \lambda_k = 0)$, at the roughness element edge $(\phi / \lambda_k = -0.25)$, and between the roughness elements $(\phi / \lambda_k = -0.5)$. The solid black line indicates the full-span azimuthal root-mean-square steady disturbance profile. The shaded regions indicate the standard error of the phase-locked mean.

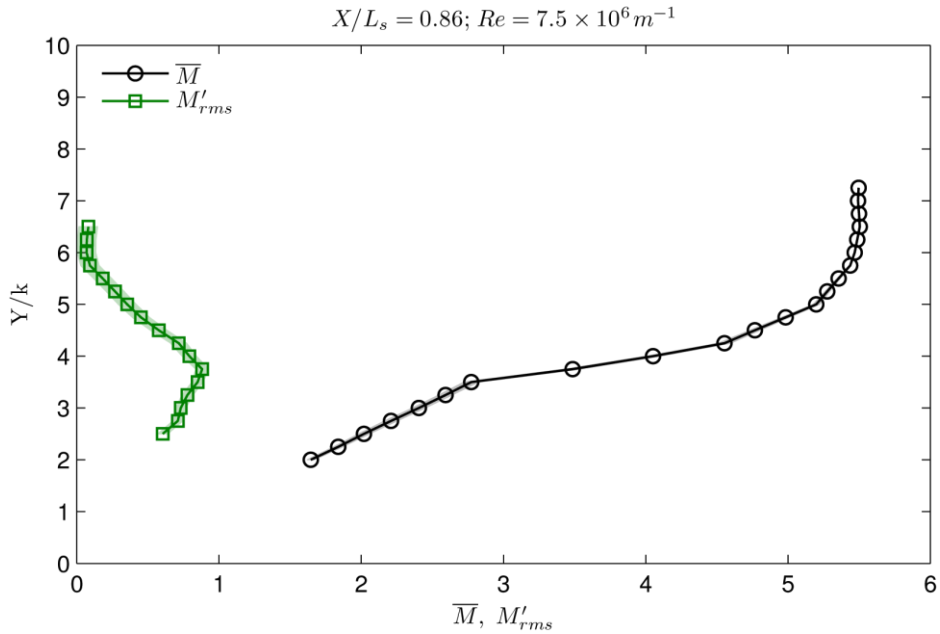

Figure A-37. Enlarged version of Figure 4-8(a). Wall-normal profiles of $\overline{M}$ and M'_{rms} at $X/L_s = 0.86$ and $Re = 7.5 \times 10^6$ m^{-1}. The shaded region indicates the extent of the uncertainty.

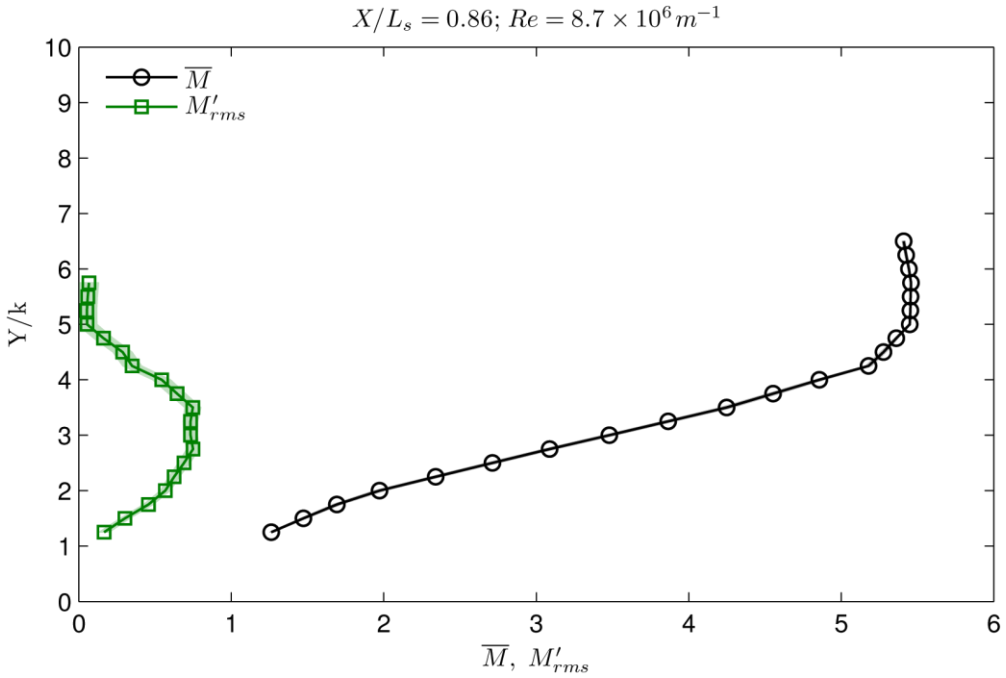

Figure A-38. Enlarged version of Figure 4-8(b). Wall-normal profiles of $\overline{M}$ and M'_{rms} at X/L_s = 0.86 and Re = 8.7 × 10^6 m^{-1}. The shaded region indicates the extent of the uncertainty.

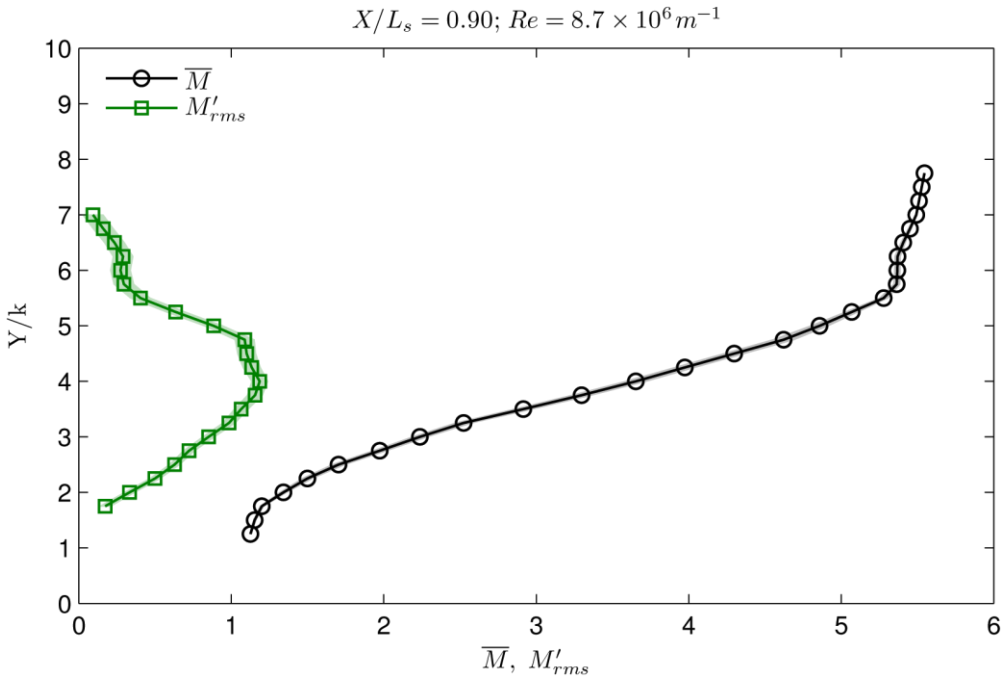

Figure A-39. Enlarged version of Figure 4-8(c). Wall-normal profiles of $\overline{M}$ and M'_{rms} at X/L_s = 0.90 and Re = 8.7 × 10^6 m^{-1}. The shaded region indicates the extent of the uncertainty.

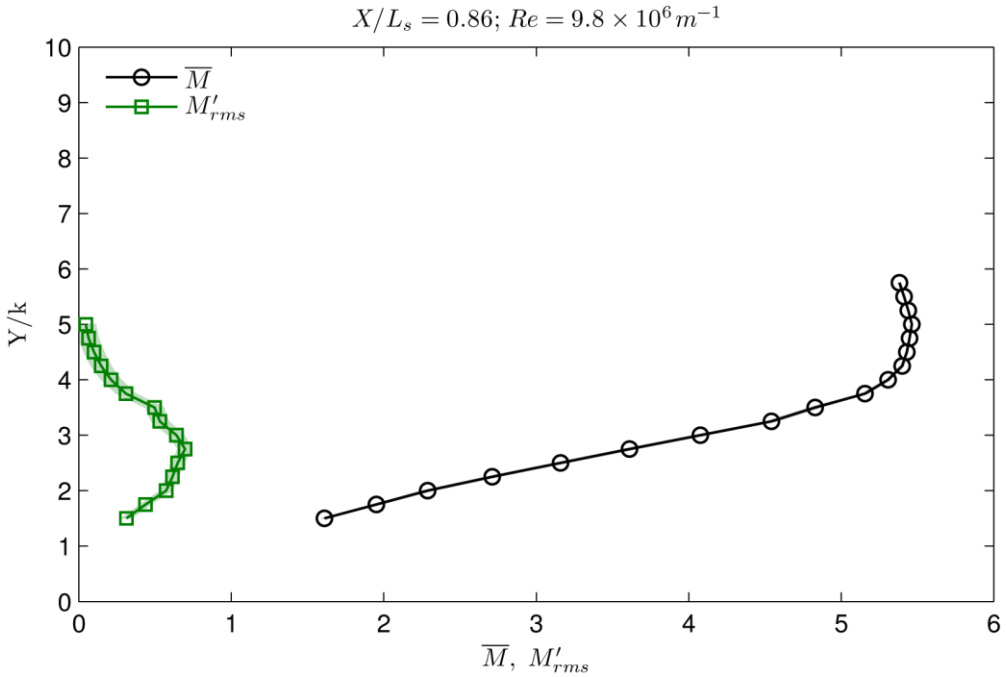

Figure A-40. Enlarged version of Figure 4-8(d). Wall-normal profiles of $\overline{M}$ and M'_{rms} at X/L_s = 0.86 and Re = 9.8 × 10^6 m^{-1}. The shaded region indicates the extent of the uncertainty.

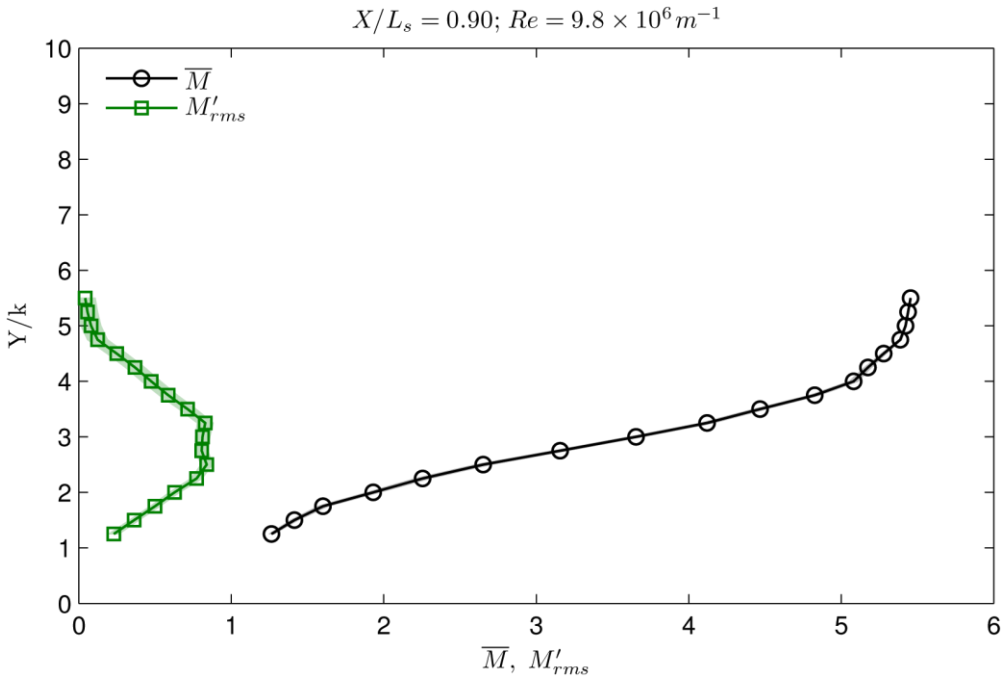

Figure A-41. Enlarged version of Figure 4-8(e). Wall-normal profiles of $\overline{M}$ and M'_{rms} at X/L_s = 0.90 and Re = 9.8 × 10^6 m^{-1}. The shaded region indicates the extent of the uncertainty.

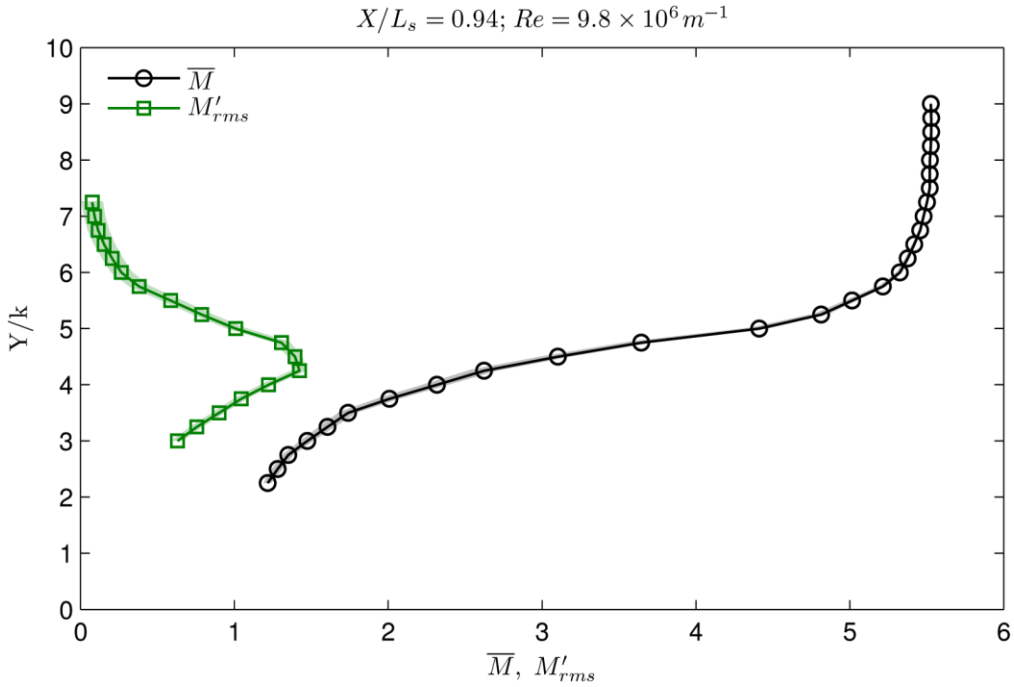

Figure A-42. Enlarged version of Figure 4-8(f). Wall-normal profiles of $\overline{M}$ and M'_{rms} at $X/L_s = 0.94$ and $Re = 9.8 \times 10^6$ m^{-1}. The shaded region indicates the extent of the uncertainty.

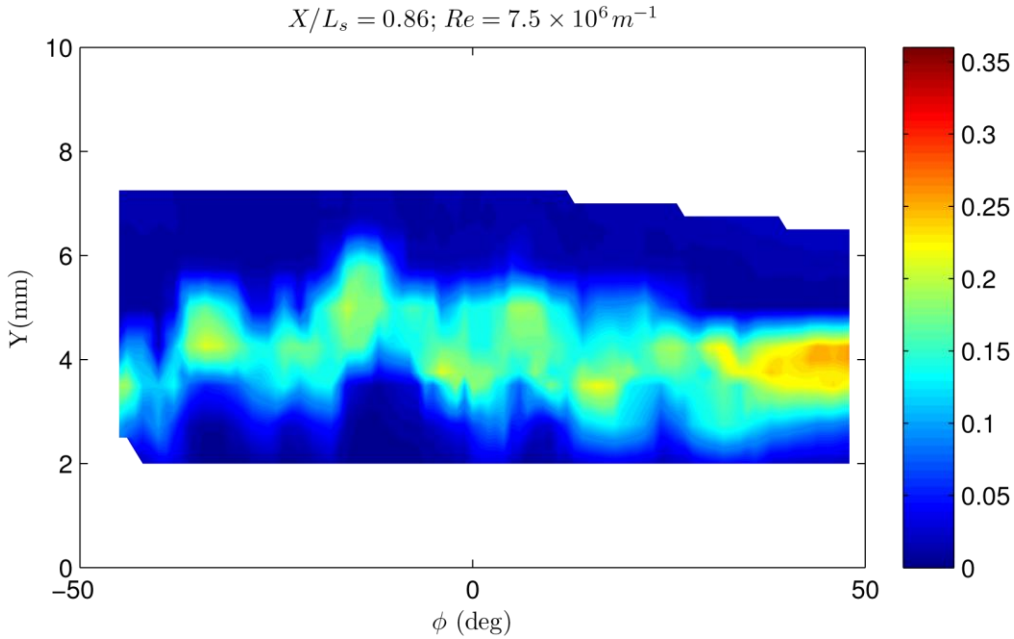

Figure A-43. Enlarged version of Figure 4-9(a). Contours of unsteady total pressure $p_{0,rms} / p_{0,edge}$ at $X/L_s = 0.86$ and $Re = 7.5 \times 10^6$ m^{-1}.

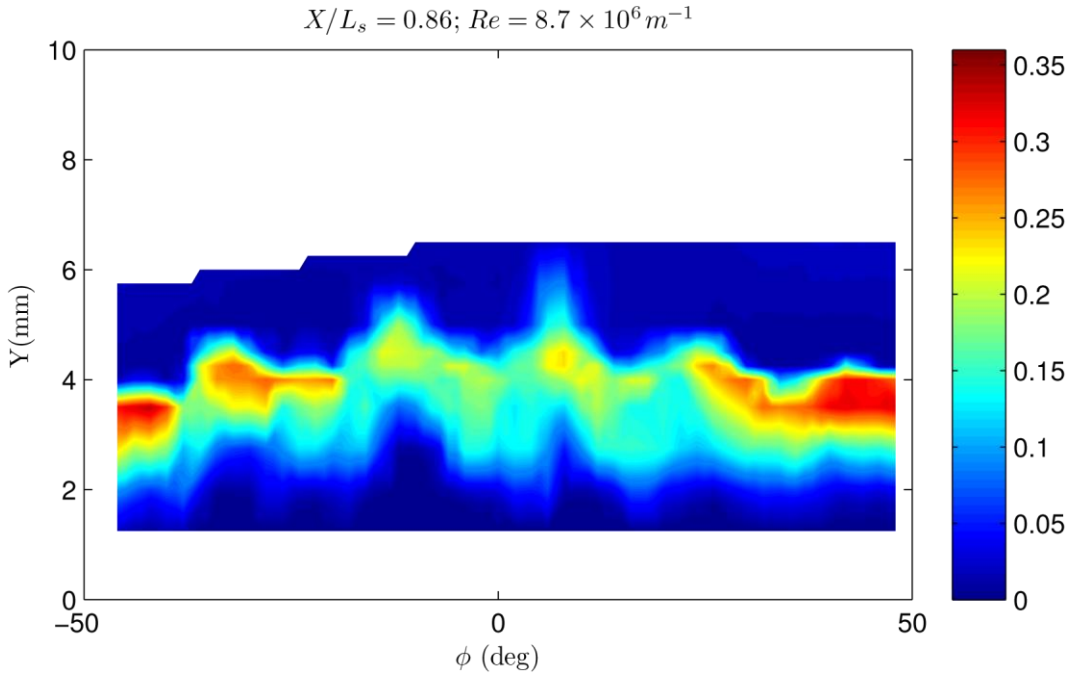

Figure A-44. Enlarged version of Figure 4-9(b). Contours of unsteady total pressure $p_{0,rms} / p_{0,edge}$ at $X/L_s = 0.86$ and $Re = 8.7 \times 10^6$ m^{-1}.

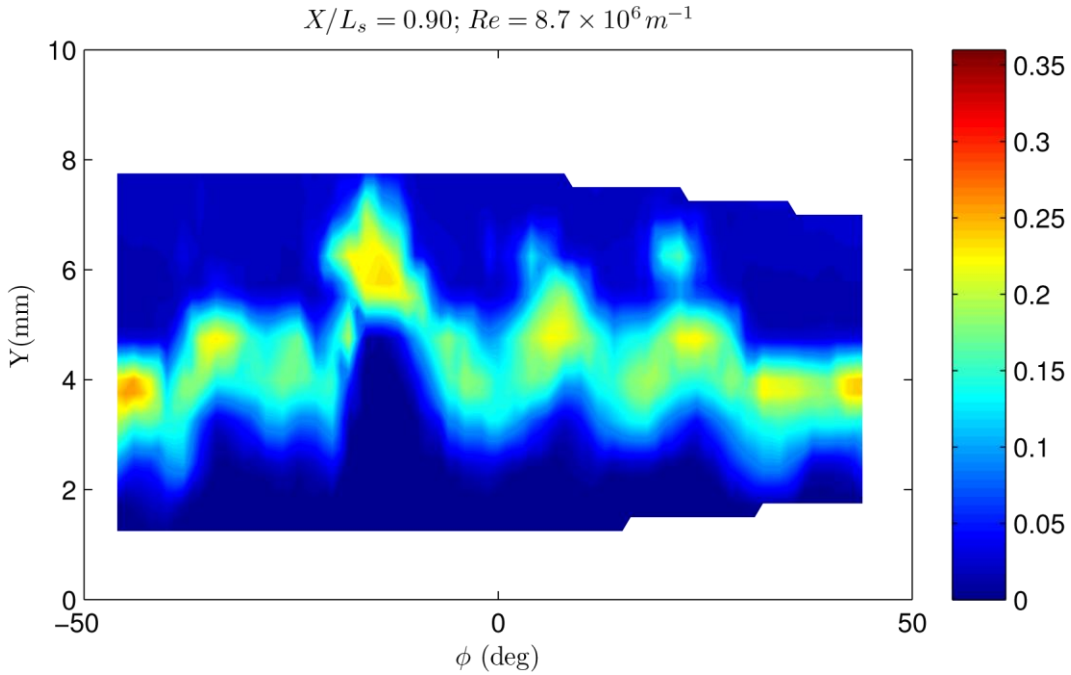

Figure A-45. Enlarged version of Figure 4-9(c). Contours of unsteady total pressure $p_{0,rms} / p_{0,edge}$ at $X/L_s = 0.90$ and $Re = 8.7 \times 10^6$ m^{-1}.

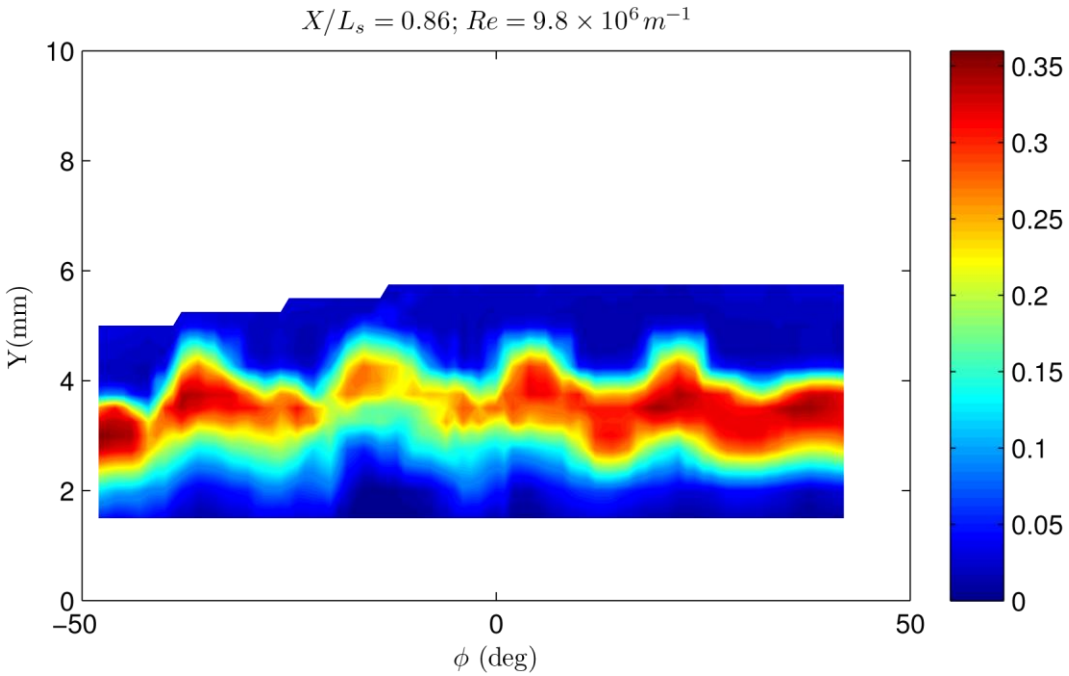

Figure A-46. Enlarged version of Figure 4-9(d). Contours of unsteady total pressure $p_{0,rms} / p_{0,edge}$ at $X/L_s = 0.86$ and $Re = 9.8 \times 10^6$ m^{-1}.

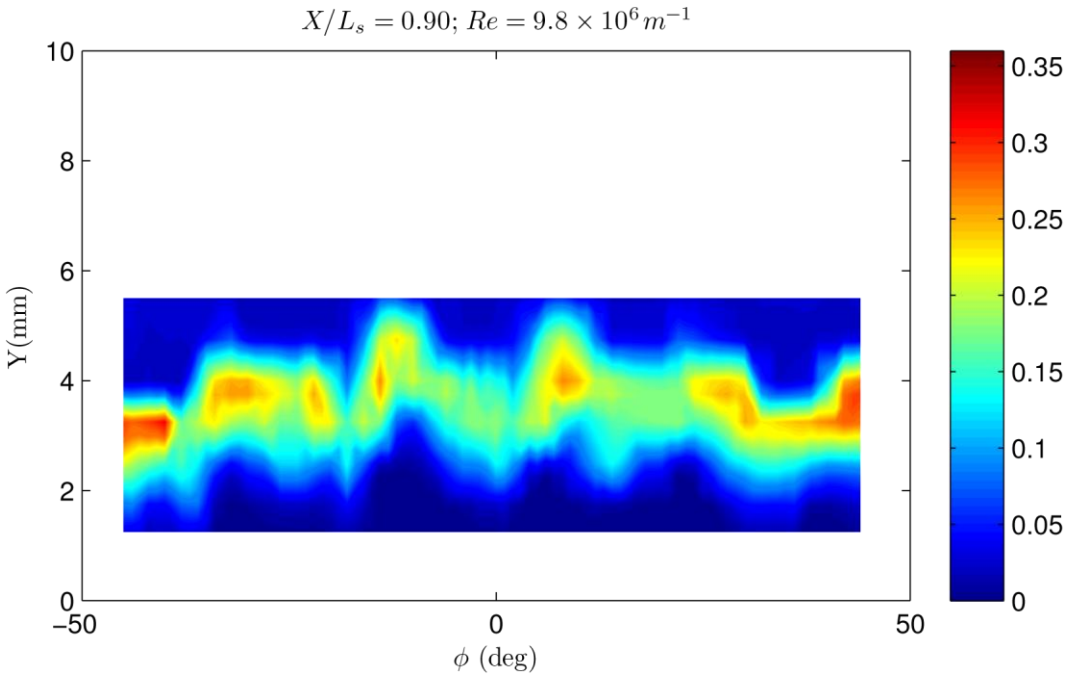

Figure A-47. Enlarged version of Figure 4-9(e). Contours of unsteady total pressure $p_{0,rms} / p_{0,edge}$ at $X/L_s = 0.90$ and $Re = 9.8 \times 10^6$ m^{-1}.

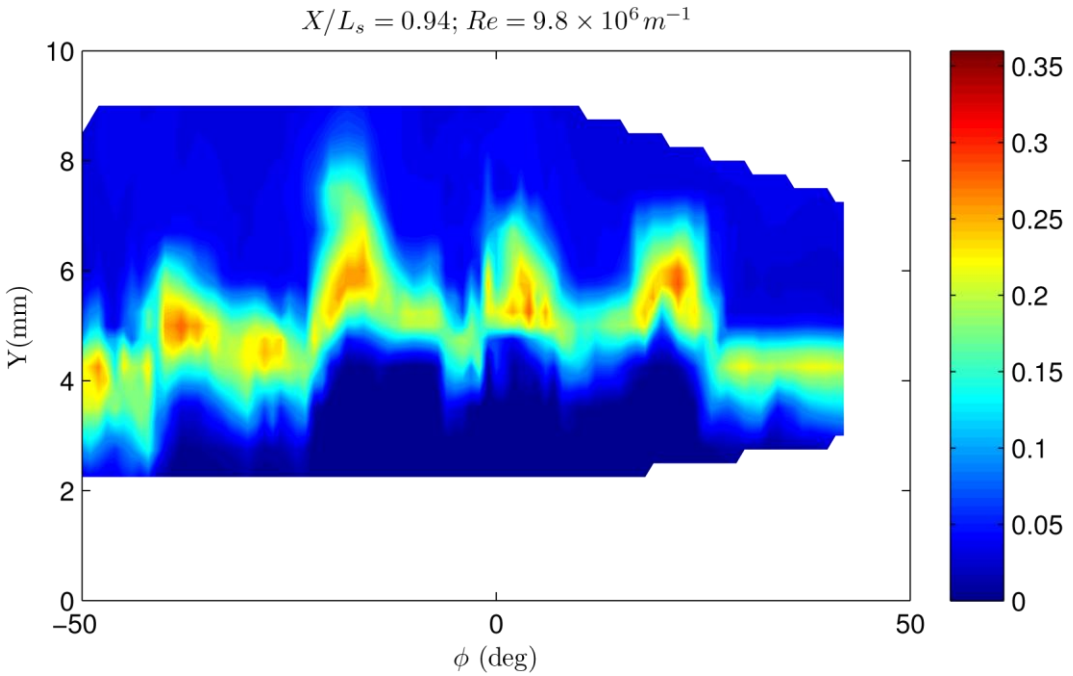

Figure A-48. Enlarged version of Figure 4-9(f). Contours of unsteady total pressure $p_{0,rms} / p_{0,edge}$ at $X/L_s = 0.94$ and $Re = 9.8 \times 10^6$ m^{-1}.

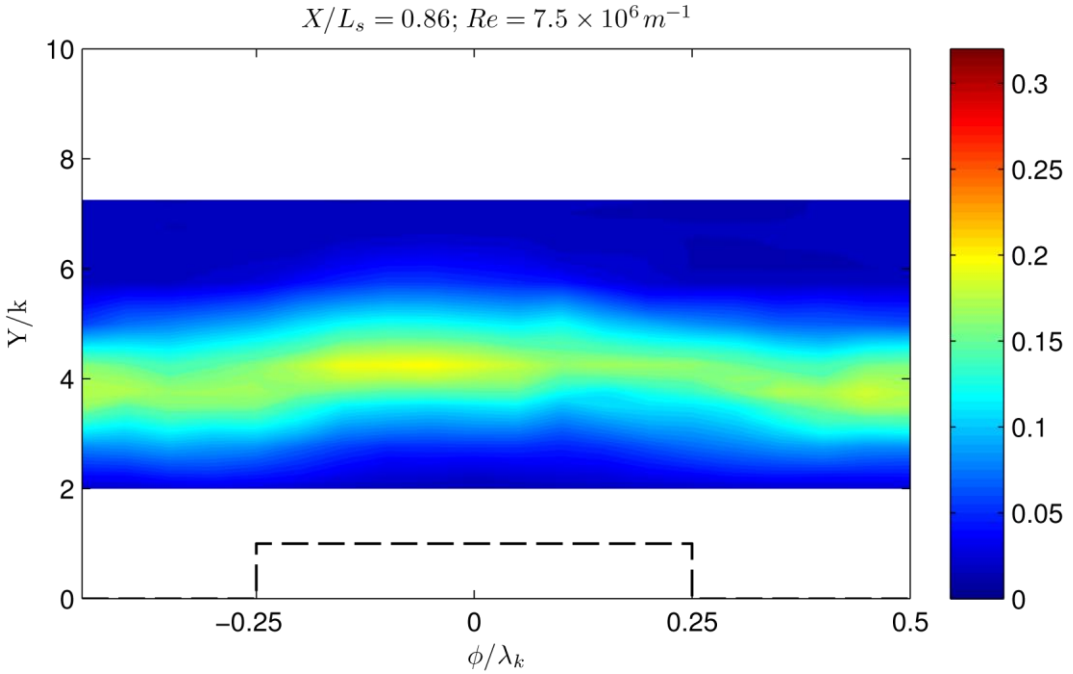

Figure A-49. Enlarged version of Figure 4-10(a). Phase-locked averaged contours of unsteady total pressure $p_{0,rms} / p_{0,edge}$ at $X/L_s = 0.86$ and $Re = 7.5 \times 10^6$ m^{-1}. Dashed lines indicate the projection of a roughness element into the measurement plane.

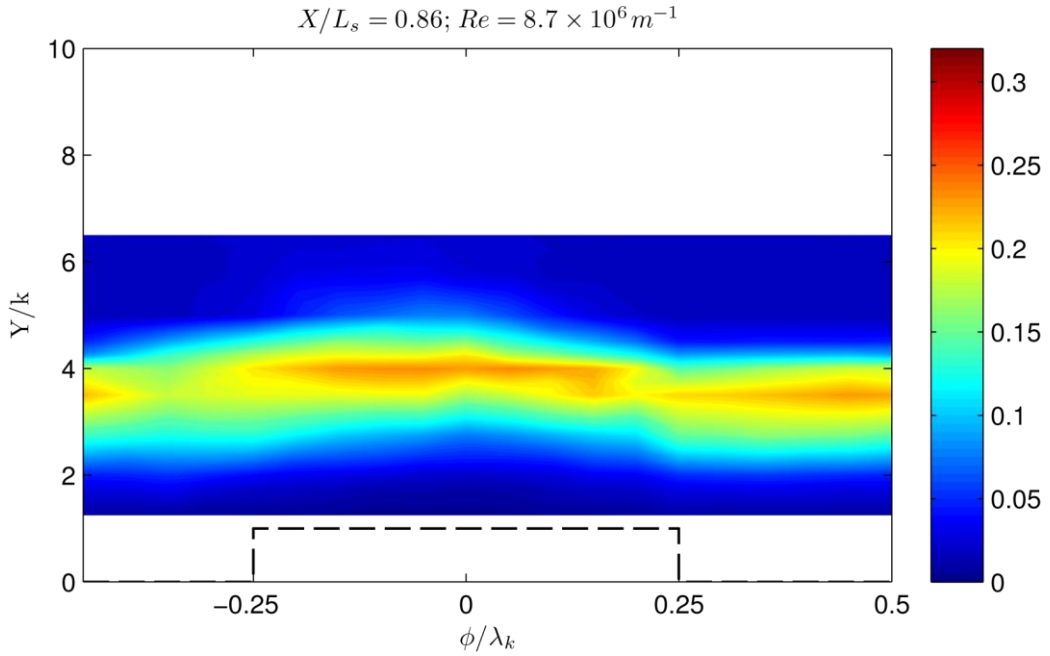

Figure A-50. Enlarged version of Figure 4-10(b). Phase-locked averaged contours of unsteady total pressure $p_{0,rms} / p_{0,edge}$ at $X/L_s = 0.86$ and $Re = 8.7 \times 10^6$ m^{-1}. Dashed lines indicate the projection of a roughness element into the measurement plane.

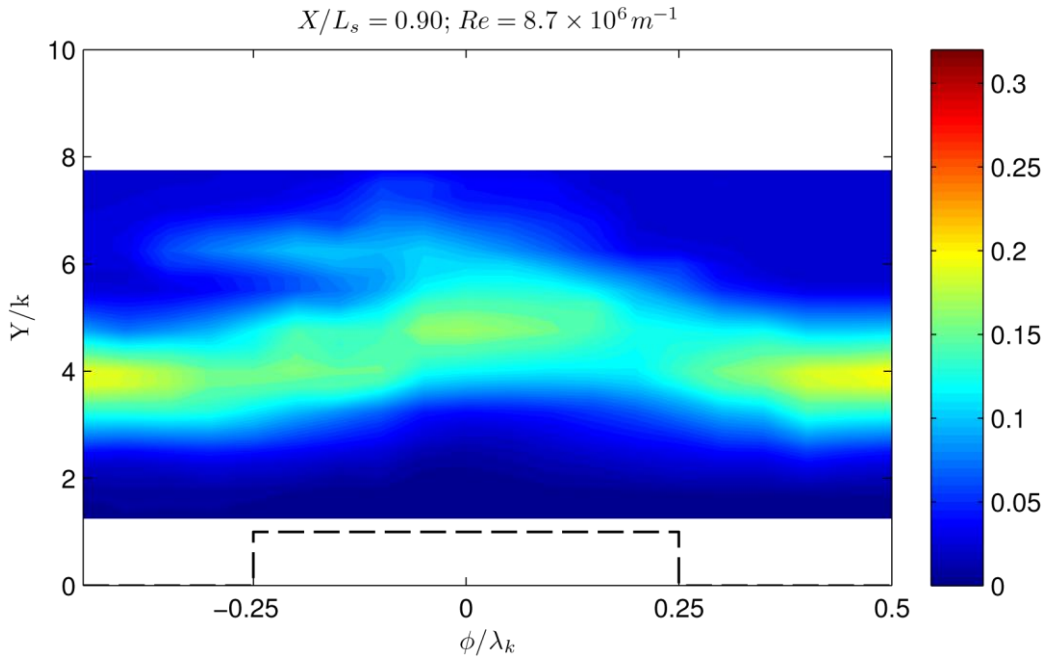

Figure A-51. Enlarged version of Figure 4-10(c). Phase-locked averaged contours of unsteady total pressure $p_{0,rms} / p_{0,edge}$ at $X/L_s = 0.90$ and $Re = 8.7 \times 10^6$ m^{-1}. Dashed lines indicate the projection of a roughness element into the measurement plane.

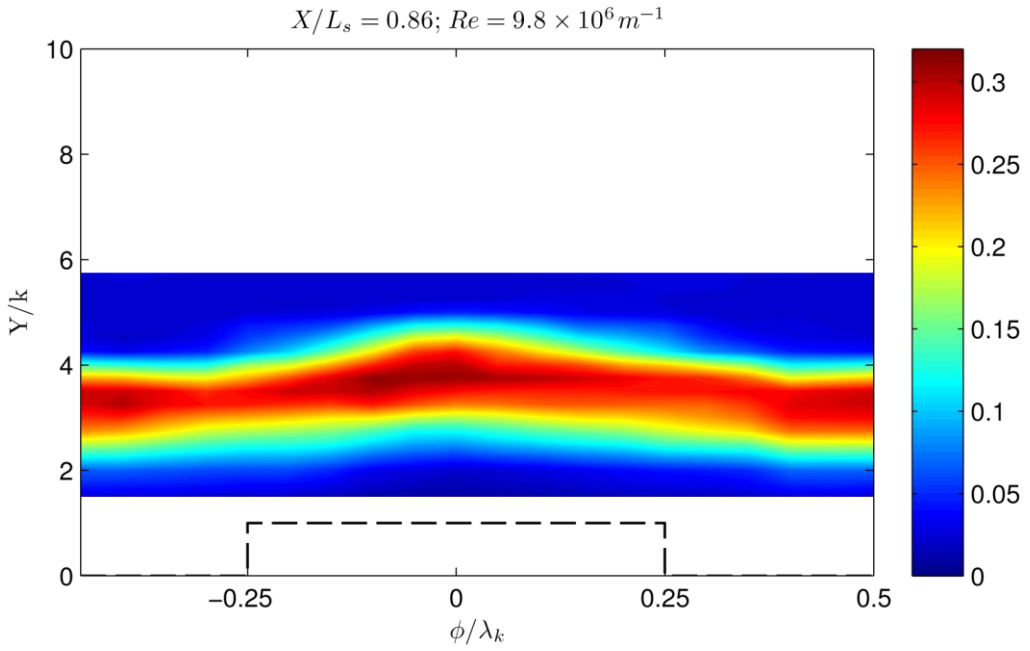

Figure A-52. Enlarged version of Figure 4-10(d). Phase-locked averaged contours of unsteady total pressure $p_{0,rms} / p_{0,edge}$ at $X/L_s = 0.86$ and $Re = 9.8 \times 10^6$ m^{-1}. Dashed lines indicate the projection of a roughness element into the measurement plane.

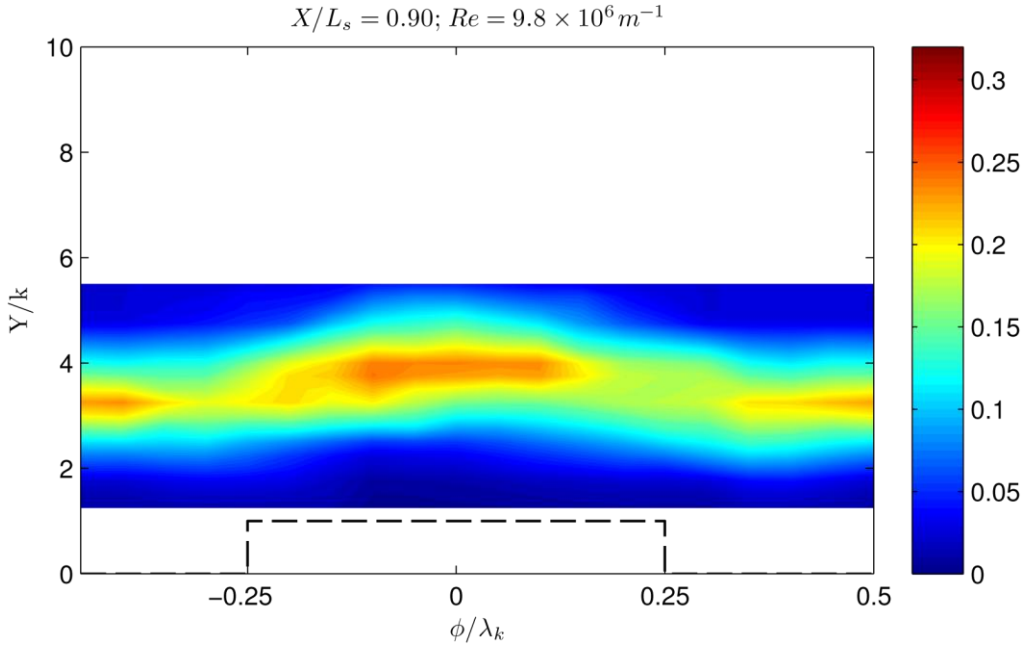

Figure A-53. Enlarged version of Figure 4-10(e). Phase-locked averaged contours of unsteady total pressure $p_{0,rms} / p_{0,edge}$ at $X/L_s = 0.90$ and $Re = 9.8 \times 10^6$ m^{-1}. Dashed lines indicate the projection of a roughness element into the measurement plane.

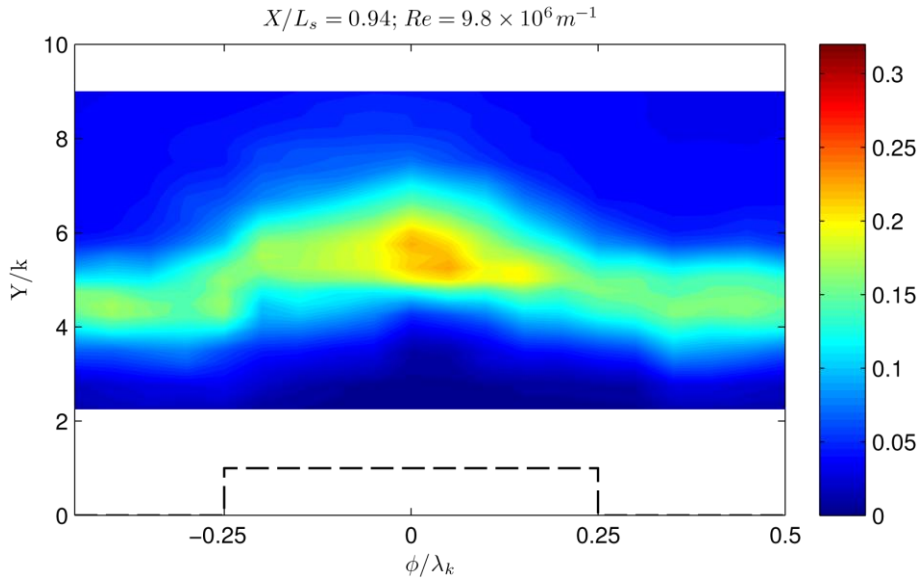

Figure A-54. Enlarged version of Figure 4-10(f). Phase-locked averaged contours of unsteady total pressure $p_{0,rms} / p_{0,edge}$ at $X/L_s = 0.94$ and $Re = 9.8 \times 10^6$ m^{-1}. Dashed lines indicate the projection of a roughness element into the measurement plane.

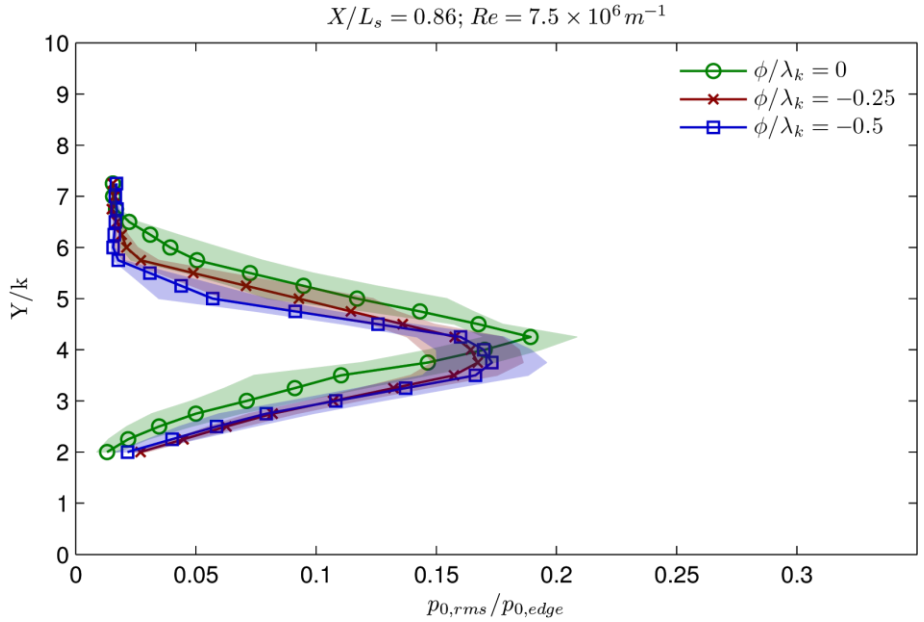

Figure A-55. Enlarged version of Figure 4-11(a). Wall-normal unsteady total pressure $p_{0,rms} / p_{0,edge}$ profiles at $X/L_s = 0.86$ and $Re = 7.5 \times 10^6$ m^{-1}. Phase-locked averaged profiles are shown along the roughness element centerline $(\phi / \lambda_k = 0)$, at the roughness element edge $(\phi / \lambda_k = -0.25)$, and between the roughness elements $(\phi / \lambda_k = -0.5)$. The shaded regions indicate the standard error of the phase-locked mean.

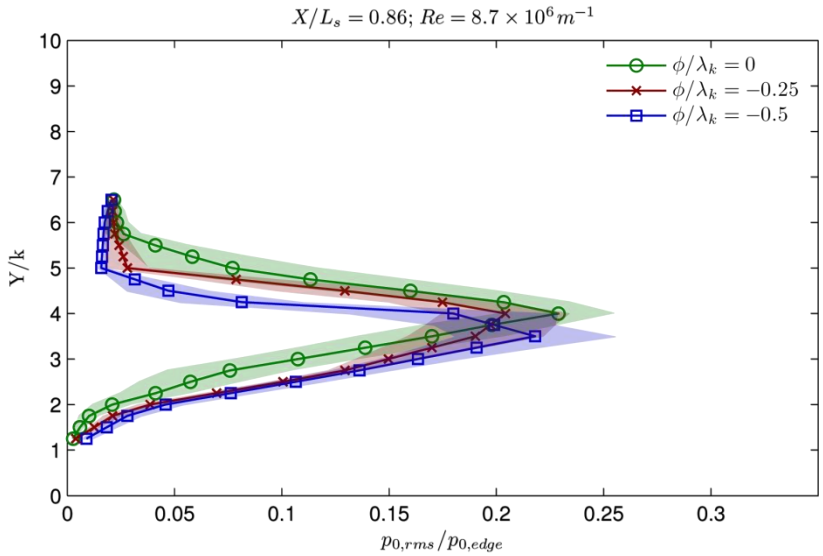

Figure A-56. Enlarged version of Figure 4-11(b). Wall-normal unsteady total pressure $p_{0,rms} / p_{0,edge}$ profiles at $X/L_s = 0.86$ and $Re = 8.7 \times 10^6$ m^{-1}. Phase-locked averaged profiles are shown along the roughness element centerline $(\phi / \lambda_k = 0)$, at the roughness element edge $(\phi / \lambda_k = -0.25)$, and between the roughness elements $(\phi / \lambda_k = -0.5)$. The shaded regions indicate the standard error of the phase-locked mean.

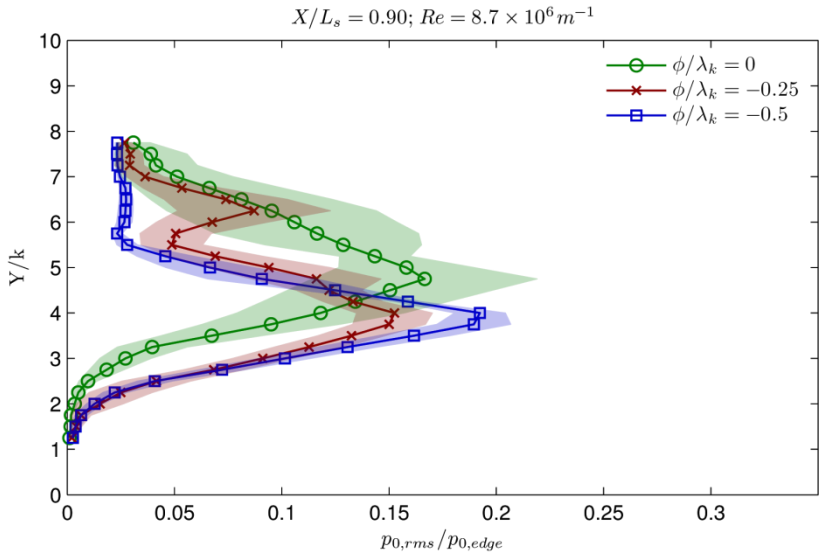

Figure A-57. Enlarged version of Figure 4-11(c). Wall-normal unsteady total pressure $p_{0,rms} / p_{0,edge}$ profiles at $X/L_s = 0.90$ and $Re = 8.7 \times 10^6$ m^{-1}. Phase-locked averaged profiles are shown along the roughness element centerline $(\phi / \lambda_k = 0)$, at the roughness element edge $(\phi / \lambda_k = -0.25)$, and between the roughness elements $(\phi / \lambda_k = -0.5)$. The shaded regions indicate the standard error of the phase-locked mean.

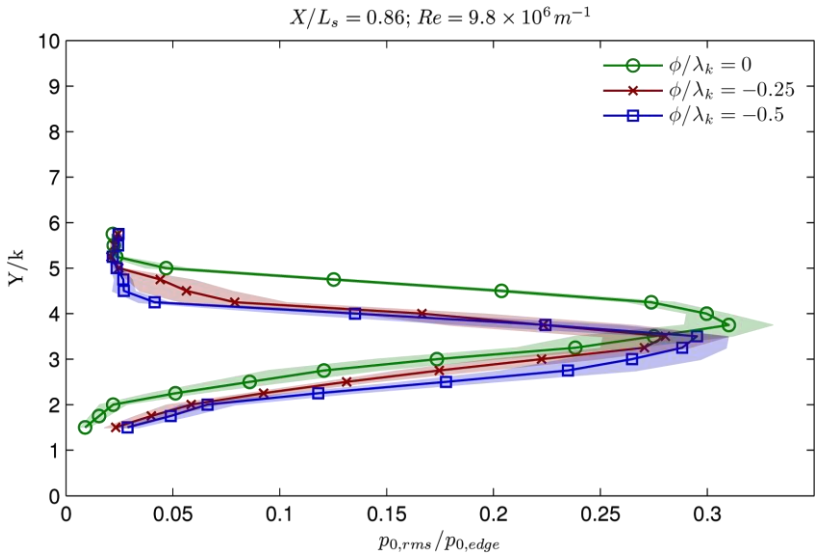

Figure A-58. Enlarged version of Figure 4-11(d). Wall-normal unsteady total pressure $p_{0,rms} / p_{0,edge}$ profiles at X/L_s = 0.86 and Re = 9.8 × 10^6 m^{-1}. Phase-locked averaged profiles are shown along the roughness element centerline $(\phi / \lambda_k = 0)$, at the roughness element edge $(\phi / \lambda_k = -0.25)$, and between the roughness elements $(\phi / \lambda_k = -0.5)$. The shaded regions indicate the standard error of the phase-locked mean.

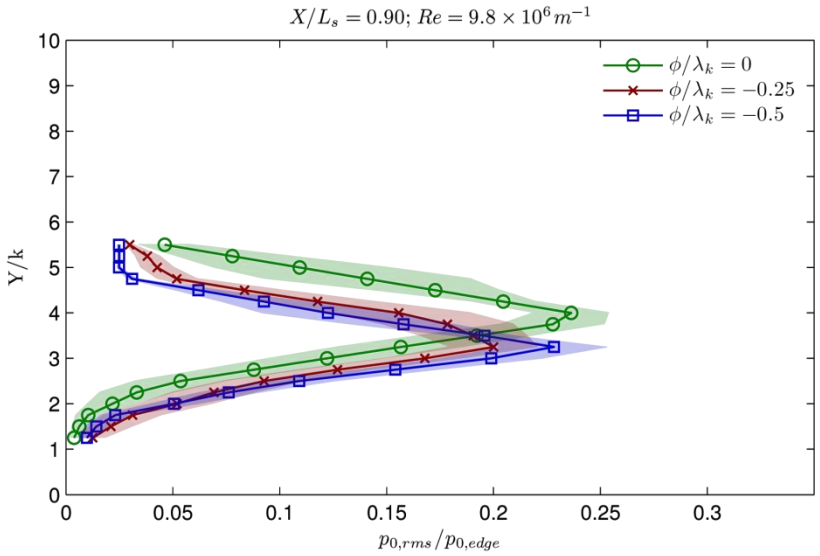

Figure A-59. Enlarged version of Figure 4-11(e). Wall-normal unsteady total pressure $p_{0,rms} / p_{0,edge}$ profiles at X/L_s = 0.90 and Re = 9.8 × 10^6 m^{-1}. Phase-locked averaged profiles are shown along the roughness element centerline $(\phi / \lambda_k = 0)$, at the roughness element edge $(\phi / \lambda_k = -0.25)$, and between the roughness elements $(\phi / \lambda_k = -0.5)$. The shaded regions indicate the standard error of the phase-locked mean.

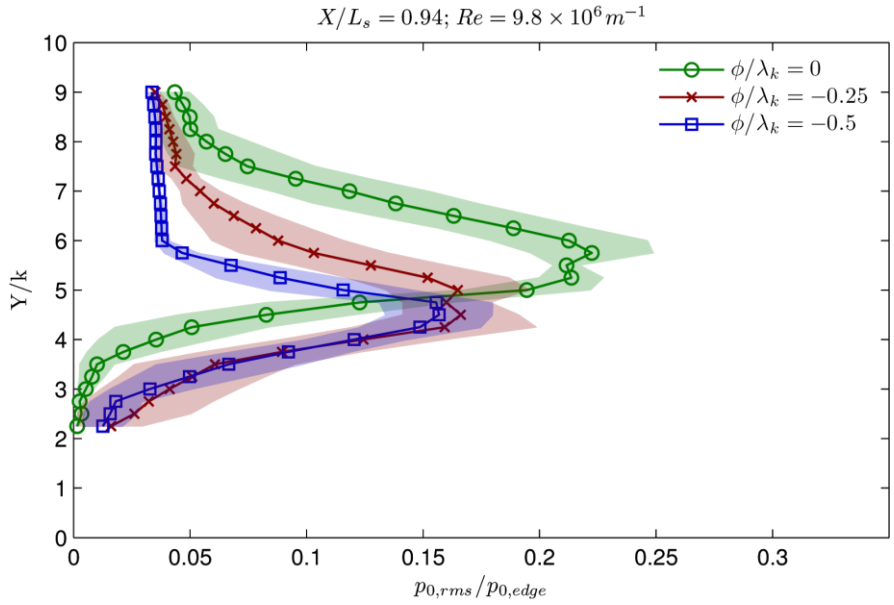

Figure A-60. Enlarged version of Figure 4-11(f). Wall-normal unsteady total pressure $p_{0,rms} / p_{0,edge}$ profiles at $X/L_s = 0.94$ and $Re = 9.8 \times 10^6$ m^{-1}. Phase-locked averaged profiles are shown along the roughness element centerline $(\phi / \lambda_k = 0)$, at the roughness element edge $(\phi / \lambda_k = -0.25)$, and between the roughness elements $(\phi / \lambda_k = -0.5)$. The shaded regions indicate the standard error of the phase-locked mean.

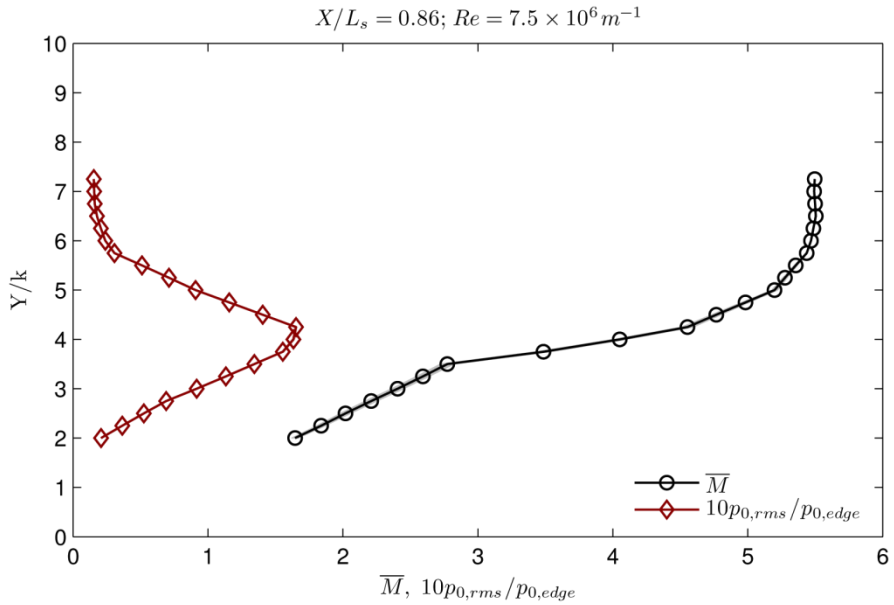

Figure A-61. Enlarged version of Figure 4-12(a). Wall-normal profiles of $\overline{M}$ and $p_{0,rms} / p_{0,edge}$ at $X/L_s = 0.86$ and $Re = 7.5 \times 10^6$ m^{-1}. The shaded region indicates the extent of the uncertainty.

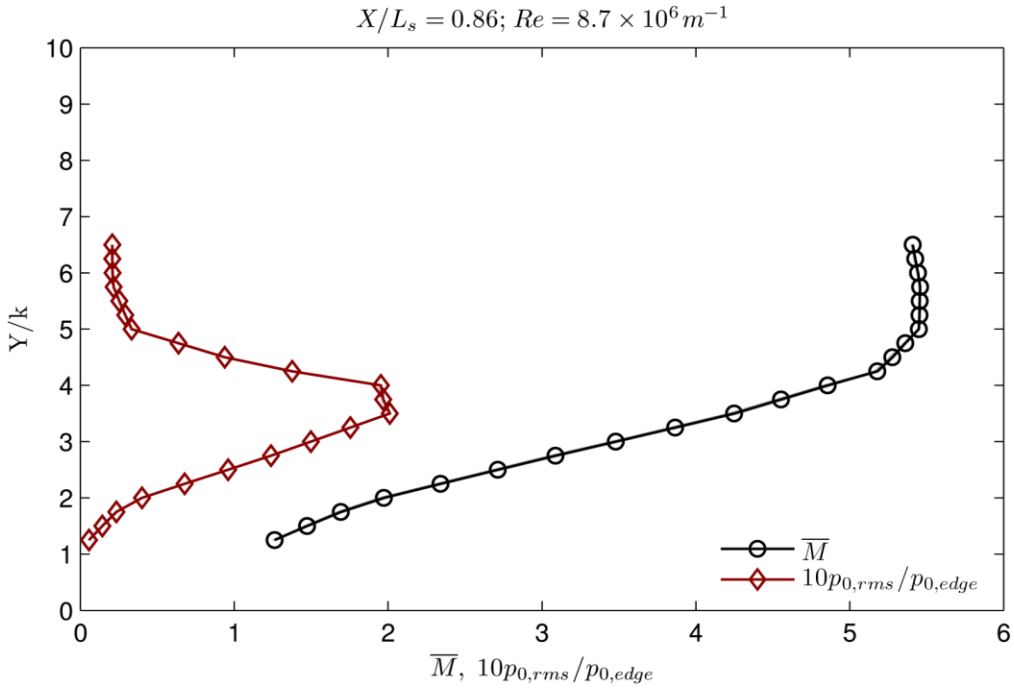

Figure A-62. Enlarged version of Figure 4-12(b). Wall-normal profiles of $\overline{M}$ and $p_{0,rms} / p_{0,edge}$ at $X/L_s = 0.86$ and $Re = 8.7 \times 10^6$ m^{-1}. The shaded region indicates the extent of the uncertainty.

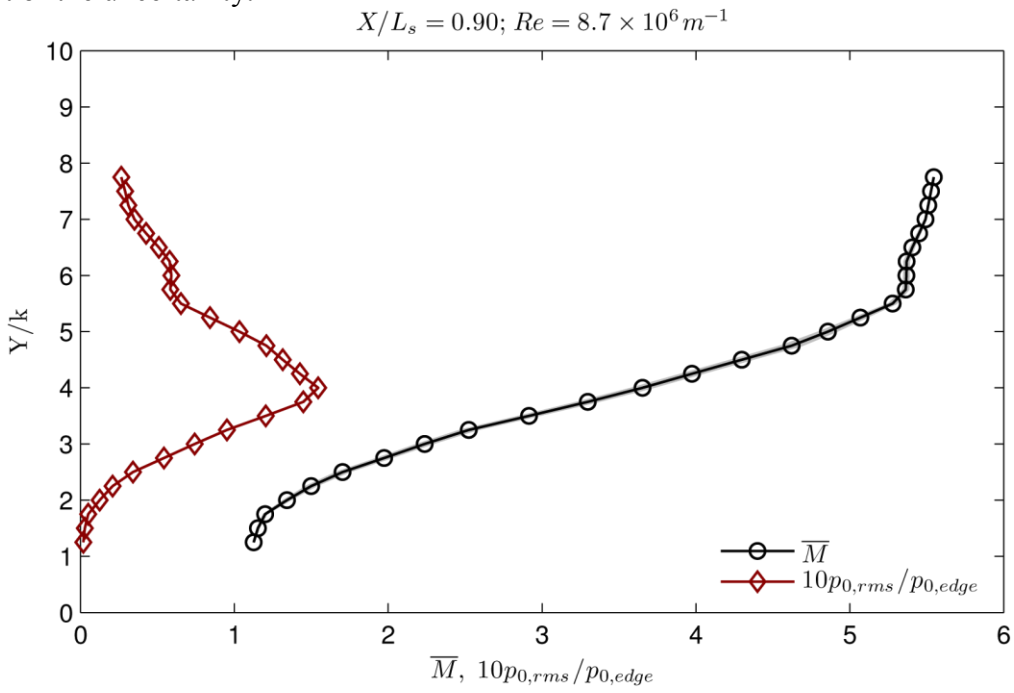

Figure A-63. Enlarged version of Figure 4-12(c). Wall-normal profiles of $\overline{M}$ and $p_{0,rms} / p_{0,edge}$ at $X/L_s = 0.90$ and $Re = 8.7 \times 10^6$ m^{-1}. The shaded region indicates the extent of the uncertainty.

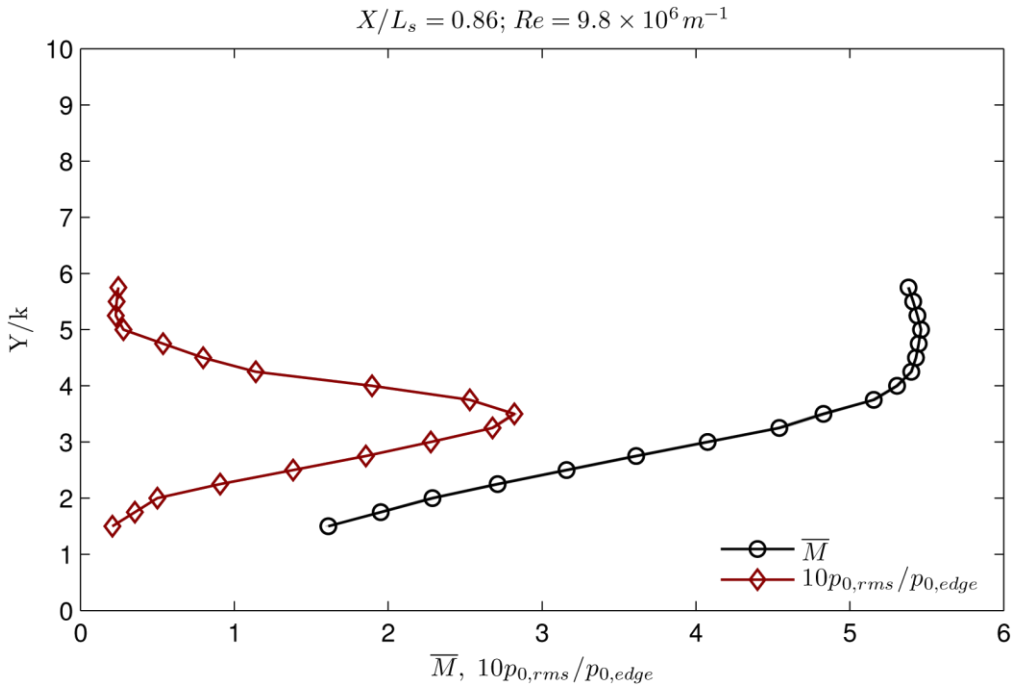

Figure A-64. Enlarged version of Figure 4-12(d). Wall-normal profiles of $\overline{M}$ and $p_{0,rms} / p_{0,edge}$ at $X/L_s = 0.86$ and $Re = 9.8 \times 10^6$ m^{-1}. The shaded region indicates the extent of the uncertainty.

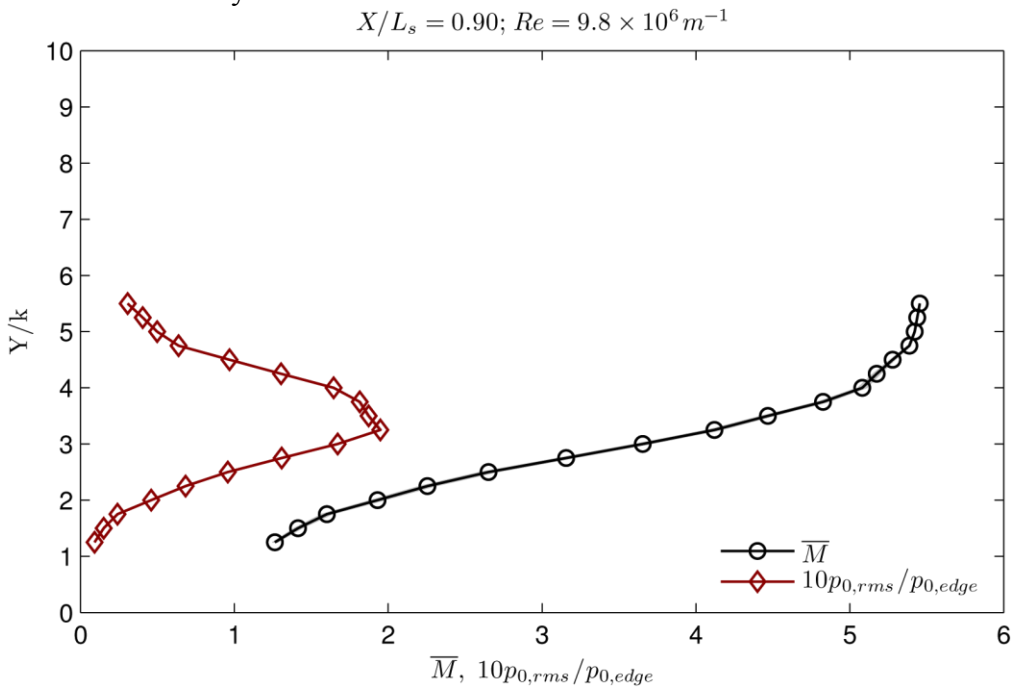

Figure A-65. Enlarged version of Figure 4-12(e). Wall-normal profiles of $\overline{M}$ and $p_{0,rms} / p_{0,edge}$ at $X/L_s = 0.90$ and $Re = 9.8 \times 10^6$ m^{-1}. The shaded region indicates the extent of the uncertainty.

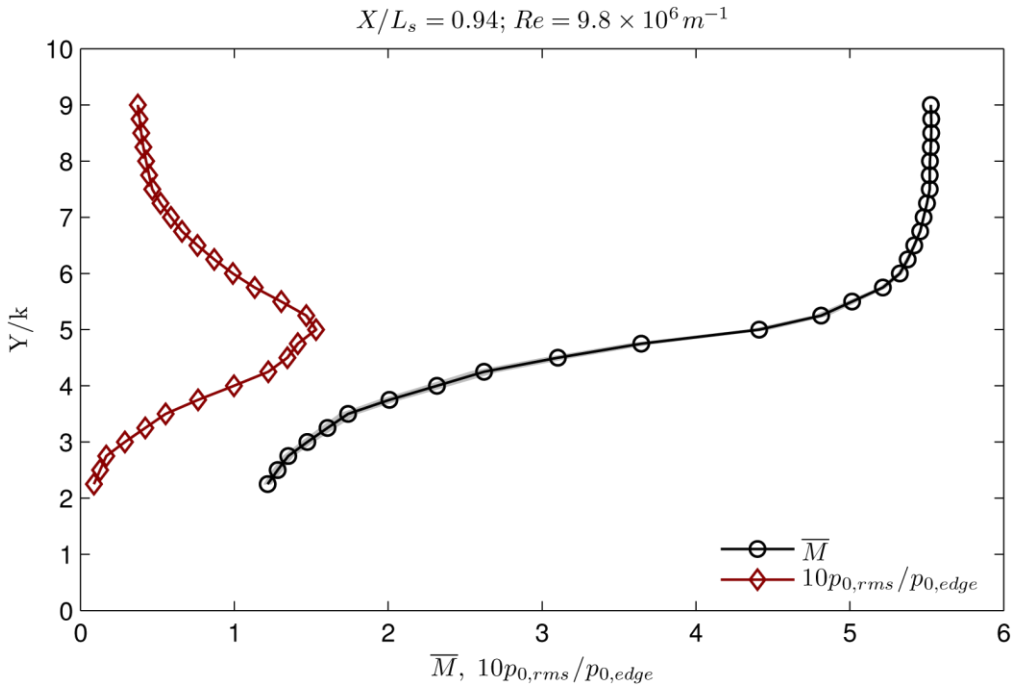

Figure A-66. Enlarged version of Figure 4-12(f). Wall-normal profiles of $\overline{M}$ and $p_{0,rms} / p_{0,edge}$ at $X/L_s = 0.94$ and $Re = 9.8 \times 10^6$ m^{-1}. The shaded region indicates the extent of the uncertainty.

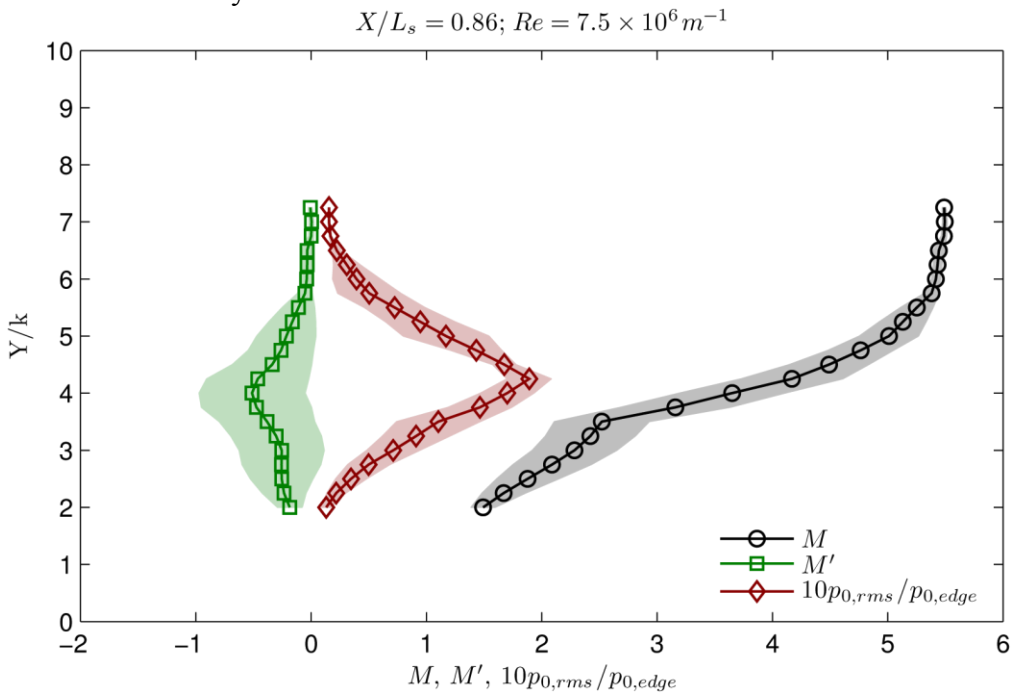

Figure A-67. Enlarged version of Figure 4-13(a). Wall-normal profiles of M , M', and $p_{0,rms} / p_{0,edge}$ along the centerline of a roughness element at $X/L_s = 0.86$ and $Re = 7.5 \times 10^6$ m^{-1}. The shaded regions indicate the standard error of the phase-locked mean.

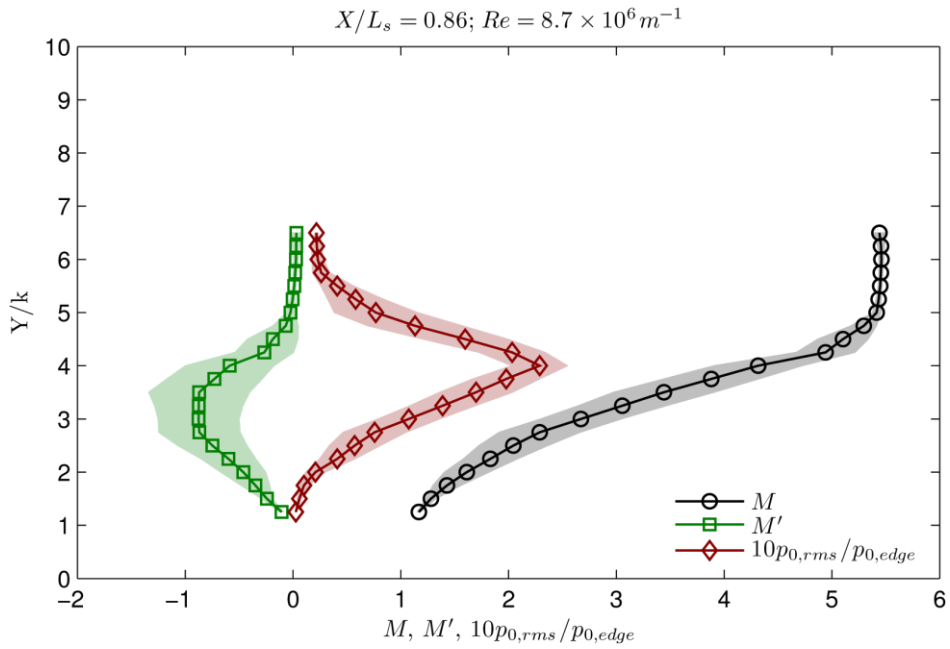

Figure A-68. Enlarged version of Figure 4-13(b). Wall-normal profiles of M , M', and $p_{0,rms}$ / $p_{0,edge}$ along the centerline of a roughness element at $X/L_s = 0.86$ and $Re = 8.7 \times 10^6$ m^{-1}. The shaded regions indicate the standard error of the phase-locked mean.

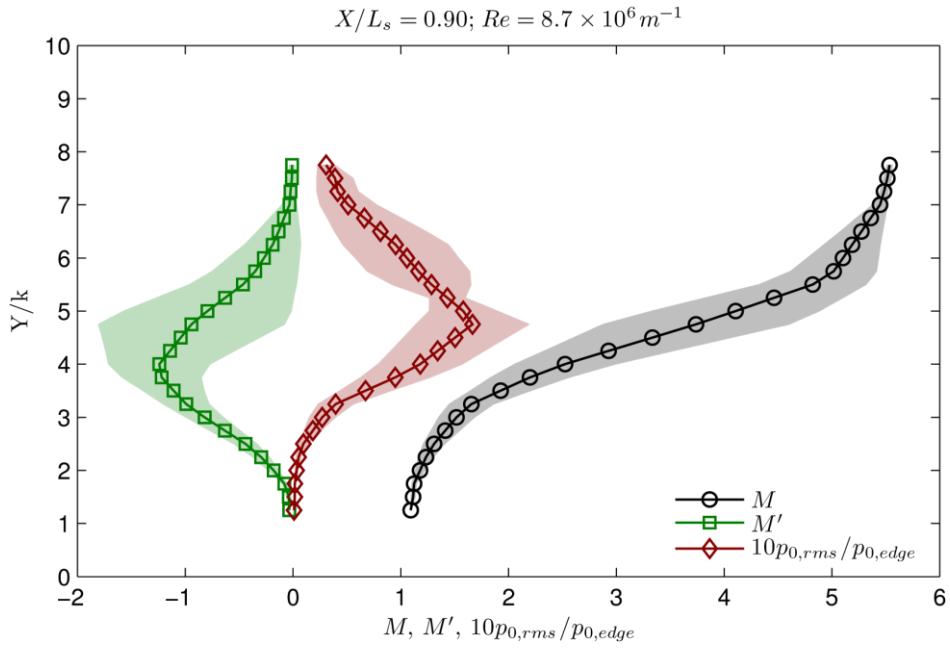

Figure A-69. Enlarged version of Figure 4-13(c). Wall-normal profiles of M , M', and $p_{0,rms}$ / $p_{0,edge}$ along the centerline of a roughness element at $X/L_s = 0.90$ and $Re = 8.7 \times 10^6$ m^{-1}. The shaded regions indicate the standard error of the phase-locked mean.

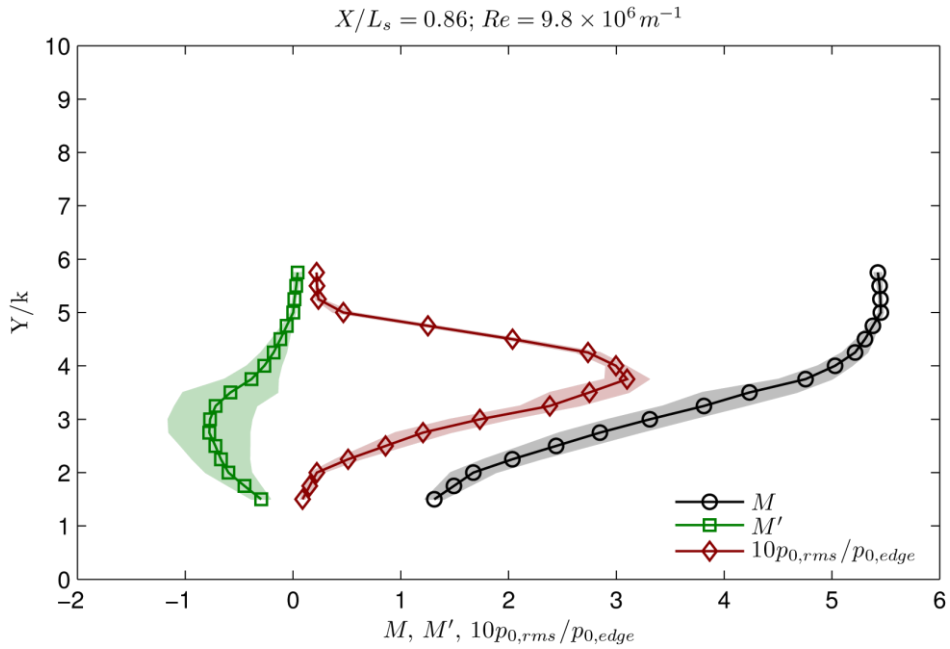

Figure A-70. Enlarged version of Figure 4-13(d). Wall-normal profiles of M , M', and $p_{0,rms} / p_{0,edge}$ along the centerline of a roughness element at $X/L_s = 0.86$ and $Re = 9.8 \times 10^6$ m^{-1}. The shaded regions indicate the standard error of the phase-locked mean.

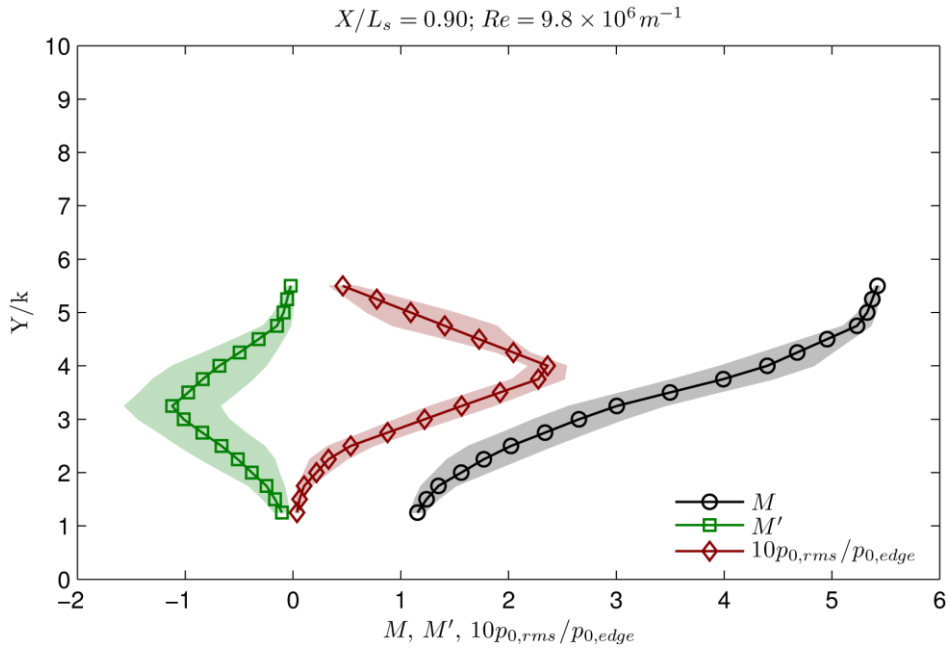

Figure A-71. Enlarged version of Figure 4-13(e). Wall-normal profiles of M , M', and $p_{0,rms} / p_{0,edge}$ along the centerline of a roughness element at $X/L_s = 0.90$ and $Re = 9.8 \times 10^6$ m^{-1}. The shaded regions indicate the standard error of the phase-locked mean.

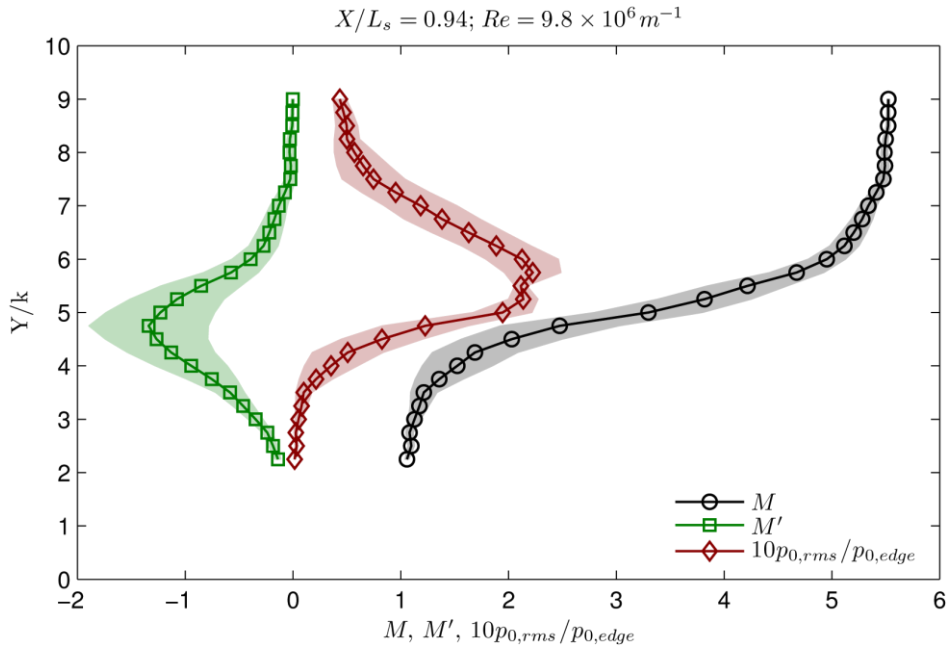

Figure A-72. Enlarged version of Figure 4-13(f). Wall-normal profiles of M , M', and $p_{0,rms} / p_{0,edge}$ along the centerline of a roughness element at $X/L_s = 0.94$ and $Re = 9.8 \times 10^6$ m^{-1}. The shaded regions indicate the standard error of the phase-locked mean.

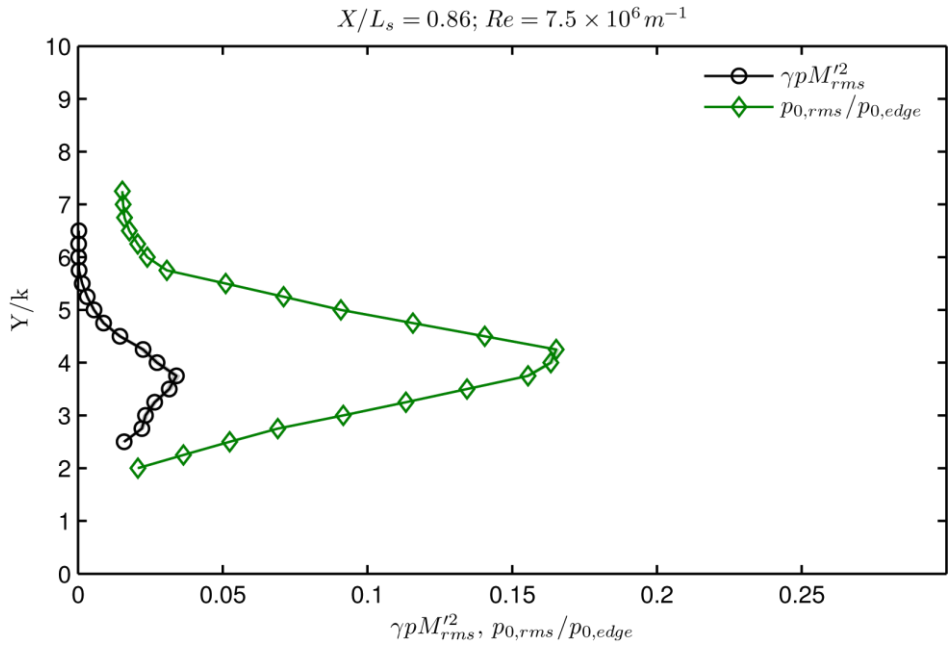

Figure A-73. Enlarged version of Figure 4-14(a). Steady disturbance and unsteady total Pitot pressure profiles $\gamma p M'^2_{rms}$ and $p_{0,rms} / p_{0,edge}$ at $X/L_s = 0.86$ and $Re = 7.5 \times 10^6$ m^{-1}. The shaded regions indicate the extent of the uncertainty.

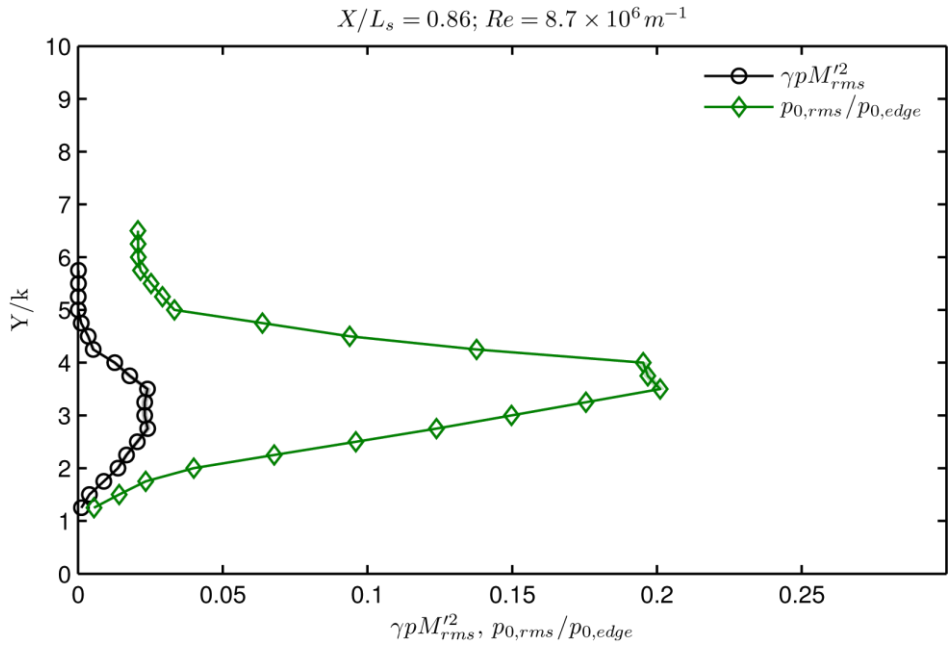

Figure A-74. Enlarged version of Figure 4-14(b). Steady disturbance and unsteady total Pitot pressure profiles $\gamma p M'^2_{rms}$ and $p_{0,rms} / p_{0,edge}$ at $X/L_s = 0.86$ and $Re = 8.7 \times 10^6$ m^{-1}. The shaded regions indicate the extent of the uncertainty.

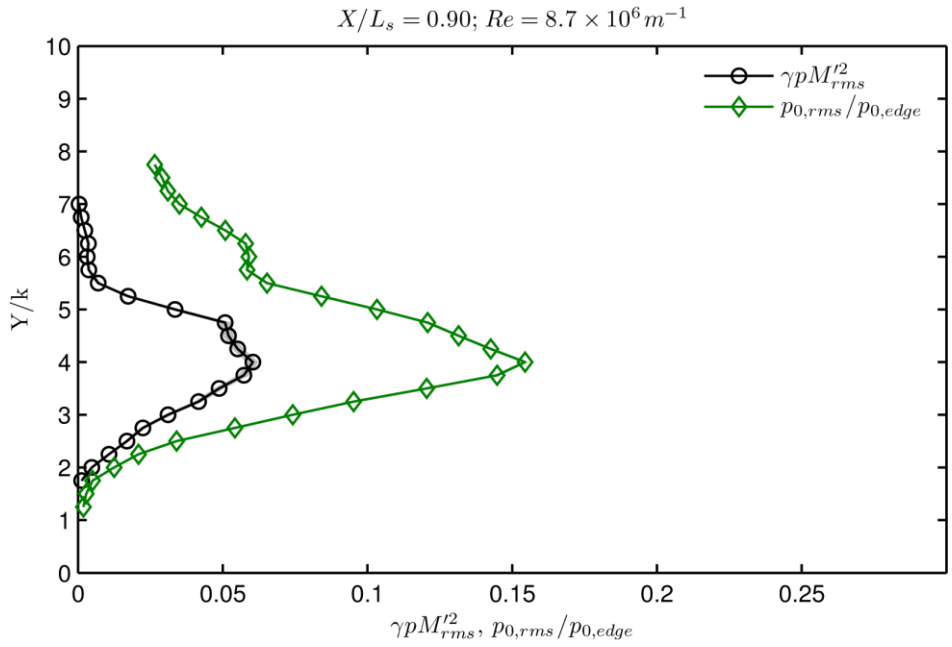

Figure A-75. Enlarged version of Figure 4-14(c). Steady disturbance and unsteady total Pitot pressure profiles $\gamma p M'^2_{rms}$ and $p_{0,rms} / p_{0,edge}$ at $X/L_s = 0.90$ and $Re = 8.7 \times 10^6$ m^{-1}. The shaded regions indicate the extent of the uncertainty.

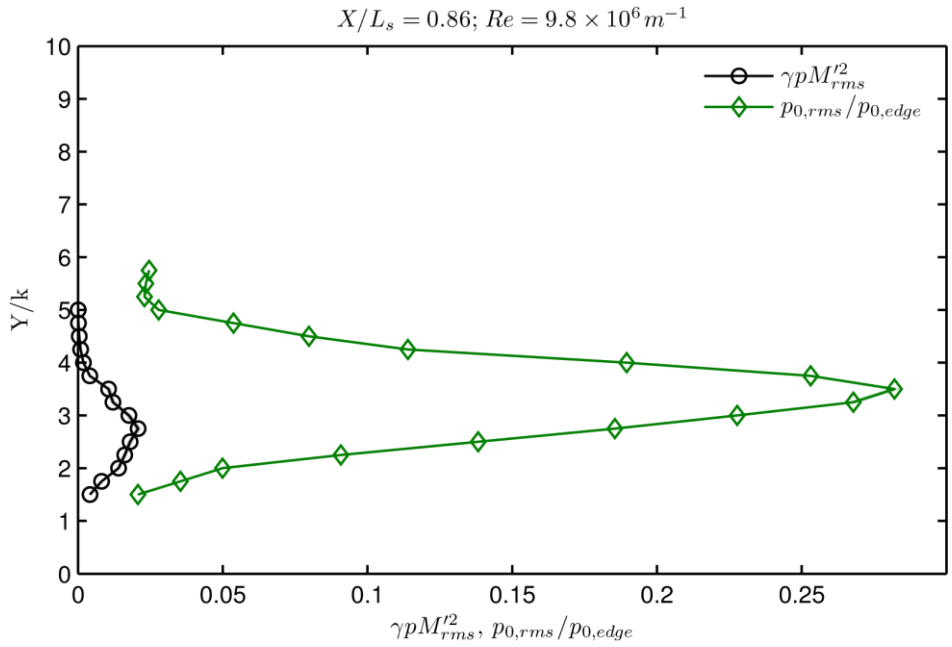

Figure A-76. Enlarged version of Figure 4-14(d). Steady disturbance and unsteady total Pitot pressure profiles $\gamma p M'^2_{rms}$ and $p_{0,rms} / p_{0,edge}$ at $X/L_s = 0.86$ and $Re = 9.8 \times 10^6$ m^{-1}. The shaded regions indicate the extent of the uncertainty.

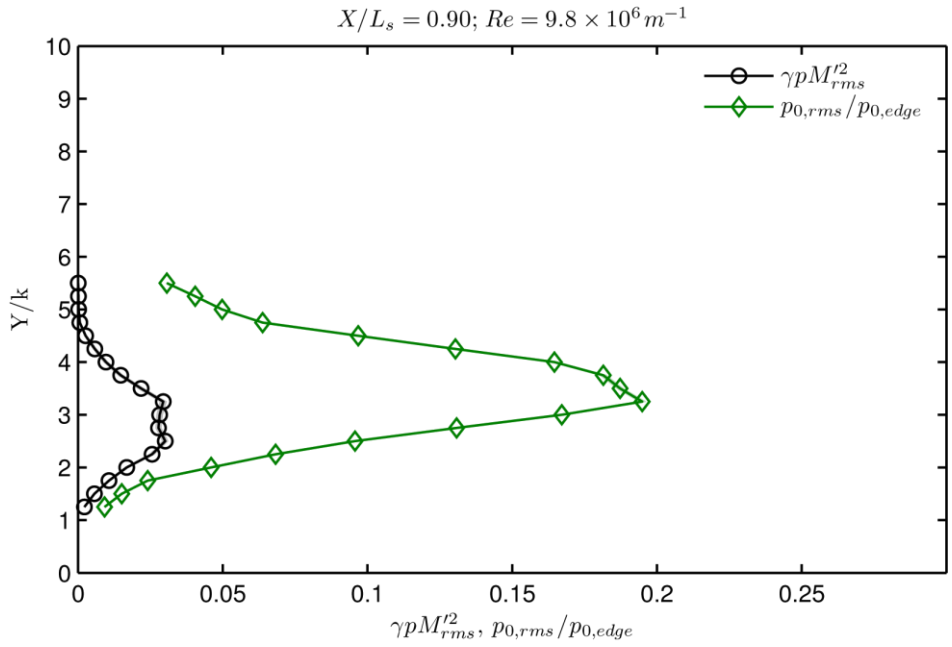

Figure A-77. Enlarged version of Figure 4-14(e). Steady disturbance and unsteady total Pitot pressure profiles $\gamma p M'^2_{rms}$ and $p_{0,rms} / p_{0,edge}$ at $X/L_s = 0.90$ and $Re = 9.8 \times 10^6$ m^{-1}. The shaded regions indicate the extent of the uncertainty.

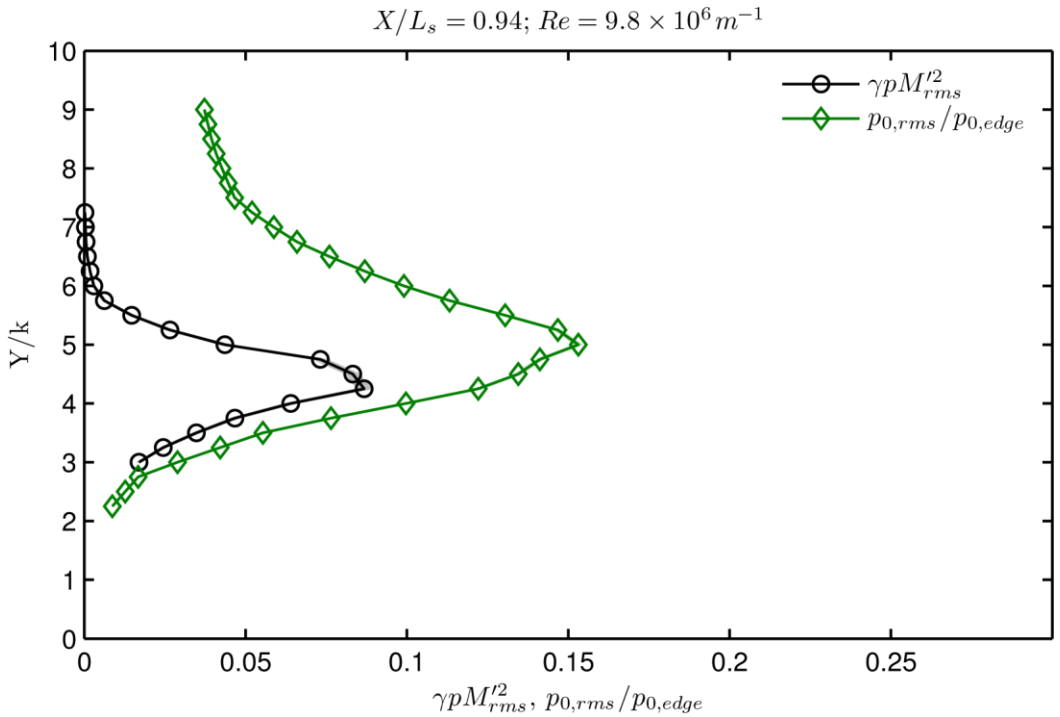

Figure A-78. Enlarged version of Figure 4-14(f). Steady disturbance and unsteady total Pitot pressure profiles $\gamma p M'^2_{rms}$ and $p_{0,rms} / p_{0,edge}$ at $X/L_s = 0.94$ and $Re = 9.8 \times 10^6$ m^{-1}. The shaded regions indicate the extent of the uncertainty.